Consortium

for

Small-Scale Modelling

Deutscher Wetterdienst
MeteoSwiss
Ufficio Generale Spazio Aereo e Meteorologia
ΕΘΝΙΚΗ ΜΕΤΕΩΡΟΛΟΓΙΚΗ ΥΠΗΡΕΣΙΑ
Instytucie Meteorogii i Gospodarki Wodnej
Administratia Nationala de Meteorologie
ROSHYDROMET
Agenzia Regionale per la Protezione Ambientale del Piemonte
Agenzia Regionale per la Protezione Ambientale dell'Emilia-Romagna
Centro Italiano Ricerche Aerospaziali
Amt für GeoInformationswesen der Bundeswehr

www.cosmo-model.org

The COSMO Priority Project
'Conservative Dynamical Core'
Final Report

M. Baldauf [*]**, O. Fuhrer, M. J. Kurowski, G. de Morsier,**

M. Müllner, Z. P. Piotrowski, B. Rosa, P. L. Vitagliano,

D. Wójcik, M. Ziemiański

[*] corresponding author:
Dr. Michael Baldauf
Deutscher Wetterdienst
Frankfurter Str. 135
63067 Offenbach am Main
Germany

Contents

1   Introduction

In 2008, the COSMO steering committee (STC) established a new Priority Project named 'Conservative Dynamical Core' (CDC). The motivation for such a project stems from the fact that the three currently available dynamical cores of COSMO (called 'leapfrog', 'Runge-Kutta' and 'semi-implicit') don't have any conservation properties concerning the dynamical variables mass, energy or momentum. However, conservation of these variables is one of the fundamental guiding principles in the development of dynamical cores in many branches of fluid dynamics. The aim of the project was to investigate possible candidates for a new dynamical core with conservation properties (at least mass conservation) and to deliver prototypes that are already implemented into the COSMO model.

Considering the different proposed dynamical core formulations of the first draft project plan, the STC decided to concentrate the project on two branches: on the one hand to the EULAG model ('anelastic branch'), which is already well established in the fluid dynamics community, and on the other hand to the CONSOL solver ('compressible branch'), which stems from the aerodynamics community. EULAG is based on an anelastic approximation of the Euler equations. It uses a finite volume approach, which per se guarantees certain conservation properties. CONSOL is based on the compressible Euler equations and also uses a finite volume approach. Both solvers use implicit time integration methods: CONSOL for the whole dynamical core, EULAG at least for the fast, quasi-linear processes. This solution strategy in general helps in solving another issue which should be tackled by the project, namely to improve the ability of the dynamical core to be stable in steep terrain. This requirement is caused by the future applications of COSMO which will cover more and more horizontal resolutions of 1 km and less, where one can expect increasingly steeper slopes.

During the project, the properties of the two proposed solvers should be inspected. For this purpose, a 'decision tree' was defined at the beginning starting from a set of well accepted idealized tests until more complex semi-realistic tests which should be simulated by the prototypes.

Therefore, the first 2 papers (sections 2 and 3) deal with idealized tests consisting of stationary flow over mountains, expansion of linear gravity waves, strongly nonlinear and unstationary falling bubbles, and convection containing cloud microphysics, simulated with the EULAG model. The ability of the EULAG dynamical core to simulate meteorologically relevant flow fields is demonstrated in section 4. Finally the functionality of the COSMO-prototype with the implemented EULAG dynamical core is demonstrated with semi-realistic model setups in section 5.

Whereas the EULAG model has been used for some meteorological simulations before, this was not the case for CONSOL, for which a great challenge was the introduction of the buoyancy term into the existing pure hydrodynamical solver. Therefore, only a reduced test set could be inspected with this solver. Section 8 describes the solver and the idealized tests performed with it.

Apart from the pure dynamical core (the solver of the EULER equations), tracer advection is an important aspect of the numerics of a model, too. Section 6 investigates the basic advection scheme of EULAG, the MPDATA, for its usability as an alternative tracer transport scheme in COSMO.

The accompanying section 7 compares wave expansion properties of the several anelastic approximations with the compressible equations and the basic divergence damping mechanism used in the current COSMO dynamical core.

After a lifetime of about four years (end of 2012), the overall status of the project is an available prototype of COSMO-EULAG, ready for further testing in real case applications. Due to constraints in man power resources, the CONSOL solver couldn't achieve a similar stage. Therefore, the COSMO Science Management Committee and STC decided to finish the CDC project and to establish a folluw-up project, which concentrates on the 'COSMO-EULAG operationalization' (CELO).

M. Baldauf
Deutscher Wetterdienst

2 Dry benchmark experiments with the anelastic EULAG model

Bogdan Rosa, Marcin J. Kurowski, Michał Z. Ziemiański

Institute of Meteorology and Water Management - National Research Institute, Poland

2.1 Introduction

This chapter describes results from dry idealized benchmark experiments performed with the anelastic model EULAG. The goal of the study is to test the feasibility of an anelastic approach for very high-resolution (kilometer and sub-kilometer) operational numerical weather prediction. The choice of tests draws on experiences with analogous problems Skamarock et al. (2004) and is based on widely accepted benchmark solutions. The experiments were performed in the framework of the COSMO Priority Project Conservative Dynamical Core.

The first experiment concerns the evolution of a two-dimensional density current induced by a large bubble of cold air descending to the ground Straka et al. (1993). The second experiment considers two interacting bubbles with different temperatures Robert (1993). Both problems are strongly non-linear and do not have analytical solutions. The third test examines the propagation of inertia-gravity waves in a periodic channel (Skamarock and Klemp, 1994) of different length. The last problem regards the evolution of gravity waves generated by a flow over a single Agnesi mountain (Bonaventura, 2000). Several flow regimes (linear / nonlinear hydrostatic and linear / nonlinear non-hydrostatic), are examined. The results are validated against the reference solutions obtained using compressible models.

2.2 Cold density current test

The simulations of a cold density current are based on a setup described in Straka et al. (1993). This experiment is one of the well-known benchmarks often employed for testing numerical models.

2.2.1 Experiment setup

As defined in Straka et al. (1993), the two-dimensional density current is initiated as a cold bubble of air that subsequently descends to the ground in a homogenous and isentropic atmosphere. After reaching the ground, the bubble spreads laterally and rotors induced by a Kelvin-Helmholtz instability form on its upper boundary. The basic set of parameters and configuration of the model are as in Straka et al. (1993). This involves constant potential temperature of the basic hydrostatic state $\theta_0 = 300$ K and diffusion coefficient $K = 75$ m^{2}s^{-1}. The appropriate environmental density profile is given by the Ogura-Philips formula Ogura and Phillips (1962). The bubble is located at the center of the model domain which extends from $x = -25.6$ km to $x = 25.6$ km. The vertical domain size is $z = 6.4$ km. In the original experiment Straka et al. (1993) the lateral boundary conditions were set as $u = w_x = p_x = \theta_x = 0$ and similarly the vertical ones, namely $w = u_z = p_z = \theta_z = 0$ Here, the lateral boundary conditions are periodic. A free-slip and rigid boundary conditions are imposed at the ground and at the top of the computational domain, respectively. The numerical calculations in Straka et al. (1993) exploit the symmetry of the problem about the vertical line $x = 0$, which is not the case for the current simulations.

2.2.2   Results

The study, following Straka et al. (1993), is focused on the first 15 minutes of the evolution of the density current. Time evolution of potential temperature field and a process of formation of the vortical structures is presented in Rosa et al. (2011). Because the problem is symmetric with respect to the vertical axis it is sufficient to visualize and analyze evolution in only half of the domain. The symmetry of the solution was monitored during the experiment but no significant deviations have been observed. In order to verify the grid-convergence of the EULAG solution, a set of experiments employing various spatial resolutions was performed. Four different spatial resolutions were used, with the grid distances of 200, 100, 50 and 25 m, the same in horizontal and vertical directions. The snapshots of the potential temperature field after 15 minutes of evolution, obtained with different grid resolutions are presented in Fig. 1.
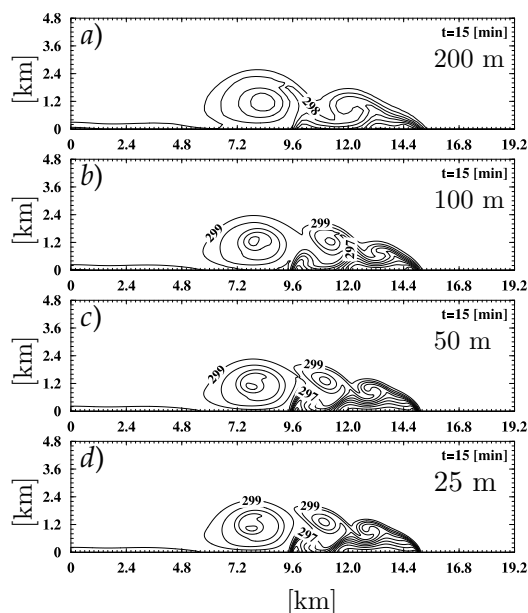
Figure 1: Plots of the potential temperature θ at 15 min for four different grid resolutions a) 200 m, b) 100 m, c) 50 m, d) 25 m computed using the EULAG model. Contour interval of the isentropes is 1 K.

It is seen, that there are no significant differences between potential temperature distribution obtained at resolutions between 25 m and 100 m. They all allow to identify the basic three-rotor structure of the flow, with a very small differences between the solutions obtained with 25 and 50 m resolutions. It shows that the EULAG simulation is grid-convergent and the simulation with the spatial resolution of 25 m can be regarded as the reference one, sufficiently resolving all scales of the flow, as is the case for the reference solution of Straka et al. (1993) employing also the grid size of 25 m.

Apparently, for the lowest grid resolution, applied (200 m), the flow is underresolved as after 15 minutes of the evolution only two well developed rotors are visible. This is similar to Straka et al. (1993) where 100 m spatial resolution was necessary to start capturing the three-rotor structure. On the other hand, solution provided by EULAG at 200 m has no numerical noise on the contrary to respective solution from Straka et al. (1993). Such robustness of the model is advantageous in NWP applications, where underresolved flow structures are unavoidable.

The quantitative comparison of the results of the EULAG simulation with the reference results from Straka et al. (1993) are presented in Table 1. They concern extreme values of

Table 1: Comparison of maxima and minima of p'-pressure perturbation, θ'-potential temperature perturbation, u-horizontal component of velocity and w-vertical component of velocity at 900 s for EULAG and Straka et al. (1993): REFC - the compressible model using unstaggered grid (resolution 25 m), REFS - the compressible model using a staggered grid (resolution 25 m), REFQ - the quasi-compressible model with unstaggered grid (resolution 25 m), for EULAG the grid size employed is shown. In the last row, location of the density current front (the $\theta' = -1^oC$ contour) from the EULAG simulations performed at four different grid resolution is given. REFC, REFS and REFQ values taken from Straka et al. (1993).

| Variable | REFC | REFS | REFQ | EULAG | | | |
				25 [m]	50 [m]	100 [m]	200 [m]
$p'_{max}(mb)$	2.87	2.49	1.74	1.67	1.66	1.47	1.49
$p'_{min}(mb)$	-5.14	-5.55	-5.21	-5.40	-5.34	-5.18	-5.04
$\theta'_{max}(K)$	0.00	0.00	0.00	0.00	0.00	0.00	0.00
$\theta'_{min}(K)$	-9.77	-9.77	-10.00	-9.96	-9.52	-9.24	-8.26
$u_{max}(m/s)$	36.46	35.02	34.72	35.06	35.26	35.26	33.48
$u_{min}(m/s)$	-15.19	-16.32	-15.31	-15.29	-15.11	-14.60	-13.68
$w_{max}(m/s)$	12.93	13.28	13.04	13.07	12.96	12.56	14.04
$w_{min}(m/s)$	-15.95	-16.11	-16.89	-15.94	-15.78	-15.41	-15.14
Front location (km) after 15 min	-	-	-	15.16	15.17	15.26	15.55

pressure perturbation, potential temperature perturbation and both components of velocity, after 15 minutes of the flow evolution. The names of the reference models presented in the current paper are consistent with the original notation used in Straka et al. (1993). The reference model simulations from Straka et al. (1993) are: compressible with unstaggered grid (REFC), compressible with staggered C-grid (REFS) and quasi-compressible with unstaggered grid (REFQ), each operating at 25 m resolution. EULAG results are presented for grid size ranging from 200 m to 25 m.

For most of the parameters, the EULAG simulation with 25 m resolution gives their values inside the interval defined by the values obtained with the reference compressible simulations employing staggered or unstaggered grid (it concerns minimum pressure perturbation (p), minimum and maximum wind (u), maximum vertical velocity (w); minimum (w) differs from the reference value from Straka by 0.01 m/s). The difference of the maximum potential temperature perturbation between EULAG and the reference compressible model from Straka et al. (1993) Straka is very small (in the range of 2%). The largest difference between compressible and EULAG solution concerns the maximum pressure perturbation being in the range of 1.2 hPa. To some degree it can result from the anelastic approximation of EULAG. On the other hand, the difference between the staggered and unstaggered compressible simulation reaches about 0.4 hPa.

Another quantitative analysis of model accuracy is based on comparison of the location of a cold front perturbation (after 15 minutes evolution of the current). A front location is defined as the place near the edge of the current where the perturbation potential temperature at the ground reaches 1 K. It is represented by the value of the x-coordinate at the location. In Fig. 2a, a front location from EULAG simulations are compared with the results of Straka et al. Straka et al. (1993). The reference data are taken from Table IV of Straka et al. (1993) and concern the simulations performed with the resolution of 200 m, except the results of fully compressible and quasi-compressible models REFC25, REFQ25,

computed with the grid size of 25 m. The EULAG results are presented for four different grid resolutions and are labeled as follows: 200 m − EULAG200, 100 m − EULAG100, 50 m − EULAG50 and 25 m − EULAG25. Additionally, the extreme values of potential temperature perturbation are plotted in Figs. 2b and 2c, for its minimum and maximum values, respectively. The differences between the solutions of different models, illustrated in Fig. 2,
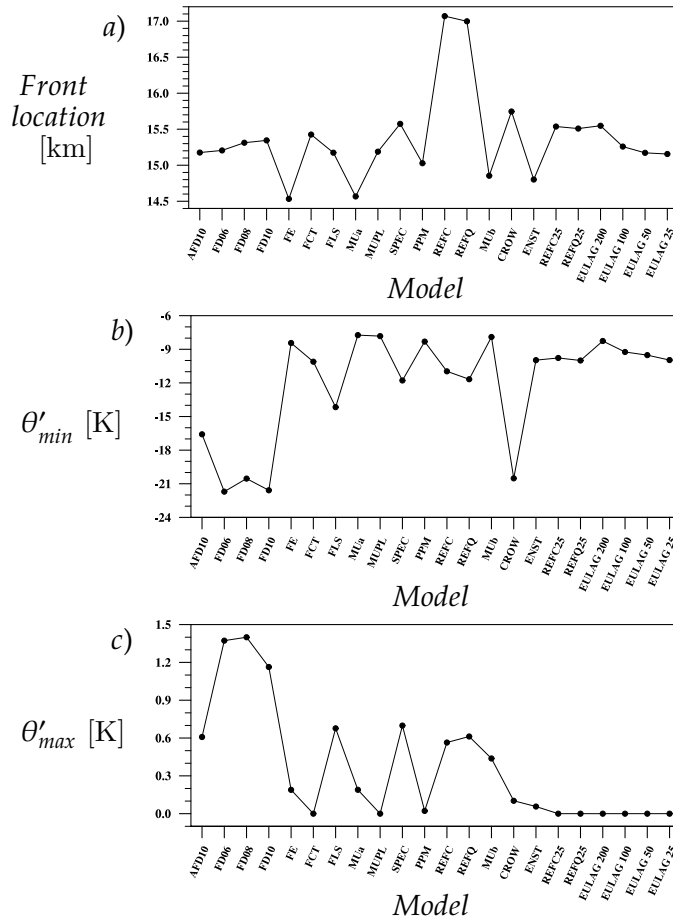
Figure 2: Quantitative comparison of front location and extreme values of potential temperature perturbation at t =15 min. Names of the models corresponds to acronyms used by Straka et al. (1993).

result both from differences in their analytical formulations and in their numerical design. However, analysis of Fig. 2a, showing the cold front location, leads to a general conclusion, that the differences resulting from analytical formulations of the models (compressible, anelastic, quasi-compressible) influence the solutions much less than the differences in the numerical schemes, employed. Note, that the majority of the models calculated with 200 m resolution (of all three analytical types, considered, including EULAG) give similar results in the range 14.5 km to 15.5 km, while the two outliers (giving very similar results of about 17.0 km) result from analytically differing compressible and quasi-compressible models. The detailed comparison of the simulations employing 200 m resolution with the reference, grid-convergent solution REFC25 (employing 25 m resolution and representing the 'true' value of about 15.5 km), confirms the above. Front positions similar to the reference one were achieved by both compressible (FCT) and anelastic models (both SPEC and EULAG). On the other hand, the results of the compressible model REFC and of the quasi-compressible model REFQ, calculated with 200 m resolution, differ significantly from the reference result. For both models, a relatively large error was a result of the under-resolving setup. This is not

the case for EULAG, as the difference between the solutions obtained with the 200 m and 25 m resolutions is relatively small. It shows reliable numerical properties of the model and confirms a grid-convergence of the solution that is very close to the reference compressible result.

The analysis of Fig. 2b, showing the minimum potential temperature perturbation after 15 minutes of evolution, leads to a similar conclusion. The majority of models using different analytical formulations give similar results being in the range of -14 K to -8 K (in a general agreement with the reference solution of -9.77 K). There are also outliers, resulting from quasi-compressible models, with much smaller values of the parameter. However, as not all quasi-compressible models are outliers, such a difference is a consequence of the numerics rather than of the analytical formulation. It is worth noting, also, that the outliers give reasonably good solutions for the front locations. This shows that the model comparison should not be limited to a single parameter only. Concerning EULAG simulations we observe both a good agreement with the reference solution from Straka et al. (1993) (-9.96 K for EULAG) and a grid-convergence to the EULAG reference solution employing 25 m grid size (see Tab. 1).

The analysis of Fig. 2c, showing the maximum potential temperature perturbation, allows for another quantitative comparison of the models. For this parameter the correct solution is known, as due to the adiabaticity of the process the actual value of the parameter is zero. Note, that the majority of the simulations performed with 200 m resolution gives incorrect results, including the compressible REFC model. However, as discussed above, these models give basically credible results for the front location and minimum θ'. The maximum potential temperature perturbation was correctly reproduced only by EULAG (anelastic), FCT (compressible), MUPL (quasi-compressible high-order accurate) and PPM (compressible high-order accurate).

The above analysis leads to the conclusion that for the problem at hand, the analytical formulation of the model equations does not have a significant impact on the simulation results, on the contrary to the numerics. The anelastic approximation allows for a correct representation of the dynamics of the system, provided the appropriate numerical design of the model, as is the case for EULAG. This result is in a general agreement with the analysis by Cullen et al. (2000) of the simulations of realistic mesoscale flow over the Scandinavian topography.

Optimal size of a time step for model integration is of great importance as it may significantly affect computational efficiency. The EULAG solutions presented above were obtained employing the same time step size as in Straka et al. (1993), i.e. 0.125 s. Additionally, several experiments with time steps increased by a factor of 2 up to 8 were performed. The tests were conducted at 100 m resolution and the results are presented in Rosa et al. (2011) Qualitative comparison of potential temperature field between solutions obtained for the original time step and the one being 8 times greater does not reveal any significant differences Rosa et al. (2011). A quantitative comparison in terms of a cold front location is presented in Table 2. The differences between the simulations for Courant numbers ranging from 0.045 to 0.36 are smaller than the grid spacing and the maximum relative difference between the solutions does not exceed 0.2 %. The presented results confirm that EULAG is not sensitive to such an increase of the Courant number.

Table 2: Front location at t=15 min and Courant number (CFL) for different time steps. Resolution is fixed at 100 m.

Time step size	CFL ($V_{max} = 36 m/s$)	Front location [m]
$dt_{Straka} = 0.125\ s$	0.045	15279
$2dt_{Straka} = 0.25\ s$	0.09	15276
$4dt_{Straka} = 0.5\ s$	0.18	15269
$8dt_{Straka} = 1\ s$	0.36	15260

2.3   Bubble convection test

The goal of the second experiment is to test the feasibility of the anelastic approach for modeling a system of two interacting density currents (warm and cold). Configuration of the experiment follows the setup proposed originally by Robert (1993). The original experiment was performed employing fully compressible model, defining a suitable benchmark for the EULAG anelastic solution.

In the experiment the atmosphere is isentropic, thus the potential temperature of the reference state is $\theta = 300$ K. The reference profile of density for the EULAG simulations is the same as used for the cold density current (Straka test). Moist processes such as condensation, evaporation or rain formation are not considered. The initial conditions are set similarly to the Robert's experiment Robert (1993). The two bubbles are defined as perturbations of potential temperature with a Gaussian profile. The maximum values of temperature perturbation are 0.5 K for the warm bubble and −0.15 K for the cold one. Domain covers an area of 1 km × 1 km. Simulations are performed at three different resolutions 16 × 16, 8 × 8 and 4×4 m². Free-slip, rigid boundary condition are imposed on each side of the computational domain. The time step is set to $\Delta t = 1$ s. Pure Eulerian set of governing equations is used without any sub-grid scale model for viscosity. There is no external flow so that dynamics is governed only by density currents.

Figure 3 presents results of the EULAG simulation performed at the resolution 8 × 8 m², as results employing two other resolutions do not reveal substantial differences, during the 10 minutes of simulations. Robert (1993) performed the original experiment at the resolutions of 10 × 10 and 5 × 5 m². Comparing Fig. 3 with the benchmark results from Robert (1993) (Figs. 8 and 9 therein) we conclude that the differences between fully compressible and anelastic models are visually hardly to notice, which confirms the EULAG abilities to correctly represent the complicated and highly nonlinear processes.

2.4   Numerical modeling of inertia-gravity waves

In this section we demonstrate EULAG capabilities for simulating two-dimensional inertia-gravity waves. The waves are excited in air flowing through a long, periodic channel via an initial perturbation of potential temperature. The experiment was proposed by Skamarock and Klemp (1994) and is widely used for testing numerical schemes of the meteorological models.
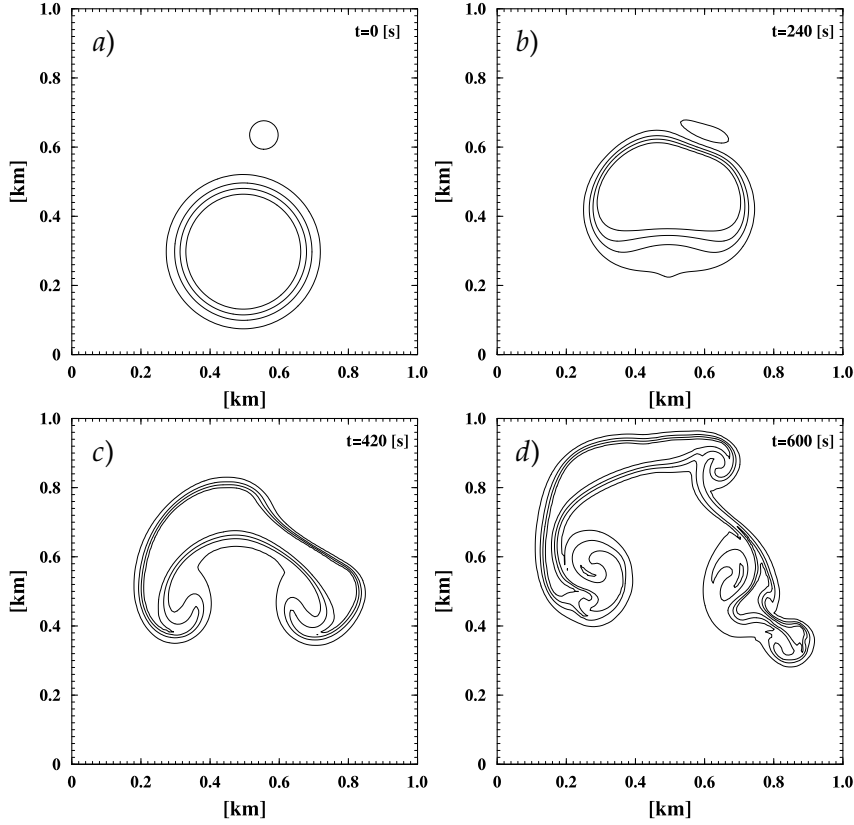
Figure 3: Time evolution of potential temperature perturbation θ' at $t = 0, 240, 420$ and 600 s. The initial distribution is depicted in panel *a*. The flow is induced by a rising large warm bubble and a descending small cold bubble. The asymmetry results from initial horizontal displacement between centers of the two bubbles.

2.4.1   Experiment setup

The computational domain is a periodic flat channel with solid, free-slip upper and lower boundaries. The simulations are performed for two different lengths of the channel, namely 300 km and 6000 km, and the same domain height of 10 km. The atmosphere inside the channel is uniformly stratified with a Brunt-Väisälä frequency equal to 0.01 s^{-1}. Constant horizontal ambient flow at an inlet is set to 20 m/s. The spatial distribution of the potential temperature perturbation, which leads to excitation of the gravity waves is defined as

$$\theta'(x, z, t = 0) = \Delta\theta_0 \frac{sin(\pi z/H)}{1 + (x - x_c)^2/a^2},$$ (1)

where $H = 10$ km is a domain height and $\Delta\theta_0 = 10^{-2}$ K is small amplitude of initial perturbation. The center of the initial perturbation x_c depends on the length of the channel and is 100 km for the short (300 km) and 2000 km for the long (6000 km) one. The half-width of the initial perturbation a also depends on the domain length and is $a = 5$ km and 100 km for the short and the long channel respectively. For the short channel, the resolution of computational grid in horizontal and vertical direction is the same. Simulation in a long channel is performed on a grid with an aspect ratio $\Delta x/\Delta z = 20$. Coriolis force is considered in both simulations, but its significant contribution to the flow dynamics is observed only for the long channel. Similarly to the previous experiments, there is no surface friction nor viscosity. More details about the experiment setup can be found in Skamarock and Klemp (1994).

2.4.2 Short channel

First, we analyze EULAG results for simulations performed for the short channel and the Boussinesq set of governing equations. In order to test the grid convergence of the solution, three different grid resolutions, namely $\Delta x = \Delta z = 1$ km, 0.5 km and 0.25 km are used. Figure 4 compares the perturbation of potential temperature at t = 50 min for the analytical solution (a) with numerical results ($b-d$), computed at the three grid resolutions. It is seen, that the numerical solutions converge to the analytical one with decreasing grid sizes.
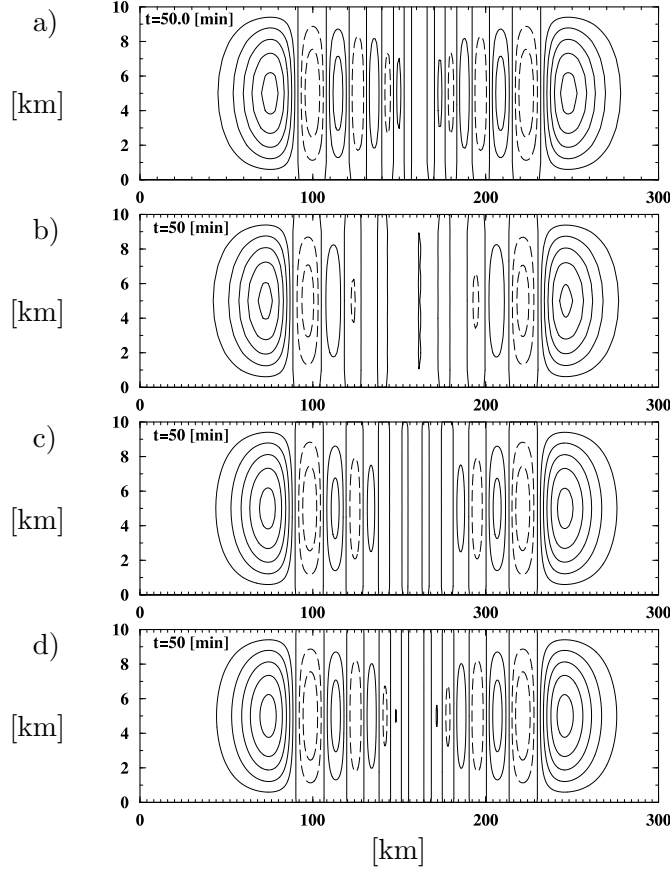
Figure 4: Spatial distribution of the potential temperature perturbation θ' after $t = 50$ min plotted (using contour values between -0.0015 K and 0.003 K) with a contour interval of 0.0005 K. Comparison of analytical solution a), with numerical solutions based on Boussinesq approximation computed using three different grid resolutions b) $\Delta x = \Delta z = 1$ km, c) $\Delta x = \Delta z = 0.5$ km, d) $\Delta x = \Delta z = 0.25$ km; negative values dashed.

In the original numerical experiment by Skamarock and Klemp (1994), the grid size was fixed to $\Delta x = \Delta z = 1$ km. Our result at this resolution (Fig. 4c) is very similar to that benchmark (see their Fig. 1c). Nevertheless, such grid size still does not allow to fully resolve the flow, which motivated us to apply higher resolutions, as described above.

Additionally, Fig. 5 compares the analytical solution for the potential temperature perturbation at constant height of 5 km above the surface (red line), with the EULAG results at three grid sizes, employed (black lines). Although small differences between numerical and analytical solutions are noticeable, the convergence to the analytical one is clearly visible. As the resolution of computational grid increases, the differences between numerical and analytical solutions diminish quickly, except the most central part of the wave-train, where 0.25 km grid size still underresolves the flow.
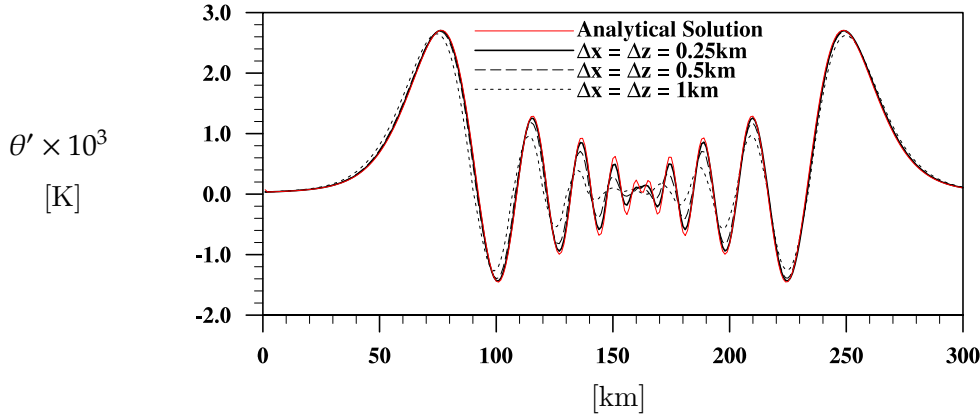
Figure 5: Profiles of potential temperature perturbation θ' along 5000 m height for the analytical solution and three different grid resolutions presented in Fig. 4.

2.4.3 Long channel

For the experiment involving 6000 km domain we used longer time step $t = 200$ s (previously 1 s), longer simulation time equal 1000 min, and different initial location of temperature perturbation ($x_c = 2000$ km). The computational grid has the same number of nodes in every direction, what implies a relatively large aspect ratio $\Delta x / \Delta z = 20$. As discussed in Skamarock and Klemp (1994), simulating atmospheric flows on grids with such high aspect ratio could be challenging for compressible models based on explicit numerical schemes. For such models, vertically propagating acoustic modes are disruptive for the slower modes of physical interest. Here, we intend to show that the numerics of EULAG provide a stable and accurate solution.

Figure 6 presents a comparison between the analytical and EULAG's numerical solutions for the potential temperature perturbation at 1000 min computed on grids with sizes of (20 km × 1 km, 10 km × 0.5 km and 5 km × 0.25 km), in horizontal and vertical directions, respectively. For different resolutions, the general pattern is similar but some differences in temperature gradients on the lateral sides of the perturbation are noticeable. With increasing resolution, the differences between the analytical and numerical solutions diminish significantly and we can conclude that the EULAG numerical solution is grid-convergent to the analytical formula. Similar to the short channel experiment, the highest resolution employed locally underresolves the potential temperature distribution, this time at the sides of the wave-train.

It is also interesting to analyze the grid convergence more quantitatively. Figure 7 presents the distribution of the potential temperature perturbation along the horizontal line at 5 km height. It confirms the grid-convergence of the numerical solutions, showing also that the largest differences between the analytic and numerical solutions can be found in the regions of high horizontal gradients of θ'.

Additional results from EULAG simulations performed using linearized version of the governing equations and pseudo-incompressible system of Durran (1989) one can find in Rosa et al. (2011).

2.5 Modeling of mountain gravity waves

The aim of that class of experiments is a comparison of the anelastic EULAG simulations of mountain flows with results of compressible models by Bonaventura (2000) and Pinty et al.
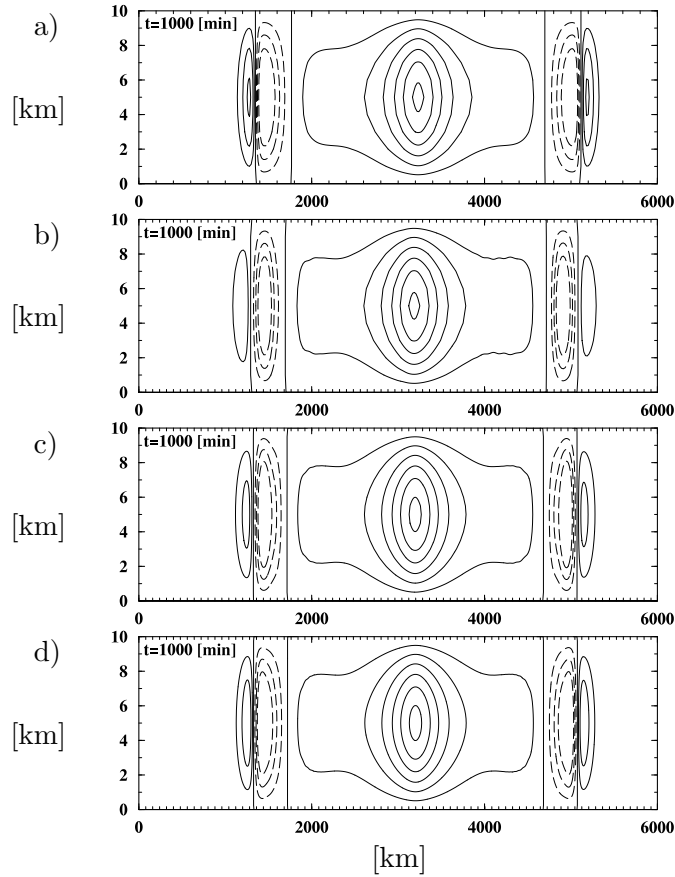
Figure 6: Spatial distribution of the perturbation of potential temperature θ' after $t = 1000$ min plotted with a contour interval of 0.0005 K. Comparison of analytical solution *a*) with the numerical solution based on Boussinesq approximation computed with three different grid resolutions *b*) $\Delta x = 20$ km, $\Delta z = 1$ km, *c*) $\Delta x = 10$ km $\Delta z = 0.5$ km, *d*) $\Delta x = 5$ km $\Delta z = 0.25$ km; negative values dashed.
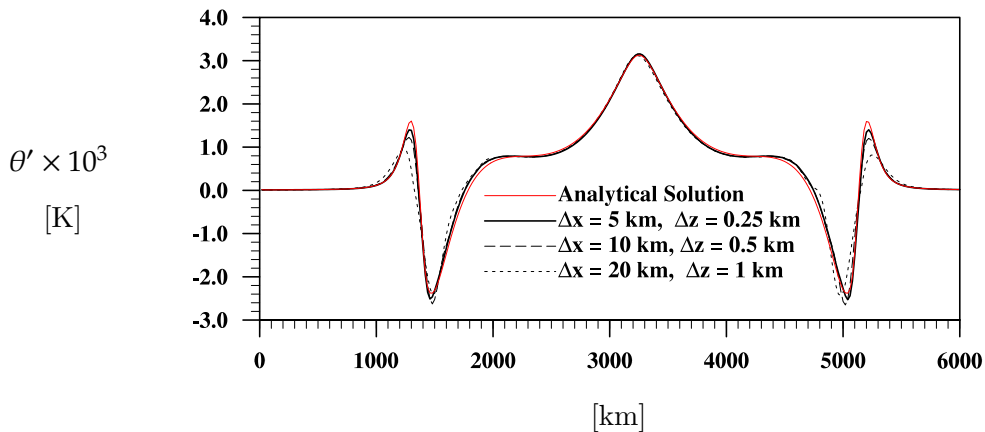
Figure 7: Profiles of potential temperature perturbation θ' along 5000 m height for the analytical solution and three different grid resolutions presented in Fig. 6.

(1995). The experiments are performed for different flow regimes, such as linear hydrostatic, linear nonhydrostatic, nonlinear hydrostatic and nonlinear nonhydrostatic.

2.5.1   Experiment setup

The flow configurations are based on Bonaventura (2000) and Pinty et al. (1995). The shape of the hill is defined by the Agnesi formula:

$$h(x) = \frac{h_0}{1 + [(x - x_0)/a]^2}, \qquad 0 \le x \le L, \tag{2}$$

where h_0, x_0 and a are height, center location and half width of the hill, correspondingly. The parameters defining shape of the hill define also a flow regime, so they differ between the simulations.

For all simulations, the reference potential temperature is given by the Clark-Farley formula. Height of the computational domain is 25 km, while its length depends on the particular flow regime. In order to avoid reflections of the gravity waves from the upper and lateral boundaries, absorbing layers are applied. Thickness and strength of the lateral damping layer depends on the flow regime. In vertical direction, the absorbing layer is the same for each experiment and covers the whole domain above 10 km height. There is no Coriolis force, nor explicit viscosity nor surface friction in the simulations.

2.5.2   Linear hydrostatic regime

The linear hydrostatic regime is characterized by the nondimensional parameter $aN/U \approx 10$ and a very small aspect ratio of h_0/a. An initial horizontal velocity U is 32 m/s. Height and half width of the hill are $h_0 = 1$ m and $a = 16$ km, correspondingly. Computational grid has significant anisotropy. Its size in the horizontal direction is $\Delta x = 3$ km while in the vertical direction it is $\Delta z = 250$ m. While the grid size in the vertical direction is much larger then the height of the hill, its presence is defined via terrain following coordinates. Brunt-Vaisala frequency is set to $N = 0.0187$ s^{-1} and the time step $\Delta t = 40$ s.

An analytical stationary solution for the wind perturbation for linear hydrostatic wave regime was developed by Klemp and Lilly (1978), for compressible atmosphere. Therefore, accuracy of the numerical solution can be directly verified against this result. Figure 8 shows a comparison of EULAG horizontal wind after 11.11 hours integration with that analytical solution. The general agreement between the solutions is apparent and is seen especially in the velocity pattern. The small differences concern mainly wave amplitudes, which are about 5% smaller for EULAG, in the areas outside the absorber. While Pinty and Bonaventura did not present a direct comparison of their simulation results with the analytical solution, we can conclude that the EULAG velocity distribution is in a close agreement with their compressible solutions.

2.5.3   Linear nonhydrostatic regime

For the linear nonhydrostatic flow regime we chose the nondimensional parameter aN/U to be of the order of 1, and the hill aspect ratio slightly smaller than 1. Thus, the hill shape parameters are $a = 500$ m and $h_0 = 100$ m for $N = 0.0187$ s^{-1} and $U = 14$ m/s. Resolution of computational grid is $\Delta x = 100$ m in horizontal and $\Delta z = 250$ m in vertical direction, to follow possibly closely a configuration applied by Bonaventura (2000). Time step used for the integration is $\Delta t = 4$ s. Distribution of the velocity and vertical momentum flux is analyzed after 1.2 h. In normalized time scale it corresponds to $t^* = Ut/a = 120$ and we can expect that they are close to the stationary solutions.
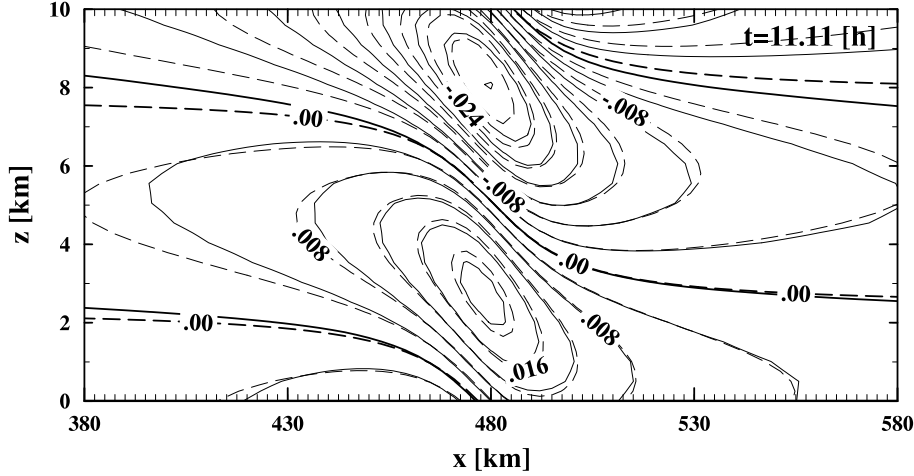
Figure 8: Perturbation of horizontal component of velocity after 11.11 hours. Comparison of numerical EULAG's solution (solid lines) with analytical solutions (dashed lines).

Vertical and horizontal components of velocity from EULAG are plotted in Figs. 9a and 9b. Their comparison with the compressible results from Bonaventura (2000) (Fig. 5 therein) shows that the characteristic features of the flow are properly reproduced and this concerns especially the pattern amplitude of the vertical velocity distribution. The small difference between the anelastic and compressible solution by Bonaventura is noticeable in the direction of the wave propagation, as in the EULAG solution, the waves propagate more steeply. Precise determination of this difference is somehow problematic due to limited resolution of Bonaventura's figure. Nevertheless, it can be said that the difference in the direction of the wave propagation does not exceed 5 degrees.
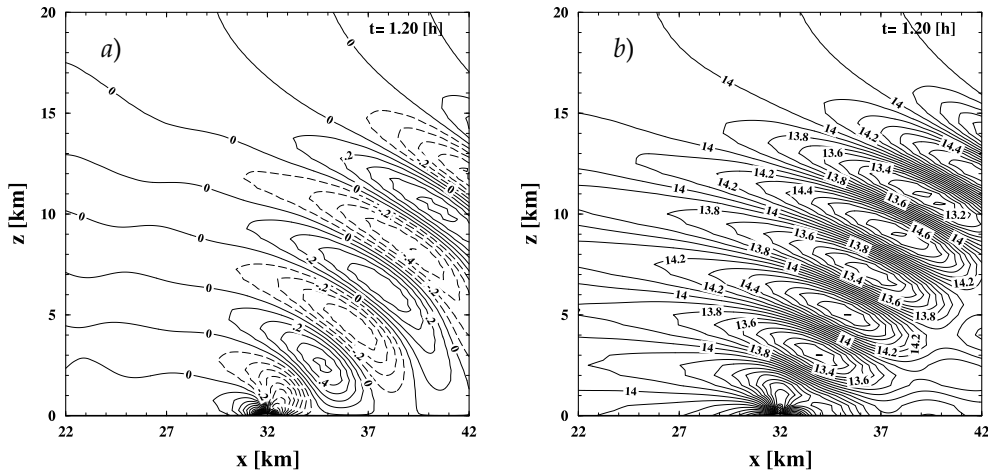
Figure 9: Velocity flow field in linear nonhydrostatic regime. Vertical a) and horizontal b) component of velocity (after 1.2 hour) computed using EULAG code, contours every 0.1 m/s.

2.5.4   Nonlinear hydrostatic regime

Nondimensional parameter aN/U for this test is equal 10. The mountain shape parameters are $a = 16$ km and $h_0 = 800$ m, while $U = 32$ m/s. Brunt-Vaisala frequency for this simulation is slightly increased $N = 0.02$ s^{-1}. Grid size is $\Delta x = 2.8$ km in the horizontal and $\Delta z = 200$ m

in the vertical direction. The whole domain covers the area of 1728×25 km. The equations are integrated over 23.9 h with the time step $\Delta t = 30$ s.

Figure 10 presents EULAG results for vertical and horizontal components of velocity perturbation. The comparison of the vertical velocity perturbation (Fig. 10b) with corresponding results from Pinty et al. (1995) (see their Fig. 8b) shows that both solutions are characterized by similar velocity pattern, as well as positions and magnitudes of the velocity extrema. This is also the case for the horizontal velocity perturbations, as both models place its first maximum at 8 km height with maximum value of about -3.5 m/s and the first minimum at ~ 9 km height with value -25 m/s for EULAG and ~ -26 m/s for Pinty et al. (1995). Also, the EULAG solution is more smooth in the upper part of the domain.
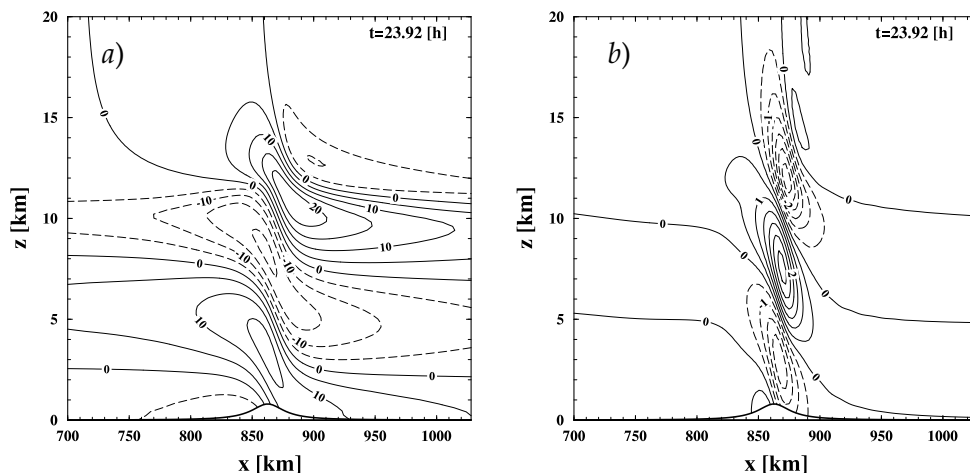
Figure 10: Spatial distribution of velocity perturbation in the hydrostatic nonlinear regime *a*) horizontal component with contour interval every 5 ms^{-1}, *b*) vertical component with contour intervals every 50 cms^{-1}. The dashed line indicate negative values.

2.5.5 Nonlinear nonhydrostatic regime

The nonlinear, nonhydrostatic flow regime is characterized by nondimensional parameter aN/U equal 1.5. Complexity of the flow results from the high steepness of the hill characterized by $a = 1000$ m and $h_0 = 900$ m giving a relatively high aspect ratio $h_0/a = 0.9$. Initial velocity at the inlet is set to $U = 13.28$ m/s. Brunt-Väisälä frequency is $N = 0.02$ s^{-1}. Resolution of the computational grid is $\Delta x = 200$ m in horizontal and $\Delta z = 100$ m in vertical direction. Size of the domain is 127.8×25 km. The experiment is run for 2400 s with the time step of 4 s. In EULAG simulations the hill is represented using the terrain following coordinates, while the Bonaventura's model uses Cartesian rectangular coordinates with step-like representation of the orography.

Figure 11 shows the EULAG solutions for vertical and horizontal components of velocity after 2400 s of calculations and, similarly to Bonaventura, focuses the analysis on the lee-side of the hill. The comparison with the compressible model of Bonaventura (2000) shows that even for this highly complicated flow regime and differing representations of orography, the main characteristic features of the flow are the same for both models. For horizontal velocity, they show similar spatial perturbation structure, with the area of positive perturbation elongated just above the lee-side slope. In EULAG solution, center-line of the area is closer to the ground comparing with the Bonaventura's solution and the difference may result from different representations of orography pattern. Maximum value of the horizontal wind inside the perturbation area and located close to the mountain peak is 25 m/s in EULAG and
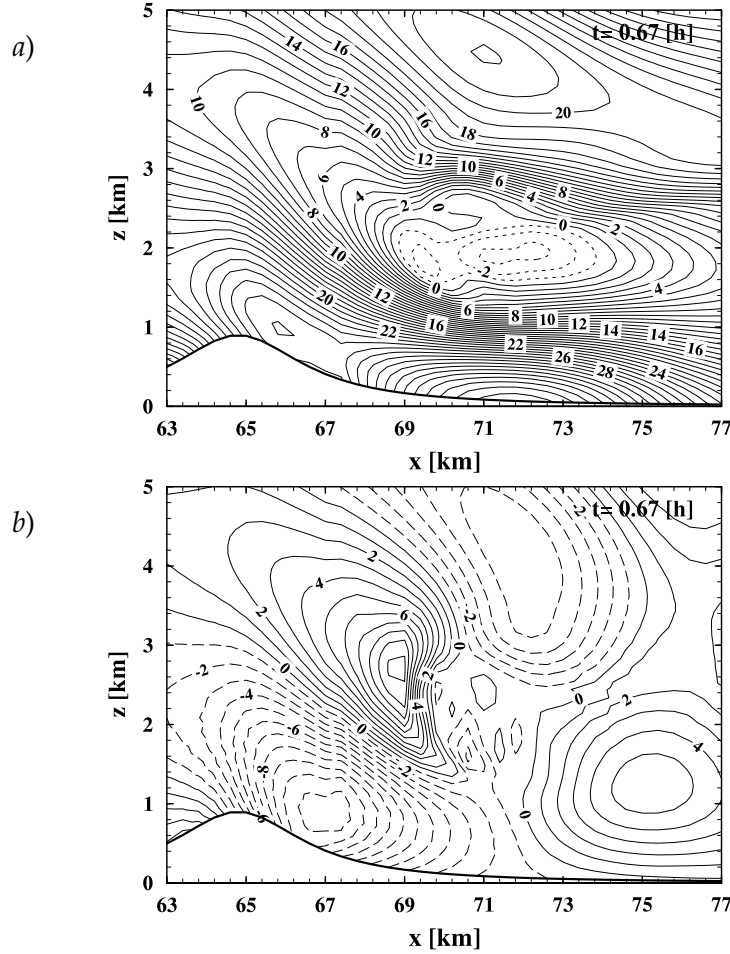
Figure 11: Velocity flow field in nonhydrostatic nonlinear regime *a*) EULAG - horizontal wind perturbation with contour interval 1 m/s, *b*) EULAG - vertical velocity with contour interval of 1 cm/s.

27.9 m/s in Bonaventura's solution. Region of negative horizontal velocity is also similar in location and shape with the corresponding region in the Bonaventura's solution Bonaventura (2000)(Fig. 15 therein). The minimum value of the horizontal velocity in EULAG is $\sim$ -3 m/s while in the Bonaventura's solution is slightly smaller and equal ~ -5 m/s.

Vertical velocity field on the lee side of the hill (Fig. 11) is organized into a quadrupole structure. The flow pattern, as well as the position of minima and maxima are consistent with results obtained with compressible model (see Fig. 16 in Bonaventura (2000)).

In summary, the results show that anelastic approximation does not impose any significant limit for accurate modeling of the mountain gravity waves for tested flow regimes, including the nonlinear nonhydrostatic one, featuring also a strong wave-breaking process.

2.6   Summary and conclusions

The paper presents results of the study aimed at testing the anelastic dynamical core of the multiscale research flow model EULAG. The study is focused on the two-dimensional dry flows, free of phase transitions of water vapor. All the tests show that the results obtained using the anelastic EULAG core agree to a high degree with the benchmark compressible solutions, for all analyzed classes of the flow. This is also the case for comparisons with the

analytical solutions, where they are obtainable, that is for the inertia gravity waves, as well as for the orographic waves in the linear and hydrostatic flow regime. Additionally, the tests confirm the robustness of the EULAG numerical design.

The test of Straka et al. (1993) allows to thoroughly analyze the properties of EULAG via comparison of its solutions with results of an ensemble of fluid models of different analytic and numerical designs. The analysis confirms that the differences between the reference compressible benchmark solution and results of other simulations depend rather on their numerical designs and not significantly on their analytical formulations, with the anelastic EULAG solutions being very close to the benchmarks ones. In this sense, the experiment confirms findings by Cullen et al. (2000) concerning an influence of numerical model design on realistic representations of mesoscale flows over Scandinavian Peninsula. Our analysis shows also that EULAG solutions well represent the flow structure, even underresolved by the model. That virtue characterizes a small minority of the tested models, not even the benchmark one of Straka et al. (1993).

In summary, the analysis of EULAG results and its comparison with the benchmark solutions confirms that the model has a number of characteristics desirable from the view point of mesoscale NWP applications. They involve the high degree of conformity with the benchmark results, as well as consistent and smooth representation of subscale process, always present in NWP applications.

References

W. C. Skamarock, J. Doyle, P. Clark, and N. Wood. A standard test set for nonhydrostatic dynamical cores of NWP models. *16th Conference on Numerical Weather Prediction, Seattle WA*, P2.17, 2004.

J. M. Straka, R. B. Wilhelmson, L. J. Wicker, J. R. Anderson, and K. K. Droegemeier. Numerical-solutions of a nonlinear density-current - A benchmark solution and comparisons. *International Journal for Numerical Methods in Fluids*, 17(1):1–22, 1993.

A. Robert. Bubble convection experiments with a semi-implicit formulation of Euler equations. *Journal of the Atmospheric Sciences*, 50(13):1865–1873, 1993.

W. C. Skamarock and J. B. Klemp. Efficiency and accuracy of the Klemp-Wilhelmson time-splitting technique. *Monthly Weather Review*, 122(11):2623–2630, 1994.

L. Bonaventura. A semi-implicit semi-Lagrangian scheme using the height coordinate for a nonhydrostatic and fully elastic model of atmospheric flows. *Journal of Computational Physics*, 158(2):186–213, 2000.

Y. Ogura and N. A. Phillips. Scale analysis of deep and shallow convection in the atmosphere. *Journal of the atmospheric sciences*, 19:173–179, 1962.

B Rosa, M. J. Kurowski, and M. Ziemianski. Testing the anelastic nonhydrostatic model EULAG as a prospective dynamical core of a numerical weather prediction model. Part I - dey benchmarks. *Acta Geophys.*, 59:1236–1266, 2011.

M. Cullen, D. Salmond, and P. K. Smolarkiewicz. Key numerical issues for the future development of the ECMWF model. *Proc. 2000 Workshop on developments in numericsal methods for very high resolution global models*, pages 183–206, 2000.

D. R. Durran. Improving the anelastic approximation. *J. Atmos. Sci.*, 46:1453–1461, 1989.

J. P. Pinty, R. Benoit, E. Richard, and R. Laprise. Simple tests of a semiimplicit semi-lagrangian model on 2d mountain wave problems. *Monthly Weather Review*, 123(10):3042–3058, 1995.

J. B. Klemp and D. K. Lilly. Numerical-simulation of hydrostatic mountain waves. *Journal of the Atmospheric Sciences*, 35(1):78–107, 1978.

3 Moist benchmark experiments with the anelastic EULAG model

Marcin J. Kurowski, Bogdan Rosa, Michał Z. Ziemiański

Institute of Meteorology and Water Management - National Research Institute, Poland

3.1 Introduction

In this section, the results of two moist benchmark tests (Klemp and Wilhelmson 1978, hereafter KW78; and Weisman and Klemp 1982, hereafter WK82) performed by the EULAG model for convection-permitting scales are documented. The both experiments consider development and evolution of a three-dimensional supercell over a flat terrain. Our strategy follows the idea of Skamarock et al. (2004), in which supercell experiments define one of the tests regarding standard verification of nonhydrostatic dynamical cores. Since the problem is strongly nonlinear and moist processes are coupled with three-dimensional dynamics, the supercell simulations are considered one of the most complex cases proposed in the test set. This is also because supercell formation involves a variety of coupled microphysical and dynamical aspects, including ice processes, gust fronts and cold pool dynamics, mesocyclone formation, forward and rear downdrafts, storm splitting, surface inflow, and multi-phase precipitation. However, a basic requirement of the test is to reduce relevant physics in order to facilitate evaluation of the results. In consequence, a set of simplifications was imposed on the experimental setup, e.g., moist physics is limited to bulk parameterization allowing only for warm rain formation. Nonetheless, the simplified setup is suitable for studying supercell development and to qualitatively reconstruct the most typical storm features, as shown in KW78 and WK82. The results of severe convection simulations presented in this report along with a set of additional sensitivity studies performed by EULAG were already published in the scientific literature (Kurowski et al. 2011).

3.2 General model setup

The two experiments presented in this report (i.e., KW78 and WK82) use a highly consistent numerical setup but different initial and boundary conditions. All simulations are carried out in a horizontally homogeneous environment and in the absence of orography. The reference profiles are based on observations and represent realistic conditions for severe storm development. The moist framework of EULAG is based on the Lipps and Hemler (1982) approach. The EULAG's reference (environmental) state is defined by the profiles of temperature and potential temperature (what allows for a derivation of reference pressure used in the moist thermodynamics), water vapor mixing ratio and both components of horizontal velocity. The initial perturbation of the potential temperature has a form of bubble with positive temperature excess in the center gradually decreasing to zero at its edge. It is placed near the ground in order to initiate convection. The Coriolis effect is not taken into account.

The bulk moist thermodynamics is represented in the model by three prognostic variables: water vapor (q_v), cloud (q_c) and rain (q_r) mixing ratios (cf. eqs. 1b, 1c and 1d from Grabowski and Smolarkiewicz, 2002). Condensation and evaporation processes are based on an instantaneous saturation adjustment (i.e., no supersaturation) while rain development is represented through a Kessler scheme. Respective mathematical formulas describing the processes of autoconversion, accretion, evaporation and rain subsidence along with a set of accompanying parameters follow KW78.

The subgrid-scale (SGS) mixing scheme (Margolin et al., 1999) is based on the prognostic equation of a volume averaged turbulent kinetic energy (TKE), which is subsequently used to prescribe the subgrid-scale turbulent mixing coefficient for momentum: $Km = c_m TKE^{1/2}(\Delta x \Delta y \Delta z)^{1/3}$, where c_m is a constant. As in KW78, the Prandtl number (i.e. $Pr = K_m/K_h$, where K_h is the subgrid-scale mixing coefficient for scalars) is 0.33. Because some of the SGS parameters of the KW78 scheme are not given explicitly, the subgrid-scale model used in KW78 may differ from the model employed in EULAG.

Rigid and free-slip boundary conditions are imposed at the top and bottom of the domain. The model's lateral boundaries are defined as follows: each explicit variable (i.e. the potential temperature, momentum, mixing ratio, etc.) has an inflow boundary value which is defined by a constant in time environmental profile; processes taking place within the domain do not affect the inflow conditions; the actual state of the flow is a superposition of the reference state and a perturbation; the perturbations are advected out of the domain at the outflow boundary by a prescribed environmental flow. We will further refer to this type of boundary condition as open. When absorber of the Davies type (Davies, 1976; Smolarkiewicz and Margolin, 1997; see discussion after eq. 9 and eqs. 17a-17d) is applied then the perturbations are attenuated to zero in this region. It helps to control an excess and propagation of gravity waves in a stably stratified atmosphere. If not otherwise stated, the sponge layer is not applied. This is because the effects of gravity wave propagation were found to be insignificant for the short-term integration time. We also tested periodic boundary conditions, and, as will be shown further, the choice between open and periodic b.c. is of negligible importance to the EULAG's solutions.

3.3   Klemp and Wilhelmson (1978) experiment

3.3.1   Setup details

The KW78 experiment represents a classic study on a supercell formation, however, it does not provide the details of initial soundings applied in the model. The approximate profiles subjectively reproduced from a skew-T diagram (cf. Fig. 1 in KW78) are given in Table 3. A well-mixed boundary layer extends in the lowest part of the atmosphere (up to 1600 m), with two layers of different stability aloft, having an interface at about 6 km. Convective available potential energy (CAPE) is about 1400 J with the lifted condensation level located at 870 mb. It should be stressed that skew-T representation is a source of insufficient information and a small modification of the initial conditions significantly affects CAPE. For instance, an ensemble of a few profiles within an envelope not exceeding 0.3 K, with respect to the values given in Table 3, changes CAPE by about 5%. The initial perturbation of the potential temperature is defined in the same way as in KW78 (cf. eq. 4.1 and 4.2 therein) and is placed near the ground in the center of the domain. Moist initial fields are not affected by this perturbation and water vapor mixing ratio changes only according to the sounding. Surface pressure is 965 hPa. The model timestep is 10 s and a total integration time is 24 min for a case with no external flow, 36 min for the simulation with a shear flow and 40 min for a case with a veering wind profile. Two sets of simulations are reported here. One does not include any explicit turbulent diffusion (NSG). The other uses the SGS scheme. Basic domain size is 24 km × 24 km × 10 km with a uniform grid spacing $\Delta x = \Delta y = 1$ km and $\Delta z = 500m$. Since the size of a developing supercell is relatively large compared to the domain, we also performed sensitivity study for domains of 36 km × 36 km × 10 km and 256 km × 256 km × 10 km with the same spatial resolution as for the basic simulations. This is to verify how convective development depends on the proximity of lateral boundaries and on the volume of the surrounding where subsiding air may differently respond to the strong

convective updraft.

Table 3: Initial profiles of height (z), pressure (p), potential temperature (θ), temperature (T), dew point temperature (Td) and water vapor mixing ratio (qv) used in KW78 experiment. Surface pressure is $965hPa$.

z [m]	p [Pa]	θ [K]	Td [K]	qv [g/kg]
0	965	300.19	290.15	$1.32 \cdot 10^1$
137	950	300.22	289.45	$1.28 \cdot 10^1$
600	900	300.25	287.05	$1.14 \cdot 10^1$
1083	850	300.17	284.25	$9.99 \cdot 10^0$
1587	800	300.83	281.05	$8.48 \cdot 10^0$
2116	750	302.85	276.95	$6.76 \cdot 10^0$
2675	700	305.44	271.25	$4.77 \cdot 10^0$
3267	650	308.36	256.15	$1.84 \cdot 10^0$
3897	600	311.44	244.85	$6.26 \cdot 10^{-1}$
4574	550	314.89	230.35	$1.66 \cdot 10^{-1}$
5303	500	318.83	215.95	$3.73 \cdot 10^{-2}$
6097	450	323.3	201.65	$6.83 \cdot 10^{-3}$
6968	400	328.52	187.25	$9.47 \cdot 10^{-4}$
7937	350	334.41	172.85	$9.41 \cdot 10^{-5}$
9029	300	341.43	158.35	$5.99 \cdot 10^{-6}$
10285	250	351.73	142.15	$1.38 \cdot 10^{-7}$

3.3.2   Atmosphere-at-rest case

Comparison of EULAG's results for simulations with and without explicit subgrid-scale mixing is presented in Fig. 12 and should be compared with Fig. 2 from KW78. Note that zero isoline is not plotted for positive defined fields such as cloud and rain mixing ratios in contrast to the plots from KW78. The results of the simulations are in qualitative agreement with KW78, that is, the dynamic and thermodynamic fields have similar patterns. A general picture of the process compares well with the reference experiment, however, some differences can be found in details. SGS model reduces the strength of convection and leads to suppressed cloud and rain development. This effect is physical and shows an influence of enhanced subgrid-scale diffusion on water species. A better consistency with KW78 is obtained when no sugbrid-scale diffusion is applied, however, the results still suggest a possible deficiency in the initial sounding. The EULAG's dynamical fields such as vertical velocity are similar to KW78, except that maximum updraft velocity is 24 m/s in KW78, 21 m/s and 18 m/s in NSG and SGS simulation, respectively. As for the moist fields, the vertical extent of convection as seen by the cloud top level (defined by the height of $q_c = 0.5$ g/kg isoline) reaches 6.5 km (SGS) or 7.5 km (NSG). These are smaller than about 8 km in KW78. Similarly to KW78, a vortical structure of cloud water is visible around the cloud base for NSG. Such a pattern is also present in SGS simulation, but for a smaller isoline interval than used in Fig. 12. The most significant differences regard maximum values of the rain field, which are strongly reduced especially for SGS case. This is a straightforward consequence of
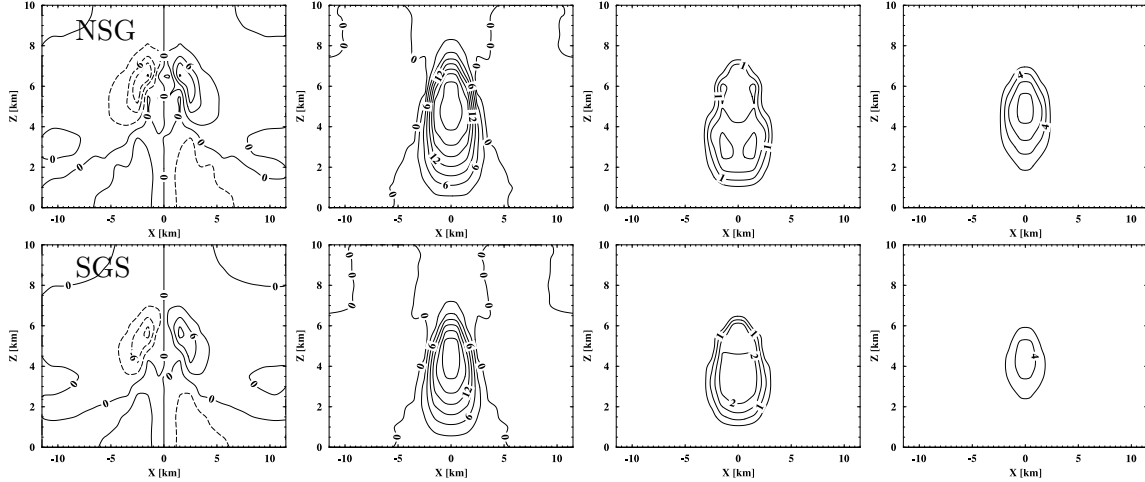
Figure 12: Starting from left column: vertical cross section of u (m/s), w (m/s), q_c (g/kg) and q_r (g/kg) at y = 0 for simulation in resting atmosphere. Results for NSG (upper row) and SGS (right column) are plotted at t = 24 min. Intervals between the isolines exactly correspond to those used in KW78. Negative values of velocity are dashed.

lower amount of cloud water converted into rain water, accordingly to the Kessler formula. Maximum isoline of q_r is 12 g/kg in KW78, 8 g/kg in NSG and 4 g/kg in SGS case.

A significant difference in the moist fields between SGS and NSG models illustrates an important role of diffusion in controlling the supercell formation. This is especially important for the large-gradient fields as narrow convective updraft that impinges upon the dry environment. The diffusion can reduce buoyancy of a rising thermal what in turn limits moisture supply. On the other hand, our sensitivity study shows that at 24 min the cell undergoes a vigorous development characterized by intensive growth of maximum updraft velocity and maximum values of water species. Therefore, even relatively small differences in model speed-up may lead to significant differences between models, at this moment. The comparison of the results at a more mature stage of the cloud development would be more illuminating, but KW78 does not offer such results for the atmosphere-at-rest case. Nonetheless, this example illustrates the complexity of a seemingly simple problem, where the coupling between dynamics and moist thermodynamics with precipitation may result in noticeable model-to-model differences in physically important fields such as cloud and rain water.

3.3.3   Shear flow case

A low-level shear is an essential component of a supercell formation as it is responsible for the storm splitting with subsequent separation of updraft and downdraft structures. This process is initiated when a vorticity tube associated with the low-level vertical shear flow is tilted up by a convective current and subsequently deformed into two separate horizontally counter-rotating branches of the air (e.g. Klemp, 1987). A low-level shear is a necessary prerequisite of the process but it also affects the vertical structure of the supercell, which may be torn apart when the shear is too strong (Weisman and Klemp, 1982). In the current simulations, a horizontal velocity in x-direction changes linearly from -5 m/s at z = 0 km to 5 m/s at 3.25 km and remains constant (5 m/s) above.

Horizontal cross sections of vertical and horizontal velocites, and cloud and rain water mixing ratios at 24 min and 36 min are presented in Fig. 13 and Fig. 14, respectively, and should be compared to Fig. 4 and 5 from KW78. Cloud water shown in Fig. 13 is replaced with the
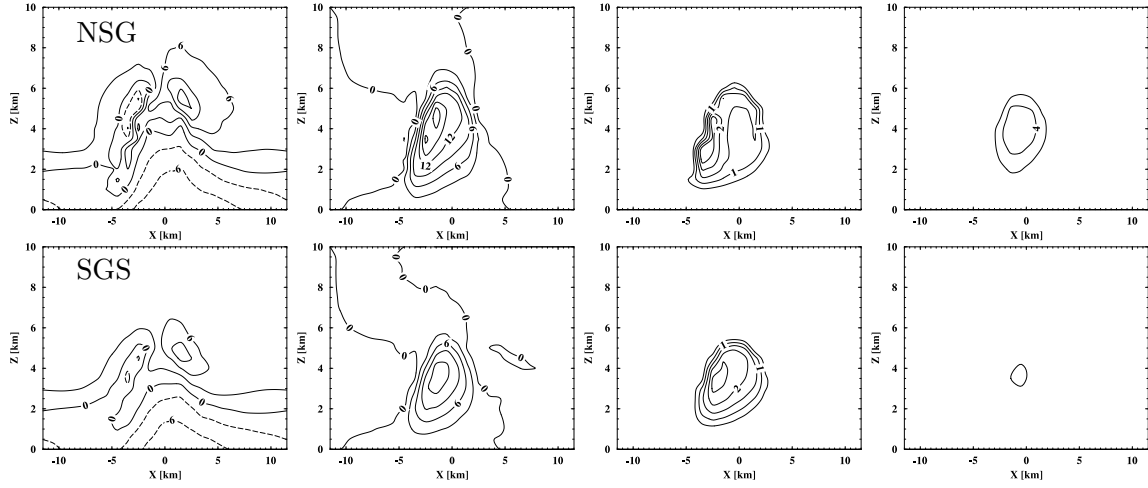
Figure 13: As in Fig. 12 but for sheared environment at 24 min.
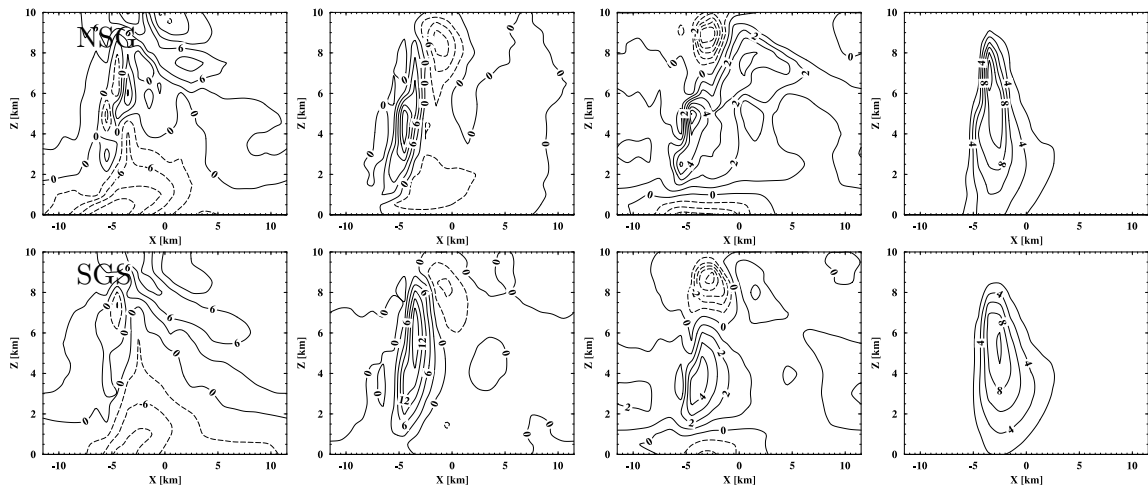

Figure 14: As in Fig. 13 except at 36 min and the third column is potential temperature perturbation (θ') in (K).
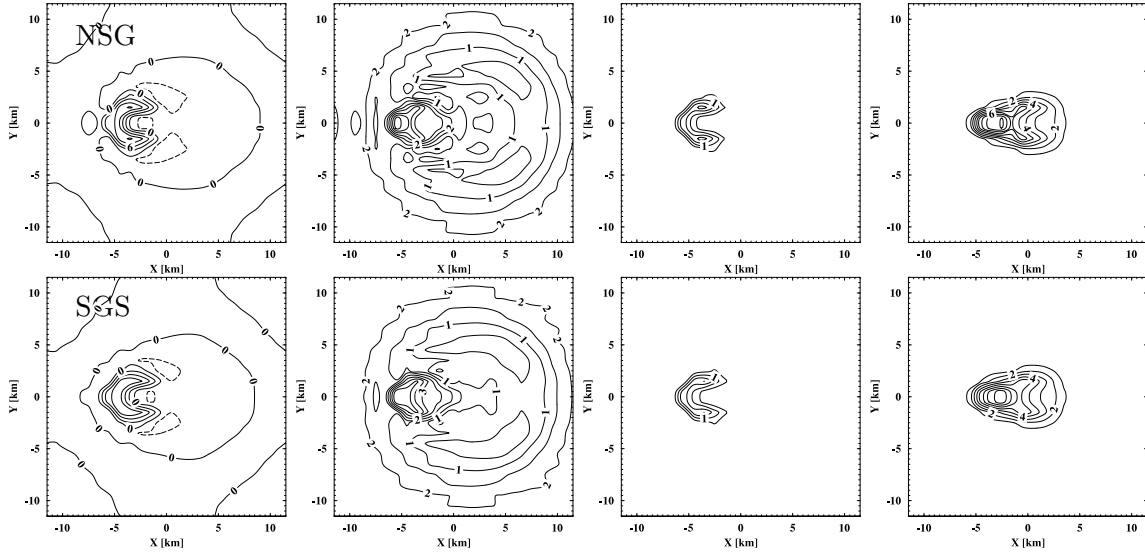
Figure 15: Horizontal cross sections at $z = 2.75$ km for one-directional shear simulations at 36 min. From left to right: vertical velocity, potential temperature perturbation, cloudy and rain water are presented for NSG (top row) and SGS (bottom row) model.

potential temperature fluctuation in Fig. 14, in agreement with Fig. 5 from KW78. Again, all the fields are in qualitative agreement with KW78 and a general picture of supercell formation in sheared environment is similar in both cases. The main differences regard the amount of rain water that is lower in the EULAG simulations. The rain water mixing ratio is especially reduced at 24 min for SGS case. This is associated with approximately 40% lower intensity of a convective updraft and thus lower moisture supply. At later times, the EULAG results compare better with KW78. For instance, after 36 min cloud and rain fields are very close to KW78. NSG model produces slightly more rain than is seen in the reference experiment as a small region of high rain water amount ($q_r > 12$ g/kg) is present in between 6 and 7 km. Rain water advected into upper parts of the supercell by a strong updraft overshoots the cloud top height (not shown) by about 2.5 km. Maximum potential temperature excess resulting from the latent heat release (4 K in EULAG simulations) compares well with KW78. As shown in Fig. 14, results of SGS model at 36 min are more consistent with KW78 than at 24 min, and only a slight delay of rain fallout is present (note that isoline of 4 g/kg have not yet reached the ground).

Horizontal cross sections of vertical velocity, potential temperature perturbation and cloud and rain mixing ratios at $z = 2.75$ km and at 36 min are depicted in Fig. 15 using the same intervals as in Fig. 6 from KW78. A characteristic horse-shoe-shaped deformation of an updraft region with the two nearly separate convective branches marks the beginning of the storm splitting. Rain water and potential temperature fields still have only one maximum, similarly to KW78. The rain water at 2.75 km, falling out between convective updrafts, covers larger horizontal area than the cloud water. As discussed above, the difference between EULAG and KW78 at 24 min can be due to different model spin-up. A longer integration time removes transient differences in moisture supply. In consequence, similar intensity of an updraft is achieved at later times and thus the cumulative total water amount is more consistent in both cases.

z [m]	u [m/s]	v [m/s]
0	-6.0	2.0
500	-3.5	1.7
1000	-1.3	1.0
1500	0.5	-0.5
2000	2.25	-2.4
2500	3.1	-4.2
3000	4.0	-6.0
3500	5.3	-5.1
4000	6.7	-2.5
4500	8.5	1.0
5000	10.3	4.8
5500	12.1	8.8
6000	13.8	12.5
6500	14.3	13.8
7000	14.8	15.0
7500	14.8	15.0
8000	14.8	15.0
8500	14.8	15.0
9000	14.8	15.0
9500	14.8	15.0
10000	14.8	15.0

Table 4: Numerical values of both components of horizontal velocity (u, v) as used in EU-LAG's simulation of the flow with a veering wind.
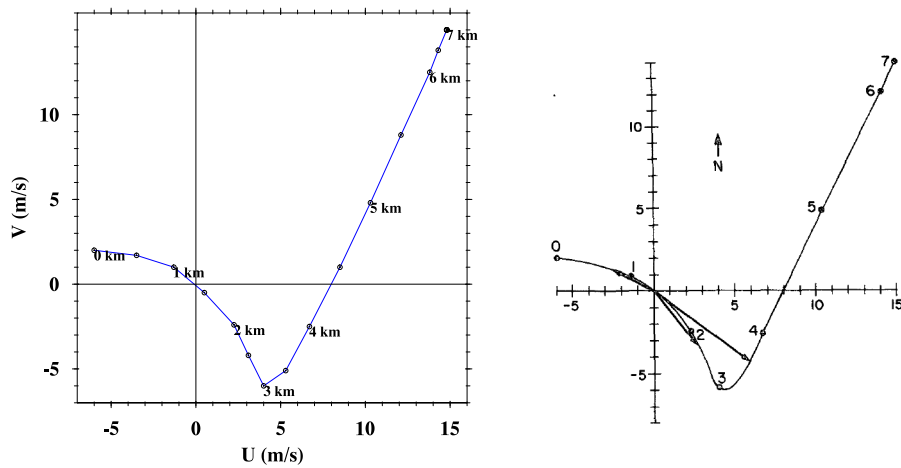

Figure 16: Hodograph of the horizontal velocity as used in EULAG's simulations (left panel) and that from the original KW78's setup (right panel). Empty circles on the left panel indicate the values exactly at model's vertical levels, i.e. the distance between adjacent points is $\Delta z = 0.5$ km.
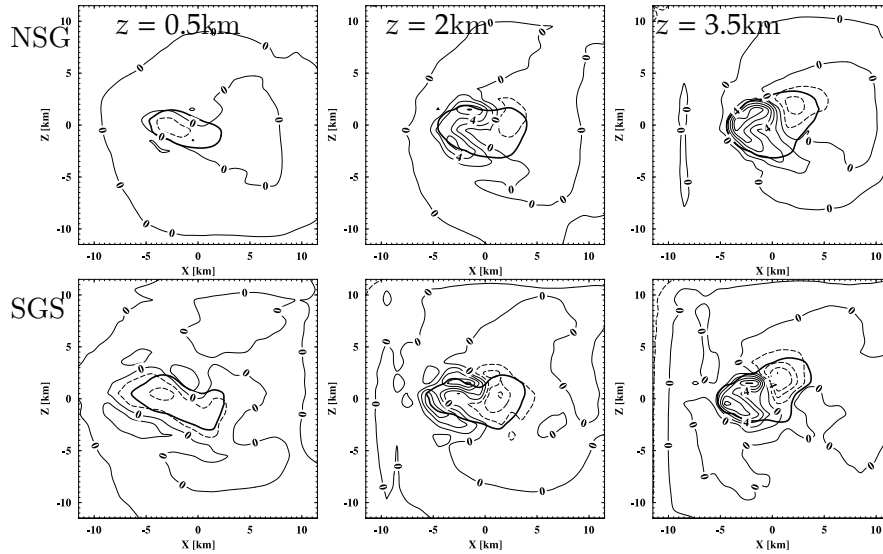
Figure 17: Horizontal cross sections of the vertical velocity w for veering wind simulation at three different levels: 0.5 km (left column), 2 km (middle) and 3.5 km (right) and after 40 min of simulation. Thick line denotes rain water contour of $q_r = 1$ g/kg.

3.3.4   Veering wind case

A case with a veering wind is the most complex out of the three presented in this study and most typical for severe storm formation (KW78). For a straight hodograph used in the previous case along with the Coriolis force omitted, supercell development is symmetric to the XZ plane at y = 0 and none of the branches is favored (cf. Fig. 15). Presence of veering wind, however, causes asymmetry in the supercell propagation and strongly affects evolution of its internal structure. This allows for a development of new characteristics that resemble supercell features observed in nature.

The environmental profile of horizontal velocity shown in Fig. 16 was reproduced from Fig. 12 in KW78 and appropriate numerical values used for the study are given in Table 3.3.4. Figure 17 presents horizontal cross sections of the vertical velocity and rain water fields after 40 minutes of simulation at three different levels: 0.5 km, 2 km and 3.5 km (using the same contour intervals as in KW78) for NSG and SGS simulations. The results were obtained for slightly larger horizontal domain size (i.e. 32 km × 32 km) in order to minimize boundary effects.

The structure at z = 0.5 km consists of two updrafts separated by rain-laden downdraft. The convective branches merge at upper levels where asymmetry of the structure is evident. The branch of stronger updraft borders upon the downdraft and the convection is more vigorous than at lower levels. The rain water contour of 1 g/kg at z = 0.5 km encloses only a region of the descending air. At upper levels, the region expands into an area where the updrafts are also present. Maximum value of the vertical velocity is similar to that from KW78, but about 25% lower for SGS model. YZ vertical cross sections of cloud and rain water as well as vertical velocity and potential temperature perturbation at x = -2 km are depicted in Fig. 18. The vertical velocity field has two updrafts in the lower part of the supercell which are merged together in the upper part. There is a region of negative velocity in between the convective branches, close to the ground, which is associated with a cold pool formation.

The potential temperature field is separated into three regions, as in KW78. The amplitude of its perturbation near the cloud top reaches -6 K in KW78 and -4 K in both EULAG
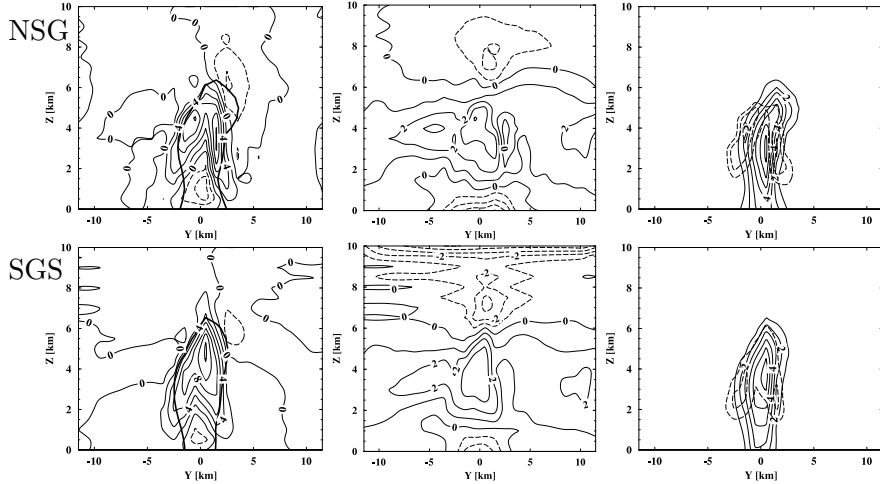
Figure 18: Vertical cross section along yz direction at $x = -2$ km after 40 min: w field (m/s) (left) with bold solid line enclosing the region of $q_r > 1$ g/kg, θ' (K) (middle), and water fields (g/kg) (right) where dashed line refers to q_c and the solid line to q_r.

simulations. The maximum positive temperature excess is 3 K in all cases. The cold pool at the bottom of supercell is characterized with temperature decrease to -4 K in KW78, -4 K for NSG and -3 K for the SGS model. The cloud and rain patterns have similar structure as in KW78 except that the maximum values of q_r are 8 g/kg in both EULAG simulations and 4 g/kg in KW78. The cloud top level reaches about 8.5 km in NSG, 8 km in SGS and 7 km in KW78 simulations.

3.3.5   Sensitivity tests

The influence of horizontal domain extent, the type of lateral boundary condition and spatial resolution were investigated in a series of sensitivity tests. As for the horizontal extend of the domain, the proximity of lateral boundaries noticeably suppresses vertical supercell development. This is evident for the maxima of rain water and updraft velocity, which are about 20% and 40% larger for 256 km × 256 km domain than for 24 km × 24 km one, at 24 and 36 minutes, respectively. The spread of the results for different domain sizes depends on the environmental flow and is generally the smallest for the veering wind where at 40 min of evolution the spread is about 20% for q_r and q_c and about 40% for maximum updraft velocity. The largest differences concern maximum updraft velocity for the atmosphere at rest, where w varies between 6 and 16 m/s at 40 min. The comparison suggests that in general terms the presence of external flow, allowing for convection organization, makes representation of convection less dependent on the model setup.

Changes in horizontal and vertical gridlength turned out to have a dominant impact on the supercell dynamics. According to the results, larger values of the extrema are generally obtained for a finer grid resolution. The strongest sensitivity is observed for maximum vertical velocity which increases from about 26 m/s for $\Delta x = 1$ km and $\Delta z = 500$ m to about 34 m/s for $\Delta x = 500m$ and $\Delta z = 170m$. Changes in resolution also affect the moist fields. Notice however, that doubling horizontal resolution (i.e. using $\Delta x = 500m$ instead of $\Delta x = 1$ km) leads to relatively small changes in the evolution of q_c and q_r extrema, whereas modification of the vertical grid has a significant impact on the fields. Another observed effect is earlier development of convection for finer grid resolution. This indicates that a simple comparison of instantaneous fields may lead to misleading conclusions, especially

when similarly evolving supercells are only shifted in time for different model setups.

The experiments with different types of boundary conditions show that the choice between open and periodic b.c. is of negligible importance to the EULAG results. The spread of results for the updraft velocity, cloud and rain mixing ratio for the most complex case (with a veering wind) is at least an order of magnitude smaller than that introduced by other modifications (i.e., resolution and domain size). For the atmosphere-at-rest case the differences between the two types of boundary conditions in terms of vertical velocity and water condensate did not exceed 0.1%.

3.4 Weisman and Klemp (1982) experiment

3.4.1 Setup details

Setup of the experiment is based on the analytic profiles of the potential temperature, relative humidity and uni-directional horizontal wind (cf. eq. 1, 2 and 4 from WK82) extending vertically up to 17.5 km. Horizontal and vertical gridlength is 2 km and 350 m, respectively. WK82 employs vertical stretching from 350 m near the ground to about 1 km at the top of the domain. This is the main difference from the EULAG's setup which employs a uniform grid. Based on the symmetry of the problem, WK82's horizontal domain was limited to one-half, in order to reduce computational cost. In contrary, we use a full domain with a horizontal size of 128 km × 128 km. This size was found to be optimal for representing propagation of supercell during the storm splitting without any noticeable interference with the lateral boundary effects. Initial perturbation of the potential temperature is similar to KW78 experiment, but the temperature excess is now 2 K. Open boundary conditions, a Kessler-type warm rain parametrization and a TKE-based subgrid-scale mixing scheme are employed in the experiment. EULAG's physics and numerics are the same as in the previous experiment. This is in contrast to WK82, where a modified version of KW78 model was used (cf. section 2 in WK82). Again, neither ice processes nor Coriolis effects are included. Total integration time is 120 min. It is worth mentioning that a SGS model is a necessary prerequisite for the simulations as the lack of subgrid-scale transport leads to disintegration of a well-organized internal supercell structure.

3.4.2 Shear flow case

The environmental horizontal shear flow employed in the simulations is defined as follows: $U(z) = U_s tanh(z/z_s)$, where $z_s = 3$ km, and U_s is a free parameter which changes in the range from 5 m/s to 45 m/s (see Fig. 2 in WK82 and its explanation in the text). We consider five cases, namely $U_s = 5$ m/s, 15 m/s, 25 m/s, 35 m/s and 45 m/s. A constant wind U of a different strength for different simulations is added as Galilean transformation to keep the supercell in the middle of the domain during the simulation. Its magnitude is chosen experimentally and depends on U_s. Using a constant U does not affect the solution since free-slip bottom boundary condition is imposed and no surface fluxes are applied.

Results of the simulations for this setup are presented in Figs. 19, 20 and 21 in a similar manner to WK82. Each figure shows the time evolution of the following fields: horizontal flow at 175 m height (black vectors), vertical velocity at 4900 m (black lines, dashed for negative values), surface precipitation (light blue lines) and a cold front defined as the edge of a cold pool ($\Delta\theta = -1K$) at the surface (bold blue line). Dotted area marks region of q_r >2 g/kg at the ground. In addition, results from WK82 are plotted in the figures. Such representation of the storm development gives an insight into the supercell dynamics, however, WK82 does not

show any vertical cross sections of the storm structure, what precludes more comprehensive comparison of the results. Note that a mean horizontal flow ($\bar{U}$) of different magnitude was subtracted from EULAG and WK82 solutions, what affects representation of storm-relative low level flow (e.g. to keep the solution for U_s =15 m/s in the domain center, $\bar{U}$=9.15 and 12m/s were used in EULAG and WK82, respectively).

The storm system evolves in a similar way for three different values of U_s (Figs. 19, 20 and 21). After 40 min of simulations the storm splitting is already underway, but only one maximum of the surface precipitation is being formed. Apparently, horizontal extent of convective perturbations depends on the shear strength. For larger U_s the fields become more asymmetric in x and y directions. This reduces the maximum updraft velocity due to lower moisture supply. This in turn suppresses precipitation-laden downdraft and delays formation of a cold pool, as compared to the other cases. After 80 min, each supercell consists of two clearly separated convective cores with a precipitation area between them. Again, intensity and horizontal extent of the vertical velocity and rain water fields decreases with increasing U_s. After 120 min, the splitting of the surface precipitation is completed for $U_s = 25$ m/s and $U_s = 35$ m/s as the rain pattern no longer extends over a single area. A local circulation within each core induces a downdraft in its rear part which diverges near the ground away from the supercell center. The largest velocity of diverging flow is for $U_s = 15$ m/s. These velocity perturbations are superimposed on the external flow that results in larger western component of horizontal velocity for greater U_s. A cold pool develops on the rear side of the supercell with a cold front located near the leading edge of the convective structure during the whole simulation. One of the most characteristic features is that the distance between the two convective branches almost does not depend on the shear-strength. It differs less than a few percent for U_s ranging from 15 to 35 m/s. The shear mostly affects the supercell evolution through the intensity of convection.
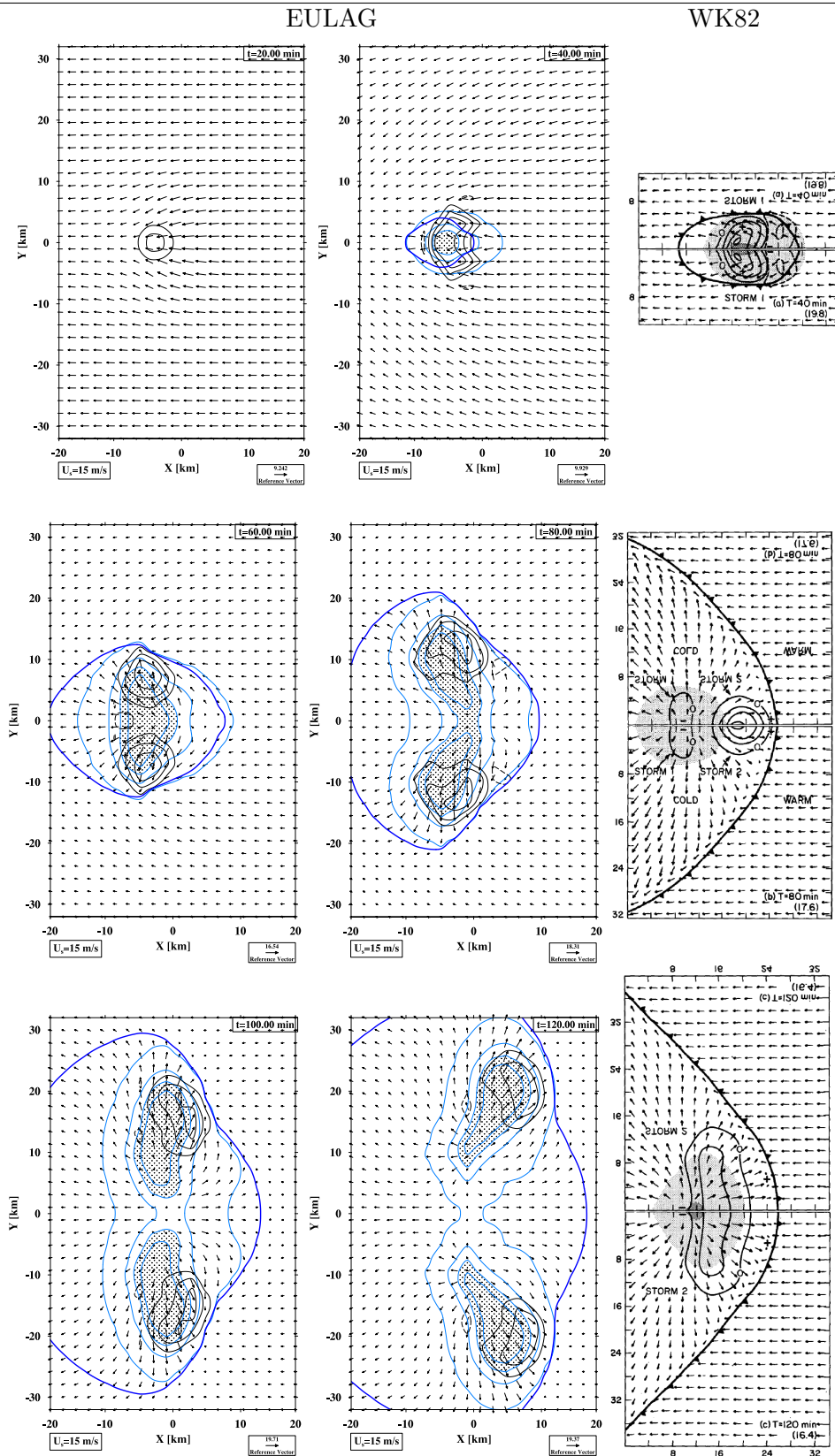
Figure 19: Time evolution of horizontal flow at 175 m (black vectors), vertical velocity at 4900 m (black lines, dashed for negative values), surface precipitation (light blue lines) and a cold front defined as the edge of a cold pool ($\Delta\theta = -1$K) at the surface (bold blue line). Dotted area marks region of $q_r > 2$ g/kg at the ground. Vertical velocity is contoured every 5 m/s for positive values and 2 m/s for negative values. Surface precipitation is contoured every 1 g/kg. The results are plotted for $U_s = 15$ m/s. Right column represents the results from WK82 experiment).

EULAG   WK82
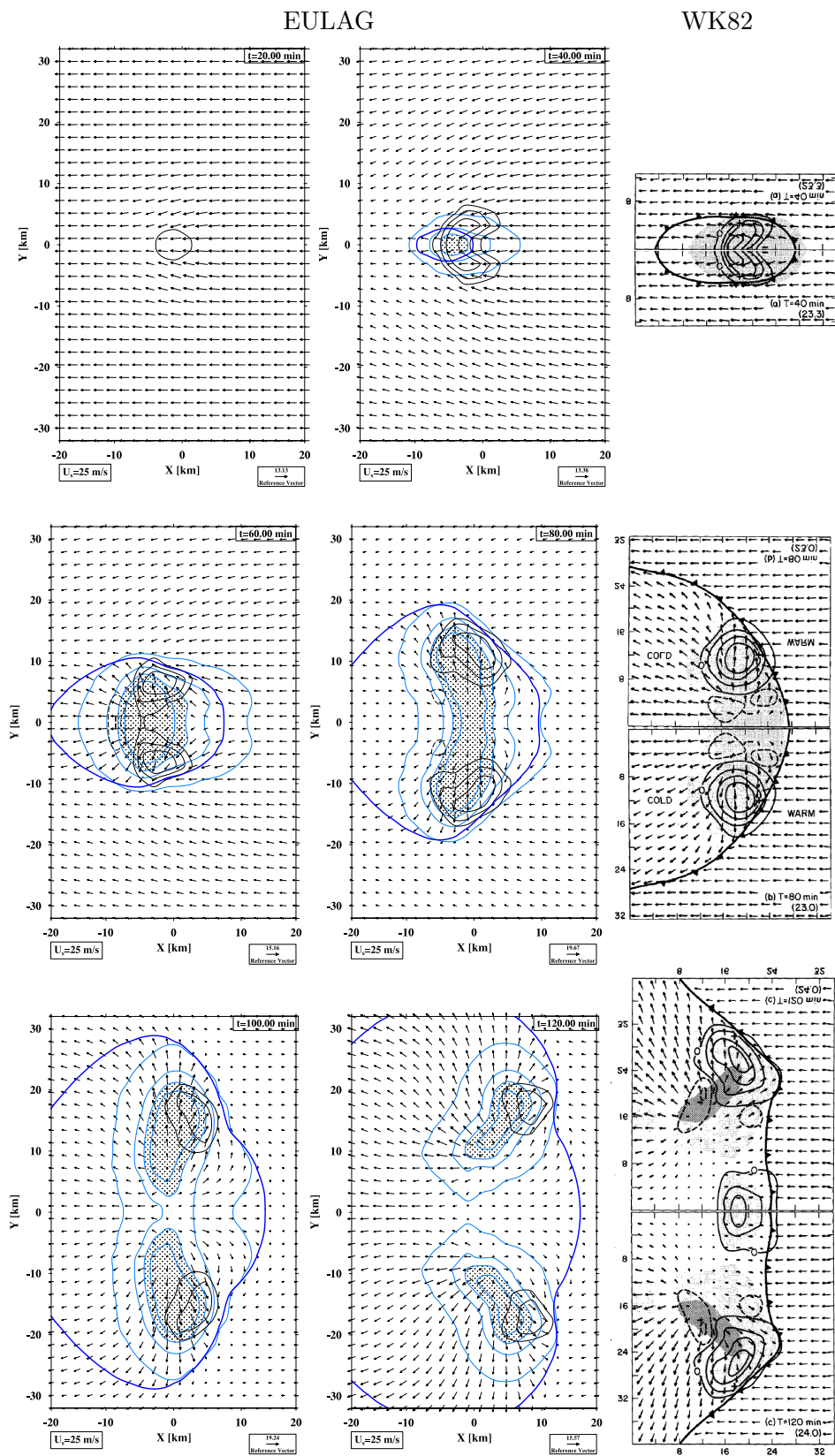
Figure 20: Same as in Fig.19 but for $U_s = 25$ m/s

EULAG   WK82
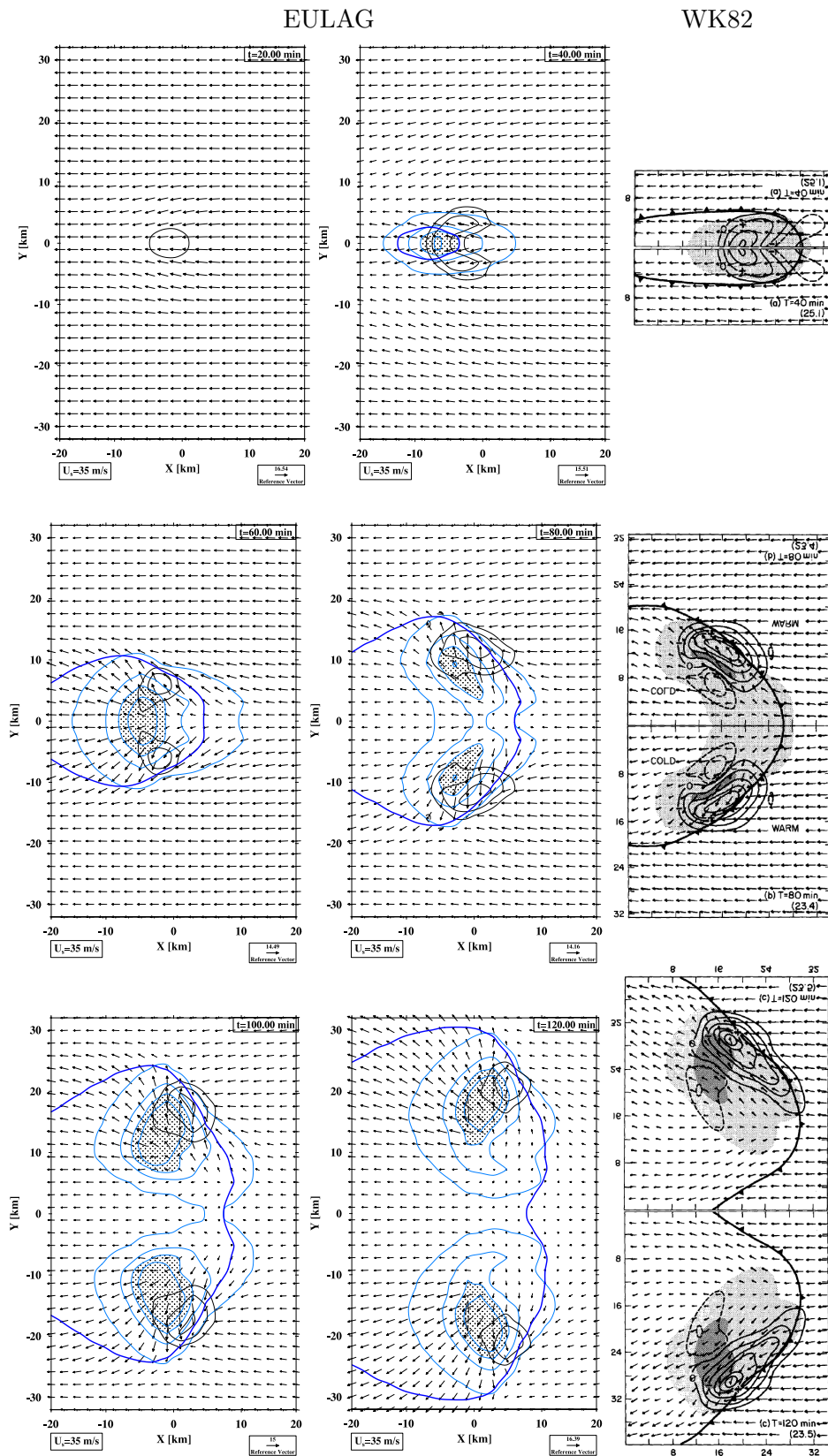
Figure 21: Same as in Fig.19 but for $U_s = 35$ m/s
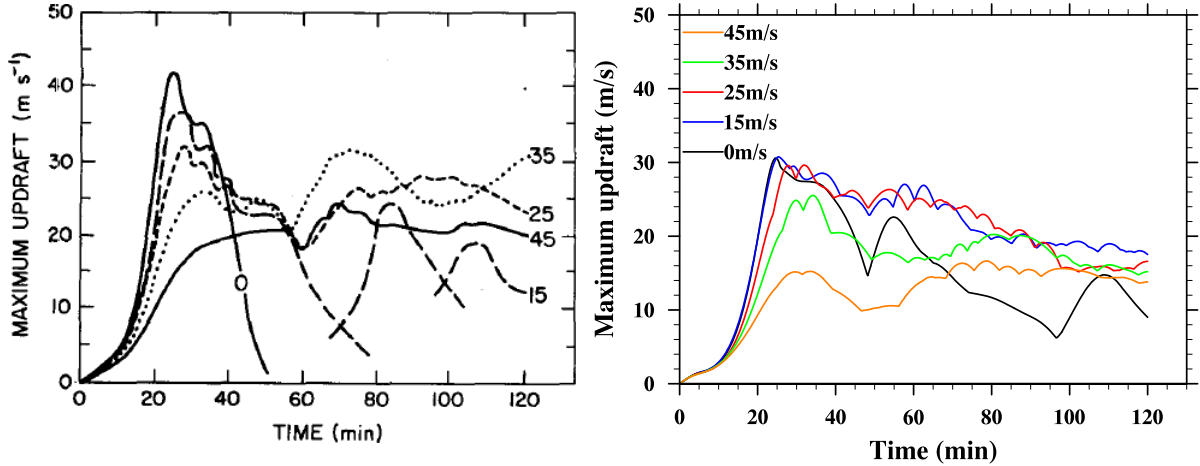
Figure 22: Comparison of the time series of maximum vertical velocity for simulations with different U_s. The results from WK82 (left) and EULAG (right) are shown.

Comparison of the results with WK82 shows that EULAG correctly reconstructs the convective process leading to formation of storm splitting and a cold pool. The main difference concerns buoyancy production that is lower in EULAG simulations. With lower strength of maximum updraft the EULAG simulations yield lower amount of surface precipitation. Additional sensitivity study indicates, however, relatively high sensitivity of convection characteristics to horizontal and vertical resolution. Reducing model's grid box size by a factor of 2 leads to about 40% increase in updraft intensity and about 50% and 10% enhancement for maximum amount of cloud and rain water, respectively. It should be underlined that, for this particular case, the improvement is stronger when horizontal resolution is refined rather than vertical one. The spread of the results is larger than for KW78 experiment, especially for water species. This suggests that we are in a flow regime where the problem is strongly underresolved. Thus a comparison between the models is somewhat burdened with possible susceptibility of the results to the details of numerics (see e.g. discussion in Rosa et al., 2011, on cold density current experiment according to Straka et al., 1998).

Detailed comparison of the storm splitting shows that the EULAG's representation of the process is similar to WK82 in terms of horizontal extent of the cells and the relative distance between them during the storm development. In both cases, formation of rear precipitation is observed in similar regions. The area of the cold pool depends directly on the distance between the cores and is larger for more mature supercells. The main difference between the models is that the storm splitting starts at lower shear strength for EULAG simulation and is already observed for $U_s = 15$ m/s, in contrary to $U_s = 25$ m/s for WK82.

Time evolution of maximum updraft velocity for different values of U_s is shown in Fig. 22. A supercell developing in a resting atmosphere ($U_s = 0$) decays quickly in WK82 but it is able to restore secondary circulations in EULAG simulation. Convection is also less vigorous in EULAG simulations since w_{max} reaches about 30 m/s in contrary to about 40 m/s in WK82. This parameter, however, is especially sensitive to the simulation details, as shown through sensitivity experiment for KW78 and WK82. Generally, the spin-up time is shorter in WK82 than in EULAG. The EULAG's spin-up time depends on the resolution in such a way that for smaller grid box sizes the convection starts earlier. The differences are relatively large as the model reaches first maximum of rain water mixing ratio after 38 min for basic resolution and at about 30 min for a doubled one. Such a time shift is also observed for maxima of cloud and rain water mixing ratios.

3.5 Summary and further development

This section documents the results of two moist benchmark experiments (KW78 and WK82) carried out by the EULAG model in order to verify its performance as a potential candidate for the future dynamical core of weather forecasting model. Both experiments concern formation of supercell in a deep atmosphere, which is unstable to moist convective motions. The results of EULAG simulations show that the model is capable to reconstruct main features of the supercell development, such as storm splitting and a cold pool formation. The EULAG solutions are realistic and compare well qualitatively with the reference solutions from KW78 and WK82 for a wide set of initial conditions (i.e., atmosphere at rest, unidirectional shear flow of different strength, veering wind). In general, the EULAG model yields less intense storm development, however, it is difficult to find the factors controling the results. Sensitivity studies indicate that convection-permitting NWP models operating at resolution of $O(1km)$ are in a strongly underresolved regime where relatively small modifications in resolution can significantly change the result (e.g., about 40% enhancement of the updraft strength for doubled vertical resolution). Moreover, the comparison between different numerical models does not allow for credible estimation/separation of the numerical and mathematical effects in the solution.

More recently, a compressible version of the EULAG model has been developed (see e.g., Kurowski et al., 2013). This created a new opportunity to compare the anelastic and compressible solutions using a highly unified numerical framework, and thus to limit the effects associated with different numerical design of the models. Currently, the model has been verified in a set of moist experiments regarding various scales of the atmosphere. First results of these experiments were already published (Kurowski et al., 2013). As for moist deep convection, the results obtained for Weisman and Klemp (1982) experiment have confirmed high consistency of anelastic and compressible solutions. It was also found that non-hydrostatic pressure perturbations are of negligible importance to the storm development. Concomitantly, sensitivity of the solutions to the numerical details (e.g., resolution) and/or physical parameterizations (e.g., subgrid-scale mixing) turned out to be at least one order of magnitude larger than for mathematical differences. Detailed results of these experiments are expected to be published soon.

References

Davies H. C., (1976), A lateral boundary formulation for multi-level prediction models, *Quart. J. R. Met. Soc.*, 102, 405-418.]

Klemp J. B. and R. B. Wilhelmson, (1978), The simulation of three-dimensional convective storm dynamics, *J. Atmos. Sci.*, 35, 1070-1090.

Lipps F. B., and R. S. Hemler, (1982), A scale analysis of deep moist convection and some related numerical calculations, *J. Atmos. Sci.*, 39, 2191-2210.

Kurowski M. J., Grabowski W. W., and P. K. Smolarkiewicz, 2013, Towards multiscale simulation of moist flows with soundproof equations, *J. Atmos. Sci.* (accepted, doi:10.1175/JAS-D-13-024.1)

Kurowski M. J., Rosa B., Ziemianski M., 2011, Testing the anelastic nonhydrostatic model EULAG as a prospective dynamical core of a numerical weather prediction model. Part II - simulations of supercell., *Acta Geophysica*, 59, 1267-1293

Skamarock W. C., J. D. Doyle, P. Clark, and N. Wood, (2004), A standard test set for nonhydrostatic dynamical cores of NWP models, *20th Conference on Weather Analysis and Forecasting/16th Conference on Numerical Weather Prediction, Seattle*

Weisman M. L. and J. B. Klemp, (1982), The dependence of numerically simulated convective storms on vertical wind shear and buoyancy, *Mon. Wea. Rev.*, 110, 504-520.

4 Semi-realistic flow over the Alps with the anelastic EULAG model

Michał Ziemiański, Marcin J. Kurowski, Zbigniew P. Piotrowski, Bogdan Rosa and Oliver Fuhrer

Institute of Meteorology and Water Management - National Research Institute, Poland, and MeteoSwiss, Switzerland

4.1 The experiment setup

The aim of the experiment was to test the EULAG dynamical core over realistic high-mountain orography for its robustness and for general physical viability of the solutions and their consistency for varying but very high horizontal resolutions (grid sizes of 2.2, 1.1 and 0.55 km). For such resolutions, the approximation of quasi-horizontal flows is no longer valid, as the models begin to resolve explicitly convective processes. Also, the model-represented inclinations of high-mountain slopes begin to resemble their actual steep values. In consequence, the dynamical cores for very-high-resolution NWP require reliable and robust solvers, which do not compromise the advantages of very high horizontal resolutions via, e.g., the introduction of a strong artificial smoothing of the orography or the simulated flow. The experiment allows also to investigate how increasing horizontal resolutions influence model-represented flow over high and diversified orographies, for horizontal grid sizes that allow a realistic representation of mountain slopes and heights. The detailed description of the experiment and its results can be found in Ziemiaski et al (2011).

The experiment employs the frictionless and adiabatic flow, which allows direct focus on the dynamical aspects of the flow, influenced only by the model-represented orography, independent of the impacts of the parameterized boundary layer physics or moist processes. An additional argument is that knowledge of mountain boundary layer physics is limited, which also concerns its parameterizations (see e.g., Rotach et al., 2008 and references therein). It was important also to employ relatively simple and easy-to-reproduce initial and boundary conditions. The idea of the experiment follows previous studies, where the numerical simulations of mountain flows were used to study varying spatial resolutions on mountain drag, e.g., Clark and Miller (1991), Hoinka and Clark (1991), Salvador et al., (1999), Rontu (2006) and Smith et al., (2006), or to study the influence of varying numerical schemes on the properties of the simulated flows, as in Cullen et al., (2000).

a. Domain

The experimental setup is based on the operational NWP COSMO model employing horizontal grid length of 2.2 km, used by MeteoSwiss (the COSMO-2 model, see description in Leuenberger et al., 2010). It concerns the experimental domain (see Fig. 23) which for 2.2 km horizontal grid spacing involves 520 by 350 grid points, so that the horizontal size of the domain is 1144 by 770 km, respectively. The locations (geographical coordinates) of the grid points for the experiment are the same as for the grid points of operational COSMO-2. For the experiment involving 1.1 km horizontal grid spacing, the locations of the grid points collocate with the grid points of COSMO-2, where possible, while the locations of the additional points are defined via halving the distances between the COSMO-2 grid points. Similarly, the additional grid points for the simulations with 0.55 km grid spacing are calculated by halving the distances between the grid points used for simulations employing the 1.1 km grid. As a consequence, the simulations at 1.1 km grid size employ a 1040 by 700 grid point
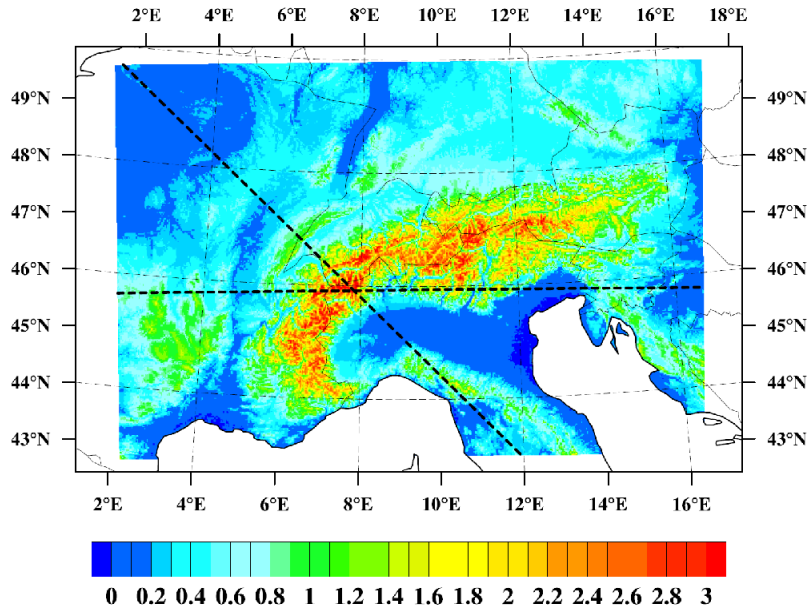
Figure 23: Model orography for 1.1 km grid size (in km, colors), illustrating the orientation of the model domain relative to the main geographic features of the area and political boundaries (thin lines). The thick dashed lines show positions of the cross sections discussed in the paper.

domain, and simulations at 0.55 km grid size employ a 2080 by 1400 grid point domain. The time steps used are 20, 12 and 6 s, for horizontal resolutions of 2.2, 1.1 and 0.55 km, respectively.

The orography for the 2.2 km grid length experiment is the same as the orography employed by COSMO-2. The orography for higher horizontal resolutions was calculated using the satellite SRTM data (Rabus et al., 2003) of approximately 90 m grid size, separate for experiments employing 1.1 and 0.55 km grid length. The satellite data were averaged over the target model grid cells, resulting in a model orography with increasing detail for decreasing grid spacing. No additional smoothing was applied for the data.

In the vertical, the model domain spans from the surface to a height of 23.5 km and employs terrain-following Gal-Chen coordinates (Gal-Chen and Somerville 1975) for the whole vertical extent of the domain using 61 grid levels. The definitions of the grid levels, except the lowest one, are as in the COSMO-2 model, with the vertical grid spacing ranging from about 10 m near the surface to about 500 m in the stratosphere, as is typical for NWP models having relatively high vertical resolution in the near-surface area of the boundary layer. The number and configuration of the vertical grid levels is the same for all the resolutions, employed.

b. The flow configuration

The model employs a free-slip boundary condition on its bottom and top levels, and there are no parameterizations of physical, subgrid-scale processes. The Coriolis force is incorporated into the simulation setup. To avoid the effects of gravity wave reflections from the top of the domain, an absorber was applied above 16 km altitude.

The ambient flow configuration of potential temperature and wind is possibly simple and defined as horizontally uniform. It is imposed by appropriate initial and constant in time boundary conditions. Such a flow configuration is commonly used for idealized simulations
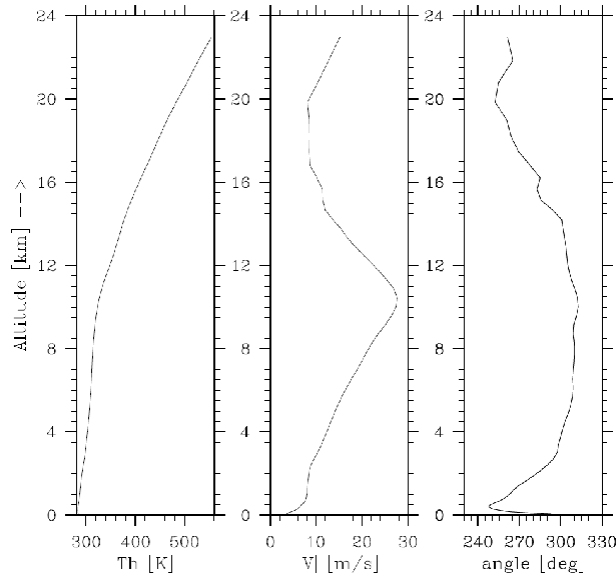
Figure 24: Profiles of the parameters of the ambient flow: potential temperature (left), wind velocity (middle), and wind direction (right).

of deep convective flows (e.g., Klemp and Wilhelmson 1978, Weisman and Klemp 1982, Rotunno and Klemp 1985, Bryan and Fritsch 2002) even though it does not formally preserve the thermal wind balance. It allows for a simple definition of the initial conditions for resolution-dependent configurations of orography.

To ensure that the wind and potential temperature profiles take typical atmospheric values, they are based on an actual meteorological situation in Central Europe on 12 November 2009 at 00.00 UTC. The profiles were calculated as horizontally-averaged wind and potential temperature coming from the operational COSMO-2 analysis of MeteoSwiss. The profiles (Fig. 24) indicate typical moderate north-westerly atmospheric flow of moderate stratification (the Brunt-Väisälä frequency for the lower half of the troposphere equals 0.013 s^{-1}), with a presence of a moderate jet stream characterized by maximum wind reaching 27.6 ms^{-1} at 10450 m above the sea level.

4.2   Results

The aim of the experiment is to analyze and compare the EULAG results for different horizontal resolutions when a quasi-stationary state of the flow is established. The analysis of time-dependent flow diagnostics (not shown) indicates that the flow fields of all simulations have reached a quasi steady-state after 24h of integration time.

a. Surface wind

Figure 25 compares the distribution of the horizontal wind on the second computational level (counting from the Earths surface) of EULAG (located about 10 m above the ground) for the tests using horizontal grids of 2.2, 1.1 and 0.55 km.

For all resolutions used, results have a very high level of consistency and realism. The large-scale flow pattern is practically the same for all resolutions, showing a westerly inflow on the Alpine ridge that divides the flow into two branches around the Alps from north and
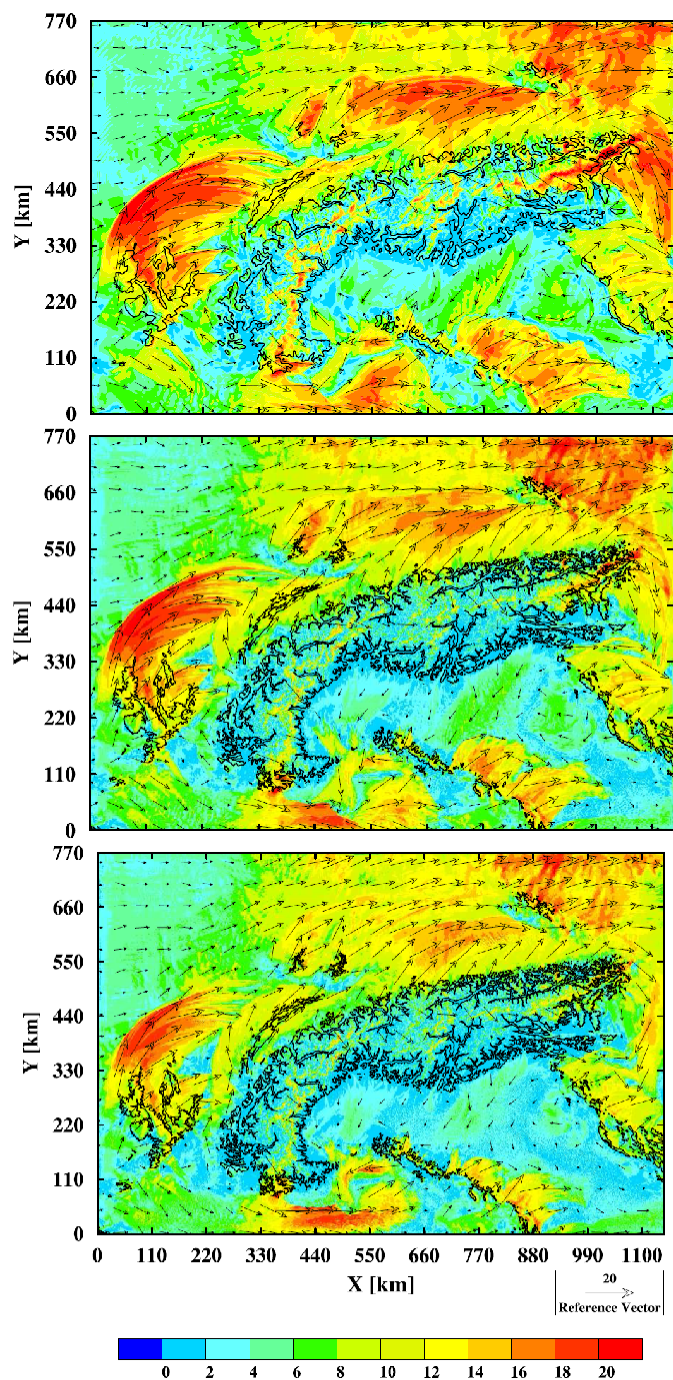
Figure 25: Distribution of the surface (10 m above the ground) wind (arrows) and its speed in m/s (colors) after 24-hours for grid sizes of 2.2 km (upper panel), 1.1 km (middle panel), and 0.55 km (lower panel).

south. The scenario agrees with a blocking condition, characterized by low Froude number (see e.g., Brighton (1978) for laboratory or Smolarkiewicz and Rotunno (1990) for numerical experiments). The Froude number is defined as $F = U/(NH)$, where U is the characteristic horizontal wind velocity, N is the Brunt-Väisälä frequency, and H is the characteristic mountain height. For the characteristic wind speed and stability defined by the ambient temperature profile, it is about 0.2. There is also a signature of an easterly circulation, opposite to the ambient wind, that turns into a southerly flow west of the windward slopes of the western Alps, consistent with the blocking condition. On the lee, southeastern side of the Alps (Po Valley), a weak-to-moderate easterly and northeasterly flow is also present. The Rossby number, assuming a half-width of the Alpine ridge ranging between 100 to 400 km and the wind speed in the lower troposphere in the range of 5 to 10 ms^{-1}, is less than 1 (for average values of the above parameters, its value is 0.3), indicating that Coriolis effects limit the spatial extent and strength of the return upstream circulation (Pierrehumbert and Wyman, 1985), in agreement with the simulation results.

All the experiments show the presence of many mesoscale (size of about 100 km) features of the wind distribution. They show the flow response to the topography and especially to its mesoscale features of sizes and elevations smaller than that of the Alps. Areas of enhanced flow are mainly located over and north-northwest of major terrain obstacles. This effect is particularly evident in the Massif Central, the western Alps and Jura, Vosges, and Schwarzwald. South of the Alps, such areas are located over the Ligurean Sea, south of the Gulf of Genoa, on the lee side of the Appenines, and on the lee side of the Dinaric Alps on the Balkan Peninsula. Areas of pronounced deceleration of the flow are the upper parts of the Saône and Rhine Valleys, and the area west of the Sumava Mountains. South of the Alps, two pronounced areas of relative deceleration are parts of the Gulf of Genoa and of the Adriatic Sea south of the Gulf of Venice.

The prominent difference between the simulations at different horizontal resolutions involves the flow magnitude. While the domain-averaged wind velocity on that level equals 9.09 ms^{-1} for 2.2 km grid size, it is 8.16 and 7.25 ms^{-1} for grid sizes of 1.1 and 0.55 km, respectively. As the simulations do not employ an explicit drag, the results show the influence of terrain-induced form drag of the explicitly represented orography (see e.g., Welch et al., 2001), which increases significantly at higher resolutions. This extends the findings of Clark and Miller (1991) and Smith et al., (2006) to higher resolutions.

Figure 26 shows that the patterns of wind speed differences between the simulations employing different resolutions span a range of scales from the smallest to hundreds of kilometers. The amplitudes of the differences are relatively high and reach -19 to 17 m/s for the difference between 1.1 and 2.2 km grid lengths, -20 to 19 m/s for the difference between 0.55 and 1.1 km grid lengths, and -24 to 17 m/s for the difference between 0.55 and 2.2 km grid lengths. Horizontally, the most extended difference patterns are located over the outskirts of the Alps and form elongated areas aligned with the wind direction (see Figure 3). The narrow streaks of extremum wind speed differences in such structures can be identified with differences in spatial extent of main mesoscale features of wind distribution, discussed above. There are also many features on a scale of about 100 kilometers, where the amplitudes of wind speed differences exceed 10 ms^{-1} and have both signs. They primarily occur in areas between or on the lee sides of main orographic features. Frequently, these flow features are systematic enough to be recognized on all the figures by their similar location and size, and they frequently have the same sign. Therefore, increasing the resolution to grid sizes of 1.1 and 0.55 km tends to have a similar effect on the mesoscale differences of the simulated flow. On the other hand, the differences between simulations with 0.55 and 1.1 km grid lengths tend to be smaller in terms of horizontal sizes and magnitudes. There is also an abundance of very small-scale differences in the wind speed pattern - of an amplitude of a few m/s -
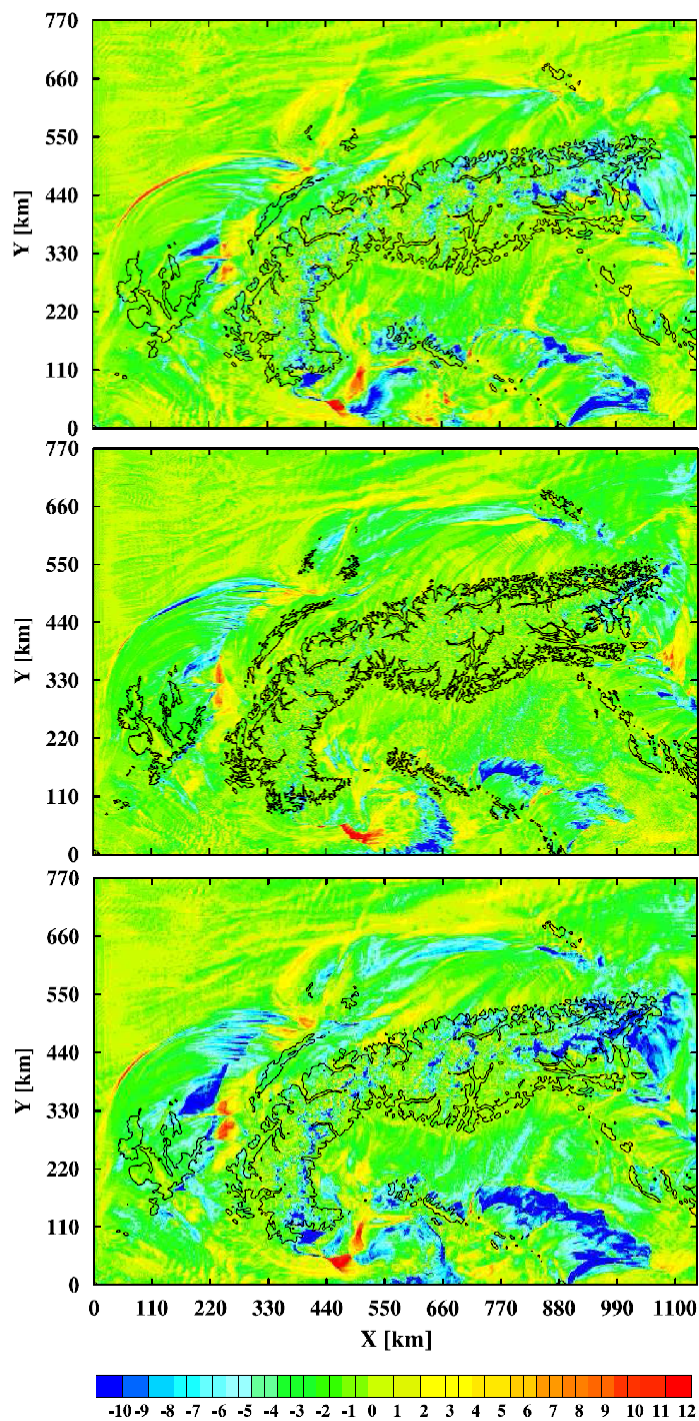
Figure 26: Distribution of the differences for surface (10 m above the ground) wind speeds in m/s (colors) after 24 hours. These difference plots compare the experiment using 1.1 km grid size (averaged to 2.2 km grid box) with the one using 2.2 km grid size (upper panel), the experiment using 0.55 km grid size (averaged to 1.1 km grid box) with the one using 1.1 km grid size (middle panel), and the experiment using 0.55 km grid size (averaged to 2.2 km grid box) with the one using 2.2 km grid size (lower panel).
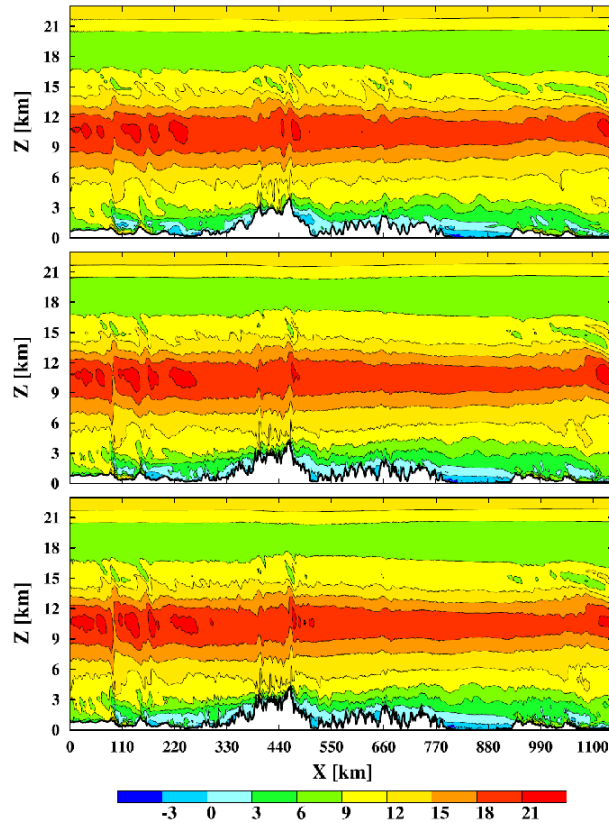
Figure 27: Vertical cross section through the u-component of wind (in ms^{-1}) after 24-hour simulations, for grid sizes of 2.2 km (upper panel), 1.1 km (middle panel), and 0.55 km (lower panel).

both over the relatively flat terrain (including sea surface) and over orographic features.

b. Vertical wind structure

Figure 27 shows west-east vertical cross sections of the u-component of wind velocity, along a line crossing the highest surface elevation represented by the model (Mt. Rosa). The general pattern of the flow is very similar for all the horizontal resolutions in the study. Its main feature is a moderate jet stream, and there are a number of mesoscale flow features over the whole domain. In the jet stream area, the locations and overall shapes of the mesoscale features are similar for all the simulations, which include e.g., pronounced acceleration areas above and in the lee of the Massif Central (left), over the Mt. Rosa area, and in the lee of the Dinaric Alps (right). Small-scale details differ between the simulations: very sharp horizontal wind gradients above the Massif Central and the Cevennes are especially pronounced, and they are reproduced with more detail and sharper gradients as the resolution increases.

The flow variability is closely related to mountain wave activity, which is abundant in the whole model domain and occurs on scales of about 50 km and smaller. All the simulations show similar flow features on the horizontal scales between 20 and 50 km (e.g., the structures over the Massif Central and the Cevennes, or over the Dinaric Alps). But there are also many smaller-scale features that differ significantly between the simulations.

Figures 28 shows the u-components of wind for a magnified part of the domain shown in Figure 27 located in the vicinity of the highest Alpine peaks (the x-coordinate is the same for
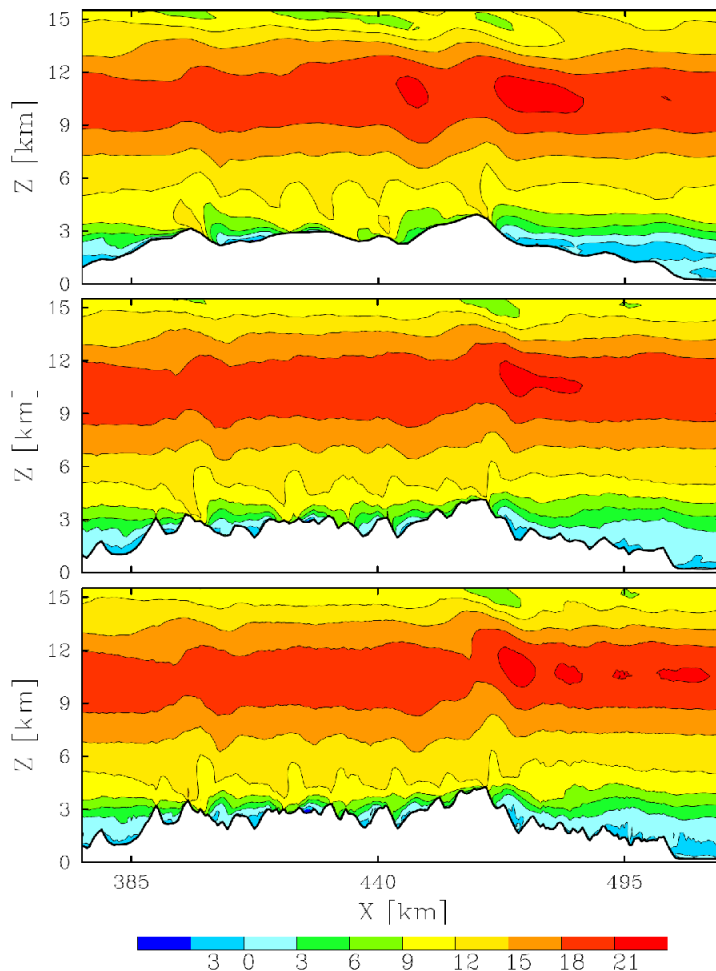
Figure 28: Closer view of the wind u-component (in m/s) over the highest Alpine peaks shown in Fig. 27 for a more detailed comparison as model resolution increases. Upper panel shows model output at 2.2 km grid size, middle shows 1.1 km grid size, and lower shows 0.55 km grid size.

all three figures). It confirms that the overall flow pattern is similar for all three resolutions. The differences are especially evident in many small-scale details of about 1 to 20 km in horizontal size for the u-component of the wind. They are seen in the jet stream area, particularly in the spatial structure of the maximum wind pattern. The largest differences appear, as expected, in the near-surface flows. Some of the differences represent circulations related to valleys, peaks, or ridges, represented only with very-high-resolution orography.

Qualitatively similar results are found for the v-component of the horizontal velocity (not shown).

Table 5 compares the RMS wind speed differences between simulations of different horizontal resolutions. It uses the 0.55 km simulation as the reference and compares data interpolated to a fixed height above ground (or above mean sea level). The comparison is done using grid point values and only grid points present in coarser resolution are used. To focus on the mountain regions, the comparison concerns areas of surface elevations exceeding 800 m above the mean sea level, for orography employing 0.55 km horizontal grid length. The table shows the wind differences on a few near-surface levels (at 20, 100, 500 and 2000 m above the ground) and on a few levels representing middle and upper troposphere (5, 6, 7 and 10 km

Altitude (m) above surface	RMS wind speed difference (m/s) between models of grid sizes (km):	
	0.55-2.2	0.55-1.1
20	3.92	1.83
100	3.80	1.64
500	2.87	1.10
2000	1.65	0.72
Altitude (m) above mean sea level	RMS wind speed difference (m/s) between models of grid sizes (km):	
	0.55-2.2	0.55-1.1
5 000	1.12	0.39
6 000	0.73	0.28
7 000	0.57	0.28
10 000	0.91	0.32

Table 5: RMS wind speed difference between simulations with 0.55 and 2.2 km grid sizes and between simulations with 0.55 and 1.1 km grid sizes, at selected altitudes above the surface and above mean sea levels. The differences are calculated only over the areas of surface elevation exceeding 800 m above mean sea level.

above the mean sea level). The table demonstrates larger differences between experiments with 0.55 km and 2.2 km grid sizes as compared to the differences between the experiments with 0.55 km and 1.1 km grid sizes. The largest differences between the experiments are located just above the surface, with values reaching almost 4 m/s for comparison between experiments with 0.55 and 2.2 km grid sizes. The differences diminish rapidly above 100 m height. The differences still decrease with height in the middle troposphere, but tend to increase near the tropopause.

c. Potential temperature

The general pattern of the potential temperature field is very similar for all three resolutions, and only small-scale details differ between the simulations (not shown). The differences are largest in the near-surface layer. They are due to both the ambient relation between the temperature and height, and the differences in the orographically induced flows. Also, the undulations of the isentropes in the near-surface layer of about 2 km depth above the Alpine ridge tend to have larger amplitudes for higher-resolution simulations. The differences between the simulations are hardly noticeable in the middle and upper troposphere.

Table 6, calculated analogously to Table 5, shows the RMS differences in the potential temperature between the simulations using interpolated values at the selected height levels. The table shows that the differences between simulations with 0.55 km and 2.2 km grid lengths are larger than the differences between experiments with 0.55 km and 1.1 km grid lengths. The largest differences are located in the near surface layer, and are in the range of 1 and 0.6 K for comparison with 2.2 km and 1.1 km grid simulations, respectively. In the middle troposphere the differences reach about one third of the surface values and increase in the tropopause area.

Altitude (m) above surface	RMS potential temperature difference (K) between models of grid sizes (km):	
	0.55-2.2	0.55-1.1
20	0.97	0.56
100	0.83	0.47
500	0.71	0.36
2000	0.52	0.25
Altitude (m) above mean sea level	RMS potential temperature difference (K) between models of grid sizes (km):	
	0.55-2.2	0.55-1.1
5 000	0.37	0.18
6 000	0.37	0.17
7 000	0.22	0.09
10 000	0.33	0.15

Table 6: RMS potential temperature difference between simulations with 0.55 and 2.2 km grid sizes and between simulations with 0.55 and 1.1 km grid sizes at selected altitudes above the surface and above mean sea levels. The differences are calculated only over the areas of surface elevation exceeding 800 m above mean sea level.

d. Vertical velocity

Figure 29 shows the horizontal distribution of the vertical velocity at level 40, located in the free atmosphere at a height of about 10400 m for all simulations. While the general pattern of the main features of the vertical velocity distribution is basically similar for all three resolutions, and while the regions of gravity wave activity do not change, significant small-scale differences are also present. In all simulations, it is common for the main patterns of the vertical velocity to be located in the vicinity of orographic features with the wave crests typically oriented perpendicular to the mean flow direction. This description generally applies to the Massif Central and the Cevennes, the Vosges Mountains and Schwarzwald, and the Sumava Mountains and the Alps. The amplitudes of the vertical velocity are in the range of 0.5 m/s, which is a realistic value.

For the area above the Alps, the pattern of the vertical velocity structure is generally similar for all the simulations in the sense that the main activity is located over the eastern slopes of the southwestern Alps and over the central crests of the eastern Alps. There are, however, clear differences. As the horizontal grid size of the model diminishes, the wave activity over the main Alpine body seems less pronounced as its spatial extent is also smaller and the wave amplitudes tend to be smaller in the area. In contrast, the wave activity over the areas south of the southwestern (Maritime) Alps and southeast of the eastern Alps seems to be at least as vigorous as for the coarser resolution simulation, but with a more complicated wave structure and many additional small-scale details.

Figure 30 presents vertical cross sections of vertical velocity, crossing the highest surface elevation of the model (Mt. Rosa), along the wind direction in the middle and upper troposphere and spanning the full model domain (see Figure 23 for the exact location of the cross-section). It shows similarity of the high-amplitude component of the wave distribution
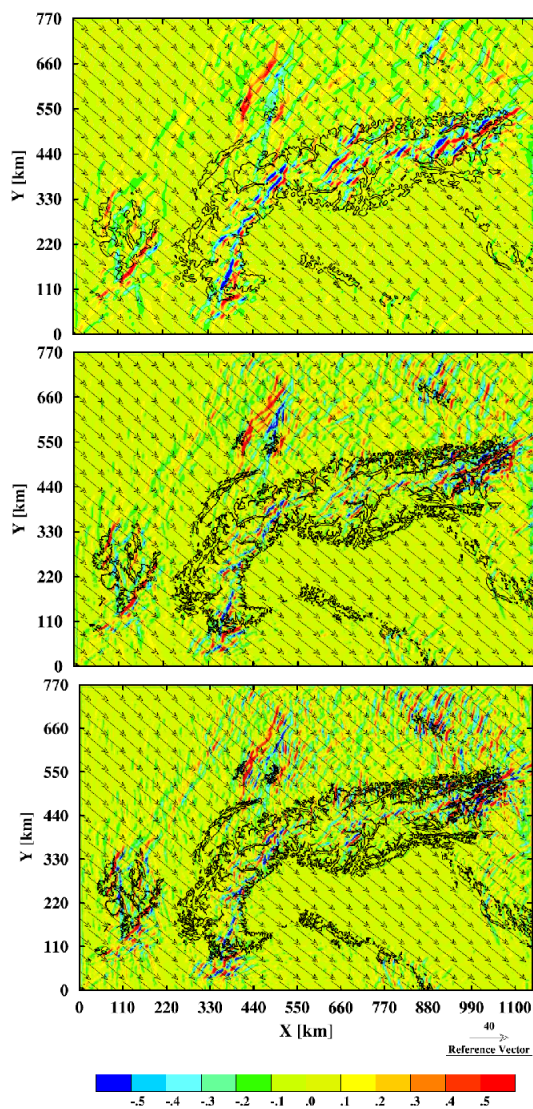
Figure 29: Horizontal distribution of wind (arrows) and the vertical velocity in ms^{-1} (colors) at 10400 m height after 24-hour simulations for grid sizes of 2.2 km (upper panel), 1.1 km (middle panel), and 0.55 km (lower panel).
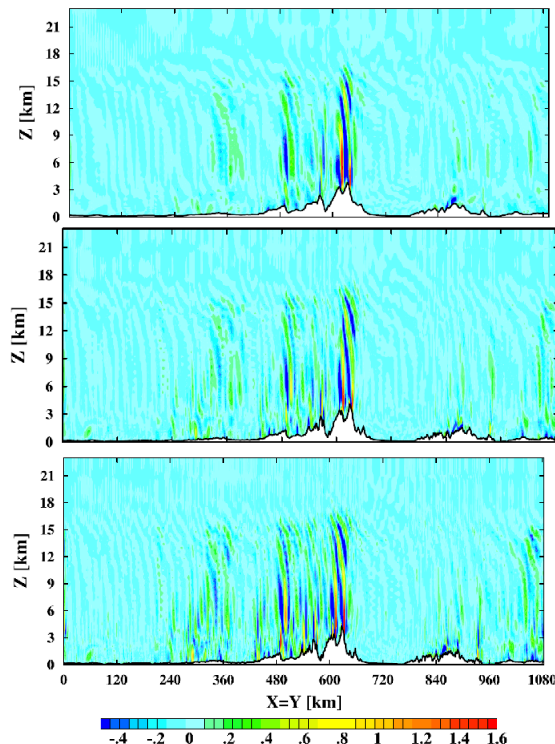
Figure 30: Vertical velocity distribution (colors in m/s) after 24 hours for simulations with grid sizes of 2.2 km (upper panel), 1.1 km (middle panel), and 0.55 km (lower panel). The cross section is oriented along the prevailing wind in the middle and upper atmosphere.

for different resolutions, but it confirms also the significant influence of horizontal model resolution on the simulated structure of vertical velocity. The differences appear in both the relatively low highlands, like the Plateau de Langres, where the 2.2 km grid shows the presence of only a single wave pattern in the middle and upper troposphere. In contrast, the higher resolution simulations show rich wave structures of slightly larger amplitudes in the middle troposphere and significantly higher amplitudes near the surface. The differences are also clearly seen above the higher mountains, especially in the area between the Jura and Mt. Rosa, where the higher-resolution simulations have significantly richer wave structures characterized by larger amplitudes.

Figure 30 shows a detail of Figure 29 over the Alps. The significant influence of the horizontal model resolution on the vertical velocity distribution is seen by the presence of the complicated wave pattern in the area west of the Rhone Valley (left), obtained with the highest-resolution simulation. For the common features, the 0.55 km grid size gives significantly higher amplitudes and more realistic wave structures for the wave triggered by the Jura (the western part of the figure) and the eastern parts of the Bernese Alps. The wave pattern and magnitudes of extremes triggered by the Pennine Alps, including Mt. Rosa, are similar at all three resolutions. However, the higher-resolution simulations show many small-scale details of the structure, especially in the near-surface layer, where small-scale terrain features play an important role in forming the shape of the wave pattern. For the area roughly 2 km above the surface, the influence of the larger scales prevails and the differences between the simulations become smaller.

The realism of the simulations can be further confirmed by noticing that the wave crests tend to change to a horizontal orientation in the upper part of the domain. This is a typical
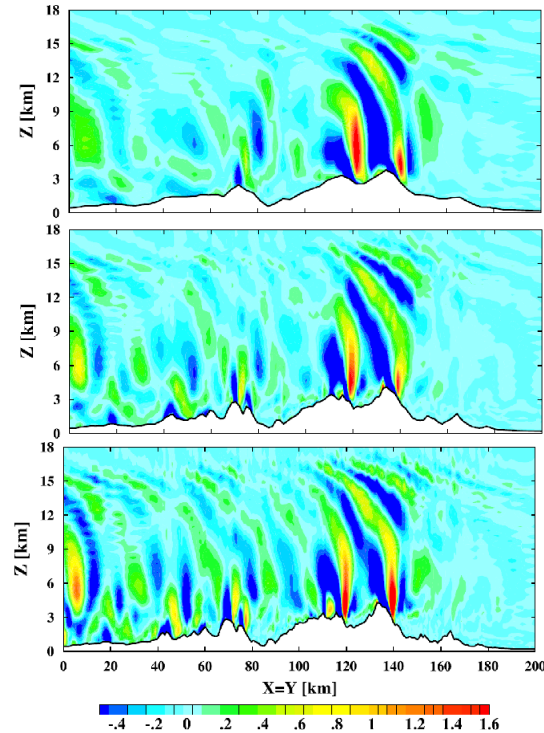
Figure 31: Enlarged picture of the flow over the Alps.

behavior for a gravity wave in the presence of the critical layer, where the phase velocity of the wave equals the flow velocity. For the Brunt-Väisälä frequency on the order of 0.013 s^{-1}, and the wavelength in the horizontal and vertical directions on the order of 10 km, estimates place the critical velocity in the range of 20 m/s which corresponds well to the typical wind speeds found in the upper troposphere. This suggests the presence of the critical layer in our simulations and confirms the physical consistency of the simulated gravity waves.

Table 7 shows the RMS differences of the vertical velocity between the simulations at selected levels, for the areas with surface elevations above 800 m and not averaged to the coarser grid. It shows that the differences between experiments with 0.55 km and 2.2 km grid lengths are larger than the differences between simulations with 0.55 km and 1.1 km grid lengths. While the differences between analyses of velocities and potential temperature presented in Figure 30 and Tables 5 and 6 are relatively small, they are larger for the vertical wind. Table 7 shows that the vertical velocity differences between the solutions over higher elevations are almost three times larger than average. This is confirmed by a qualitative analysis of Figures 29 to 30, suggesting that vertical velocity perturbations are spatially related to the areas of highest elevations, and that the horizontal resolutions significantly affect the vertical velocity pattern. Over the mountains, the RMS differences are highest in the near-surface layer, reaching almost 0.9 m/s for the comparison between the experiments with 0.55 and 2.2 km grid lengths. They decrease with height by about one third at 2000 m altitude. In the middle and upper troposphere the difference still diminishes with height, consistent with Figure 30a.

4.3 Summary and conclusions

The tests show the numerical robustness of the EULAG dynamical core, as no numerical problems were encountered during the simulations and no artificial measures, like flow or

Altitude (m) above surface	RMS vertical velocity difference (m/s) between models of grid sizes (km):	
	0.55-2.2	0.55-1.1
20	0.87	0.54
100	0.80	0.47
500	0.69	0.38
2000	0.59	0.35
Altitude (m) above mean sea level	RMS vertical velocity difference (m/s) between models of grid sizes (km):	
	0.55-2.2	0.55-1.1
5 000	0.49	0.29
6 000	0.42	0.24
7 000	0.33	0.28
10 000	0.20	0.11

Table 7: RMS of vertical velocity difference between simulations with 0.55 and 2.2 km grid sizes and between simulations with 0.55 and 1.1 km grid sizes, over areas of elevation exceeding 800 m above mean sea level, at selected altitudes.

orography smoothing, were applied to achieve the results. The scales of the values of the flows physical parameters are represented correctly. This concerns especially vertical velocity, magnitude of which is sensitive to possible problems in the model setups. This suggests that an anelastic dynamical core like EULAG has numerical robustness appropriate for NWP purposes at horizontal grid sizes of at least $O(1km)$.

The analysis of the results, especially of the spatial distribution of different parameters characterizing the flow and their comparison for varying horizontal resolutions, shows that the results are realistic and highly consistent. Results indicate a realistic low-level flow pattern characteristic of mountain blocking, and the presence of characteristic mesoscale features related to the flow over specific terrain features like large valleys, highlands, and mountains. The vertical flow structure shows that the orography significantly influences regional and local circulations, including low-level circulations like valley flows, but especially mountain waves, and the whole troposphere including the structure of the jet stream.

The flow structures are consistent between the three model resolutions, especially for flow features having characteristic sizes of 20 km and more. However, the differences between simulations involve a wide range of scales and are not limited solely to the barely resolved scales. The differences are seen especially clearly and abundantly in the near-surface tropospheric layer at a depth of about 1.5 to 3 km. For surface wind, differences between the three solutions have characteristic structures of horizontal sizes varying from hundreds of kilometers to the smallest resolved by the model, the amplitudes of the differences reach up to 20 m/s, and the RMS difference reaches 4 m/s. From the viewpoint of NWP, the near-surface area is highly important for a majority of the forecast users, including aviation.

References

Brighton, P.W.M. (1978), Strongly stratified flow past three-dimensional obstacles, *Q. J. Roy. Meteorol. Soc.* 104, 289-307.

Bryan, G. H., and J. M. Fritsch (2002), A benchmark simulation for moist nonhydrostatic numerical models, *Month. Wea. Rev.*, 1030, 2917-2928.

Clark, T.C., and M. Miller (1991), Pressure drag and momentum fluxes due to the Alps. II: Representation in large scale atmospheric models, *Quart. J. Roy. Meteor. Soc.* 117, 527-552.

Cullen, M., D. Salmond, and P.K. Smolarkiewicz (2000), Key numerical issues for the future development of the ECMWF model, *Proc. ECMWF Workshop on Developments in Numerical Methods for Very High Resolution Global Models*, Reading, ECMWF, pp. 183-206

Gal-Chen T., and R.C.J. Somerville (1975), On the use of a coordinate transformation for the solution of the Navier-Stokes equations, *J. Comput. Phys.* 17, 209-228.

Hoinka, K.P., and T.C. Clark (1991), Pressure drag and momentum fluxes due to the Alps. I: Comparison between numerical simulations and observations, *Quart. J. Roy. Meteor. Soc.* 117, 495-525.

Klemp, J. B., and R. B. Wilhelmson (1978), The simulation of three-dimensional convective storm dynamics, *J. Atmos. Sci.* 35, 1070-1096.

Leuenberger, D., M. Koller, O. Fuhrer, and C. Schaer (2010), A generalization of the SLEVE vertical coordinate, *Month. Wea. Rev.*, 138, 3683-3689.

Rabus, B., M. Eineder, A. Roth, and R. Bamler (2003), The shuttle radar topography mission (SRTM) - A new class of digital elevation models acquired by space borne radar, *ISPRS J. Photogramm. Remote Sens.* 57, 241-262.

Rontu, L. (2006), A study on parametrization of orography-related momentum fluxes in a synoptic-scale NWP model, *Tellus A* 58, 69-81.

Rotach, M.W., M. Andretta, P. Calanca, A.P. Weigl, and A. Weiss (2008), Boundary layer characteristics and turbulent exchange mechanisms in highly complex terrain, *Acta Geophysica* 56, 194-219.

Rotunno, R., and J.B. Klemp (1985), On the rotation and propagation of simulated supercell thunderstorms, *J. Atmos. Sci.* 42, 271-292.

Salvador, R., J. Calbo, and M.M. Millan (1999), Horizontal grid size selection and its influence on mesoscale model simulations, *J. Appl.Meteorol.* 38, 1311-1329.

Smith, S.A., J.D. Doyle, A.R. Brown, and S. Webster (2006), Sensitivity of resolved mountain drag to model resolution for MAP case-studies, *Quart. J. Roy. Meteor. Soc.* 132, 1467-1487.

Smolarkiewicz, P. K., and R. Rotunno (1990), Low Froude number flow past three-dimensional obstacles. Part II: Upwind flow reversal zone, *J. Atmos. Sci.* 47, 1498-1511.

Weisman, M. L., and J. B. Klemp (1982), The dependence of numerically simulated convective storms on vertical wind shear and buoyancy, *Monthly Weath. Rev.* 110, 504-520.

Welch, T.W., P.K. Smolarkiewicz, R. Rotunno, and B.A. Boville (2001), The large scale effects of flow over periodic mesoscale topography, *J. Atmos. Sci.* 58, 1477-1492.

Ziemianski, M.Z., M.J. Kurowski, Z.P. Piotrowski, B. Rosa, and O. Fuhrer (2011), Toward very high horizontal resolution NWP over the Alps: Influence of in-creasing model reso-lution on the flow pattern, *Acta Geophys.* 59, 6, DOI:10.2478/s11600-011-0054-9.

5   Semi-realistic flow over the Alps with the COSMO-EULAG model

Michał Ziemiański, Marcin J. Kurowski, Zbigniew P. Piotrowski, Bogdan Rosa, Damian Wójcik

Institute of Meteorology and Water Management - National Research Institute, Poland

5.1   Introduction

This section reports on semi-realistic simulations of weather for the Alpine region using a prototype COSMO model equipped with the anelastic dynamical core. The prototype couples the dynamical core of the EULAG model with a limited set of standard COSMO parameterizations. The report begins with a brief description of the implementation of the EULAG dynamic core into the operational software environment of the COSMO model. Next, it shows the results of testing the COSMO-EULAG prototype (CE) for a simulation of mesoscale weather for 24 hours forecast at three different horizontal resolutions i.e. with 2.2, 1.1 and 0.55 km horizontal grid size. The CE results for 2.2 km grid are compared with analogous results obtained using the COSMO model employing standard Runge-Kutta dynamical core and the same limited set of physical parameterizations (RK) to evaluate the viability, consistency and correctness of the CE results. The goal of the comparison is to assess whether the anelasticity of the CE dynamical core has noticeable detrimental effect on the simulation results. Also, the CE results for various resolutions are inter-compared and analyzed to assess whether they are consistent, realistic and robust.

Both model setups involve physical parameterizations of boundary layer effects with surface fluxes, radiation and moist processes. The experiment employs also realistic initial and changing in time boundary conditions for a selected actual weather situation, provided by MeteoSwiss and taken from its operational data. The experiment has, therefore, a higher degree of realism comparing with the one described in the previous section, but the model prototype is still not in a full and consistent NWP setup.

5.2   The COSMO-EULAG prototype

The implementation of the EULAG dynamical core into the COSMO operational environment required addressing a number of technical issues. First, the EULAG dynamical core has been translated from Fortran 77 to Fortran 90/95 which allowed the implementation of alternative programming structures required by the COSMO programming standards. Common blocks were replaced by modules, and the data structure in the translated code is based on explicit dynamic memory allocation. The MPI communication of the CE model was organized in a consistent way with COSMO framework. The key steps of the implementation and the relevant technical details regarding translation have been reported by Wojcik et al. (2012).

The coupling of the two codes (COSMO and EULAG) required a development of specially designed interface. Its main purpose was to allow a data communication between dynamical core and physical parameterizations applying different types of computational grids. The nodal points of the EULAG grids are non-staggered (A-grid) whereas algorithms of COSMO parameterizations have been developed for the staggered C-grid.

The interface is designed according to the rule that the COSMO mass levels and mass
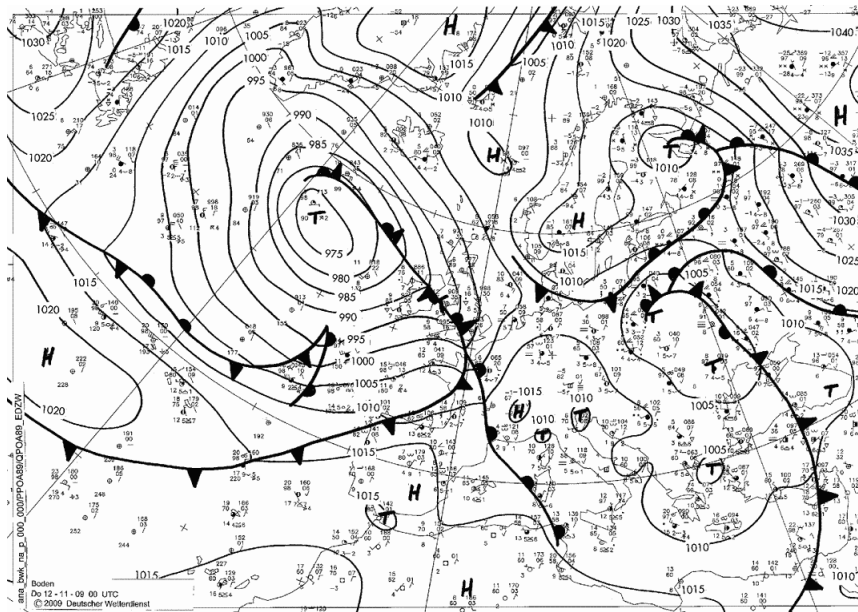
Figure 32: Surface synoptic chart of Europe for 12 November 2009, 00:00 UTC.

points collocate with the EULAG computational points and levels in order to avoid spatial interpolation of the mass-related flow parameters. In order to provide the bottom boundary conditions for the vertical component of velocity (w), an additional EULAG level is provided just at the ground. Its physical flow parameters are the same as the parameters on the next EULAG level collocated with the first COSMO mass level (counting from the surface) in order to ensure consistent values of the flow parameters from the finite-volume-wise view point (alteration of the physical parameters within the surface level would result in alteration of volume averaged values in the COSMO finite volumes around its lowest-lying mass points).

With such an approach, the interface requires interpolation of velocity values between grid A and C while providing information from the dynamical core to the parameterizations, and interpolation of their forcings, diagnosed by COSMO parameterizations, between grid C and A. It transforms also potential temperature of EULAG to temperature of COSMO, as well as temperature forcing from COSMO parameterizations to potential temperature forcing to be used by the dynamical core.

5.3   The experiment setup

The tests are based on 24-hour simulation of an Alpine flow using the COSMO model with the RK and CE setups, both using the same limited set of physical parameterizations. The employed parameterizations are:

- Vertical Turbulent Diffusion

- Surface Fluxes Louis (1979)

- Radiative Transfer Scheme Ritter, Geleyn (1992)

- Multilayer Soil Model

- Moist Microphysics with prognostic variables including rain, snow, ice and graupel.

n/s] after 12h at level = 1   **| [m/s] after 24h at level = 1**

Figure 33: Wind velocity (color scale and wind arrow length) and direction (wind arrow direction) on the 10 m model level for 12 hour (left panels) and 24 hour (right panel) forecast for the CE (upper panels) and RK (lower panels) model versions.

There was no special tuning of the physical parameterizations for the CE setup and their parameters took values tuned for the operational COSMO model using the RK dynamical core.

a. Domain

Similarly to the semi-realistic tests described in the previous section, the experiment setup is based on the COSMO-2 model of MeteoSwiss. Its domain (see Fig. 23 of the previous section), orography, vertical Gal-Chen coordinates and computational layers are configured as for the experiment described in the previous section. Only the size of the computational domain for the experiment employing 0.55 km resolution was limited and covers only a part of the full COSMO-2 domain (see Fig. 41) due to computational reasons.

b. The flow configuration

The experiment follows the actual operational COSMO forecast for 12 November 2009 and involves a 24-hour simulation starting at 00:00 UTC. The initial conditions are the same for RK and CE runs and are taken from operational data of MeteoSwiss. It concerns also the boundary conditions, which are interpolated linearly in time from the hourly data sets.

The synoptic situation, chosen, involves a moderately stratified westerly flow with a moderate

ı/s] after 12h at level = 10   [m/s] after 24h at level = 10

Figure 34: As in Figure 33 but for the 10th model level (approximately 500 m above the ground level).

jest stream. It features a relatively shallow low-pressure system with atmospheric fronts traversing the simulation domain (Fig. 32).

5.4 Results

An analysis of the simulation results is presented below. It compares the wind velocity distribution, cloud water and cumulative surface precipitation for the RK and CE models. Both models use 2.2 km grid size and their results are compared for 12 and 24 hour forecast. Also, the CE results after 12 and 24-hour forecasts are inter-compared for varying resolutions of 2.2, 1.1 and 0.55 km and analyzed.

RK and CE comparison

Figure 33 presents the wind velocity at 10 m above the ground (the first COSMO computational level) for 12 and 24 hour forecast for the CE (upper panels) and RK (lower panels) versions of the model. For both realizations, the general pattern of the flow is practically the same and follows the synoptic situation with weak to moderate south-westerly flow in the western part of the domain and relatively weak variable flow in the rest of the domain which is influenced by the anticyclonic pressure system. Moreover, both simulations very similarly represent the mesoscale structure of the flow with the same patterns of flow acceleration and deceleration(see for instance the pronounced flow patters over the Genoa Bay and Adriatic

Figure 35: As in Figure 33 but for the 26th model level (approximately 4600 m above the ground level).

Sea). Also the wind velocities are very similar for both model versions, with a tendency of the CE solution for slightly higher wind speeds. The effect is especially seen over the Alps. That may result from the lack of tuning of the parameterizations for the CE setup (note the diminishing surface wind velocities of the CE simulations for increasing resolutions, described below). The pattern of the flow areas with nearly zero wind velocities suggests also more patchy (spatially variable) structure of the CE velocity field within the smallest resolvable scales.

Figures 34, 35 and 36 present, respectively, the wind velocity on different computational model levels ranging from level 10 (approximately 500m above the ground), to 26 (approximately 4600 m above the ground) and 40 (approximately 10 km above the ground). Note that the levels are counted from the ground level up (that is opposite to standard COSMO level counting) and the approximate heights of the computational levels concern areas where the ground surface is located at the mean sea level. The results are for 12 (left panels) and 24 hour (right panels) forecast for the CE (upper panels) and RK (lower panels) versions of the model.

The figures show that both the synoptic and mesoscale patterns of the flow as well as wind velocities are to very high degree the same for both simulations and the similarity is even greater, comparing with the surface wind field, for the flow less or not affected by the friction. Only some differences are noticeable for wind velocities. For 10 and 26 model levels (lower and middle troposphere) CE gives slightly higher wind velocities in constrained, localized

[m/s] after 12h at level = 40

[m/s] after 24h at level = 40

Figure 36: As in Figure 33 but for the 40th model level (approximately 10 km above the ground level).

areas, especially immediately north of the Alpine ridge (see the 12 hour forecast at 10 level and 24 hour forecast at 26 level). For level 40 (near the tropopause) the situation is different: the CE solution brings slightly lower wind velocity at areas just over the Alpine ridge (for 12 and 24 hour forecast) and on the lee side of the Alps (for 24 hour forecast). That suggests generally stronger effects of the explicitly resolved orographically induced gravity wave drag in the CE representation of the flow.

Figure 37 presents the vertical cross section through the fragment of wind velocity field in the vicinity of Mt. Rosa. The orientation of the section line is from north-west to south-east (similar to Figure 27 of the previous section), for 12 hour (left panels) and 24 hour (right panel) forecast for the CE (upper panels) and RK (lower panels) model versions. The figure shows clear similarity of the general pattern of the flow but also some differences. The differences are located in the near surface layer where numerous differing very-small-scale details are superimposed within the same large-scale flow pattern. The localized differences are also present in the middle troposphere and have generally a signature of gravity wave structures. For the jet stream area larger-scale differences are seen especially over the mountains (12 hour forecast) and over their lee side (24 hour forecast) where CE wind velocities are smaller suggesting stronger gravity wave drag, in agreement with analysis of Fig. 36.

Figure 38 presents the vertical cross section through vertical velocity distribution in the vicinity of Mt. Rosa, in the area shown by Fig. 37. Also for the vertical velocity distribution the general pattern of the flow is similar for both realizations and for both instances.

Figure 37: Vertical cross section through wind velocity in the vicinity of Mt. Rosa, the north-west to south-east orientation of the section line for 12 hour (left panels) and 24 hour (right panel) forecast for the CE (upper panels) and RK (lower panels) model versions

It concerns especially the magnitudes of the amplitudes and general pattern of the most pronounced features. There are also noticeable differences between CE and RE simulations, which concern details of shape and extension as well as magnitudes of weaker flow features, but they are generally common for both representations.

Figure 38: Like in Figure 37 but for vertical cross section through vertical velocity field

The experiment involved also a simulation of moist processes. The results for CE and RK realizations are very similar. It is seen e.g. analyzing a 3-dimensional distribution of iso-surfaces of constant cloud condensate mixing ratio for which there are no significant differences between the realizations (not shown). A comparison of distribution of cloud water

mixing ratio is shown in Figure 39 presenting a vertical cross section through the field along the north to south oriented cutting line crossing the Western Alps for 6, 12 and 24 hour forecast. The figure demonstrates very similar cloud pattern for CE and RK simulations, especially for relatively dense cloud structures, with some differences concerning smaller scale details and the parameter's amplitudes. For less dense clouds the differences are more significant and in places concern also more general cloud patter. Nevertheless, the similarity of the solutions is significant.

Figure 39: Vertical cross section through the cloud water mixing ratio along the north to south oriented cutting line crossing the Western Alps for 6 (upper panel), 12 (middle panel) and 24 hour forecast; RK results on the left panel, CE on the right.

A good general indication of the consistency of simulations involving representation of moist processes comes from analysis of the resulting precipitation distribution. Figure 40 shows the precipitation accumulated within 12 (left panel) and 24 hours (right panel) periods. The figure confirms a very high degree of similarity of the precipitation pattern for the RK and CE realizations, for both instants. Also the precipitation amounts are similar, especially during the first 12 hours of forecast. Later, for the 24 hour accumulation of precipitation, the locations of maxima are still very similar for both model versions but CE tends to generally produce higher precipitation maxima.

Overall, the consistency of the RK and CE results involving the parameterizations tuned for the RK operational setup and simply implemented to the CE setup can be regarded as significant

CE inter-comparison for increasing horizontal resolution

`kg/m^2] till hour 12h at level = 2`   c. [kg/m^2] till hour 24h at level = 2
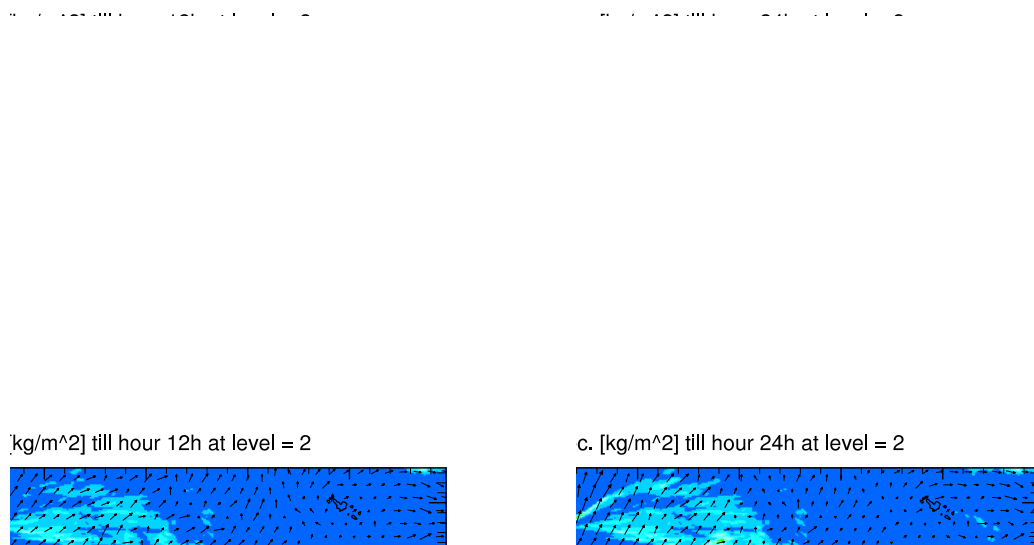

Figure 40: Accumulated precipitation (color scale) and direction on the surface for 12 hour (left panels) and 24 hour (right panel) forecast for the CE (upper panels) and RK (lower panels) model versions.

Figure 41 presents an inter-comparison of surface wind (on the computational level 10m above the surface) obtained with the CE model for 2.2, 1.1 and 0.55 km horizontal grid size. The figures show consistently the same synoptic and mesoscale velocity pattern, discussed above, for all the resolutions. The differences concern mainly small scale details of the flow field and a general tendency for lower wind velocities for increasing horizontal resolution of the simulation, especially over the Alps, suggesting an influence of explicitly resolved orography drag, increasing with increasing model and orography resolutions.

Similarly, Figure 42 compares the wind on 10-th computational level (about 500 m above the surface) for the CE forecast with 2.2, 1.1 and 0.55 km horizontal grid size. The figures show very high consistency of the flow pattern, for all the resolutions. The differences concern mainly small-scale details of the flow field, especially in the immediate vicinity of high mountains. A general tendency for lower wind velocities for higher horizontal resolution is also seen over the Alps, especially while comparing the results for 2.2 and 0.55 km grid size.

Figure 43 (left panels) compares the vertical cross sections through a fragment of the wind velocity field obtained with horizontal grid sizes of 2.2, 1.1 and 0.55 km for the Mt. Rosa vicinity in location close to the one in Fig. 37. The figure allows analyzing in more details the differences in the forecasted velocity field as well as in the orography pattern for different resolutions. It shows that while the results keep consistency of the general flow pattern,
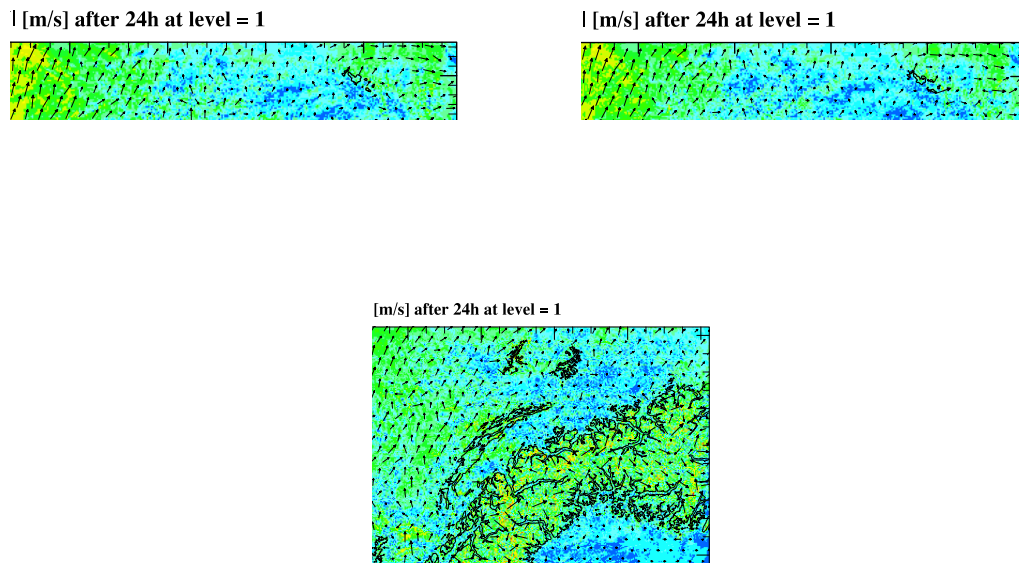
Figure 41: Wind velocity (color scale and wind arrow length) and direction (wind arrow direction) on the 10m model level for 24 hour forecast with the CE model version using horizontal grid size of 2.2 km (left, upper panel), 1.1 km (right panel) and 0.55 km (left lower panel).

the differences concern whole depth of the troposphere and are pronounced especially in the near-surface and the jet stream area. For increasing resolution, in the near-surface area there is more variability in the flow for the smallest scales, which results both from the increased variability of the resolved orographic forcing and of the model resolved scales. In the jet stream area, the differences concern mainly mesoscale patterns of the sizes of tens of kilometers. The general tendency is diminishing strength of the jet stream with increasing resolution, suggesting an increasing drag of explicitly resolved mountain waves. There is no grid-convergence of the simulated flow due to the resolution dependent orography pattern.

Figure 43 (right panels) compares also the vertical cross sections through the CE vertical velocity field obtained with grid sizes of 2.2, 1.1 and 0.55 km for the Mt. Rosa vicinity in the location shown in Figure 42. The wave features forecasted with the 2.2 km resolution and especially the most pronounced wave patterns are also clearly present in simulations with higher resolutions. The features have also similar amplitudes. On the other hand, the simulations with higher resolutions show a presence of increasingly complicated wave patterns with additional or significantly amplified features comparing with 2.2 km grid simulations. Such features are present not only in the vicinity of the surface but also in the middle and upper troposphere and in places reach magnitudes of the main wave features obtained with

[m/s] after 24h at level = 10

[m/s] after 24h at level = 10
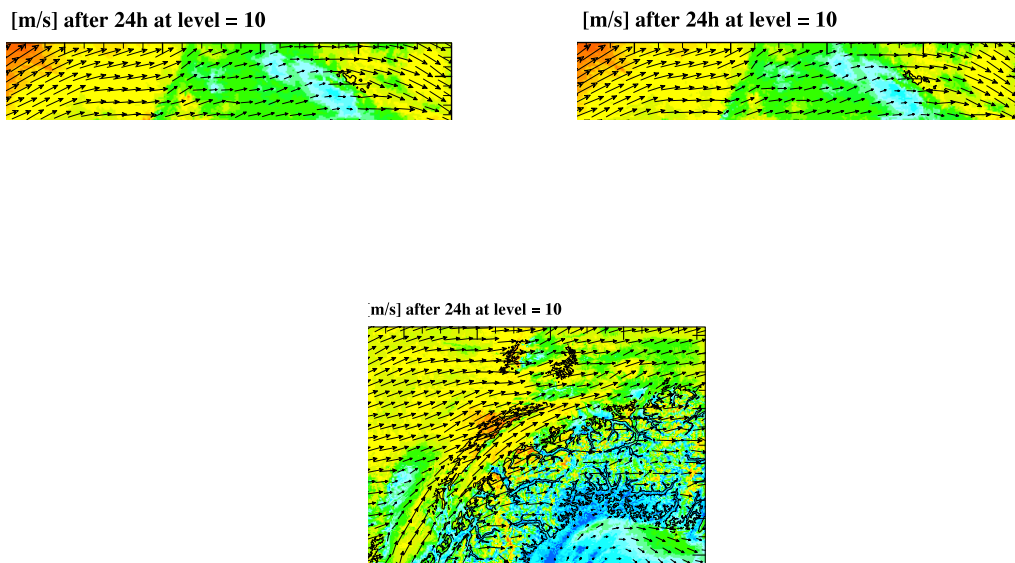
m/s] after 24h at level = 10

Figure 42: As in Figure 41 but for 10th model level above the ground.

2.2 km grid.

Finally, Fig. 44 compares vertically integrated cloud water for the CE forecast for 12 hours for 2.2 km (left panel) and 0.55 km (right panel) grid sizes. It presents high similarity of the obtained cloud fields, concerning both the cloud pattern and the amount of the condensate. The high-resolution simulation shows, however, a general presence of many very small-scale details absent in the lower-resolution simulations.

5.5   Summary and conclusions

The COSMO-EULAG prototype with EULAG dynamical core implemented into the software structure of the COSMO model and linked with basic physical parameterizations was successfully developed. The prototype was tested comparing its results with analogous COSMO model based on the compressible Runge-Kutta dynamical core for high-resolution 2.2 km horizontal grid sizes, for semi-realistic 24 hour forecast of the flow over Alps and its vicinity.

The tests have shown that the realistic CE results are similar to and consistent with the results of COSMO with RK dynamical core. It concerns not only basic parameters of the flow like wind and potential temperature distribution (the latter not shown) but also moist parameters like cloud condensate distribution and cumulative surface precipitation. Interesting differences between the models concern mountain gravity waves. While their distribution

Figure 43: Vertical cross section through wind velocity (left panels) and vertical velocity (right panels) for 24 hour forecast in the vicinity of Mt. Rosa with the CE model using horizontal grid size of 2.2 km (left, upper panel), 1.1 km (right panel) and 0.55 km (left lower panel).
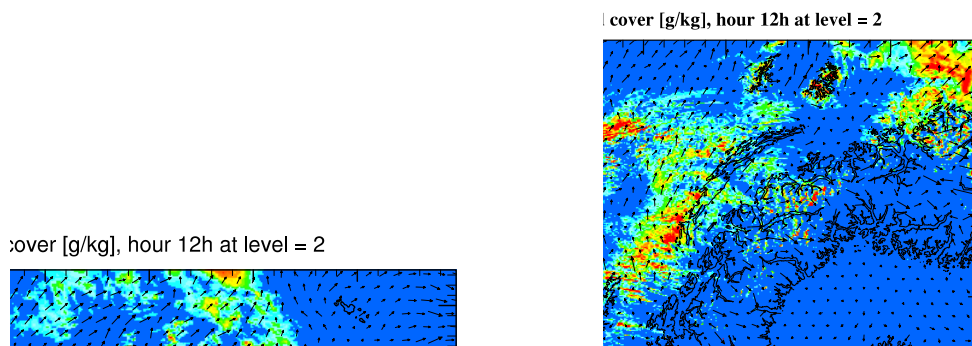

Figure 44: Vertically integrated cloud water (g/kg) for the CE forecast for 12 hours using 2.2 km (left panel) and 0.55 km (right panel) grid size.

is generally similar for both models, they differently influence the upper flow pattern leading to noticeable differences of the wind velocity in the jet stream area, while preserving similar general flow pattern. In general, no discrepancies of the CE simulations were found which would prove unsuitability of the EULAG dynamical core as well as of the anelastic approach for the very-high resolution regional NWP applications.

Finally, the CE prototype was tested for the varying horizontal resolutions with grid sizes of 2.2, 1.1 and 0.55 km. The simulations show a high degree of consistency of the results as well as the desirable robustness of the CE prototype. It was shown that with the increasing grid resolution the small scale variability of the flow increases with appearance of many small scale details especially in the near surface layer and gravity wave pattern. There are also resolution dependent differences in the jet stream velocity distribution suggesting effects of explicitly resolved gravity wave drag. There is no grid convergence of the solution for the orography significantly varying between the simulations.

References

Wojcik, D., K. Kurowski, B. Rosa and M. Ziemianski, 2012: A study on parallel performance of the EULAG F90/95 code. *Lecture Notes in Computer Science*, **7204**, 419–427.

Louis, J.-F., 1979: A parametric model of vertical eddy fluxes in the atmosphere. *Bound. Layer Meteor.* **17**, 187–202.

Ritter, B. and J.-F. Geleyn, 1992: A comprehensive radiation scheme for numerical weather prediction models with potential applications in climate simulations. *Mon. Wea. Rev.*, **120**, 303–325.

6   MPDATA as an alternative tracer advection scheme

Guy de Morsier and Marie Müllner

MeteoSwiss, Krähbühlstrasse 58, 8044 Zürich, Switzerland

6.1   Introduction

The results shown here were achieved during a 6 month diploma work done by Marie Müllner at MeteoSwiss in 2010 and for the full details see the original work by Muellner (2010) (in German).

In the current COSMO model the advection of the prognostic variables is done with an upwind scheme[1]. This scheme is efficient and therefore well adapted for a fast operational model but it is not monotone and not conservative. For the advection of positive definite variables such as scalar tracer fields, i.e. all water constituents, possible aerosol particles and gaseous substances or turbulent kinetic energy, finite volume schemes are more appropriate. For the tracer transport the model provides already different formulations but all of them have some drawbacks.

The aim of this work is to implement, evaluate and test a fully three dimensional advection scheme for the COSMO model. The proposed advection scheme is MPDATA (multidimensional positive definite advection transport algorithm, see Smolarkiewicz and Margolin (1998)) which is used in the EULAG (Eulerian/Semi-Lagrangian fluid solver, see Prusa et al. (2008)) numerical model. The code used for the implementation is from Piotr K. Smolarkiewicz and it can be found in the appendix of Muellner (2010).

6.2   Advection of prognostic fields

In COSMO the advection of the wind components, the temperature and the pressure is operated with an upwind scheme of the 5th order. The upwind scheme is a numerical discretization for hyperbolic partial differential equations.

We take the following advection equation

$$\frac{\partial u}{\partial t} + a \frac{\partial u}{\partial x} = 0 \tag{3}$$

A solution of this equation is a wave that travels along the x-direction with the speed a. For a numerical approximation of $\partial u/\partial t$ we use

$$\frac{\partial u}{\partial t} = \frac{u_i^{n+1} - u_i^n}{\Delta t}$$

and for the approximation of $\partial u/\partial x$ we use the backward difference if $a > 0$

$$\frac{\partial u}{\partial x} = \frac{u_i^n - u_{i-1}^n}{\Delta x} \tag{4}$$

and the forward difference if $a < 0$

$$\frac{\partial u}{\partial x} = \frac{u_{i+1}^n - u_i^n}{\Delta x} \tag{5}$$

---

[1]upwind scheme of 5th order is used (Wicker and Skamarock, 2002); more general operators are described in (Doms et al., 2011, section 8.1.2) .

After replacement in (3) and depending on a we obtain

$$\frac{u_i^{n+1} - u_i^n}{\Delta t} + a\frac{u_i^n - u_{i-1}^n}{\Delta x} = 0$$

or

$$\frac{u_i^{n+1} - u_i^n}{\Delta t} + a\frac{u_{i+1}^n - u_i^n}{\Delta x} = 0$$

By defining $a^+ = \max(a,0)$, $a^- = \min(a,0)$, $u_x^- = \frac{u_i^n - u_{i-1}^n}{\Delta x}$ and $u_x^+ = \frac{u_{i+1}^n - u_i^n}{\Delta x}$ we can put the 2 cases together to

$$u_i^{n+1} = u_i^n - \Delta t(a^+ u_x^- + a^- u_x^+)$$

or

$$u_i^{n+1} = u_i^n - C(u_i^n - u_{i-1}^n)$$

where C is the Courant-Friedrichs-Lewy number (CFL) which is defined by

$$C = \left|\frac{a\Delta t}{\Delta x}\right|$$

This upstream scheme is of the first order and is only stable if $C \leq 1$.

6.3 Positive definite advection

For the advection of tracers the model provides a semi-Lagrangian scheme (SL) and direction splitted finite volume schemes. For the latter, several flux formulations exist under which the flux calculation by Bott (1989) is the standard one and the others are the vanLeer-scheme and a piecewise parabolic method (PPM). The different methods should satisfy the following conditions so that the physical properties are fulfilled:

- conservation of mass

- computation of the fluxes in upstream direction

- no production of new maxima or minima

- conservation of tracer relationships during the advection

- efficient computation in spherical coordinates

The Bott-scheme is a one-dimensional scheme which is used in split mode for the different directions. The advection is done in 2 steps. After weighting the advective fluxes, corrections are applied to make the scheme positive definite. These corrections gives the scheme a precision of the second or forth order. The second order is usually used for operational applications and is hereafter referred to as Bott_2. The SL-scheme is a fully 3-dimensional but it does not conserve the mass. More details about these schemes can be found in the chapter 8.3 of Doms et al. (2011).

6.4 MPDATA in 3-dimensions

MPDATA is a finite difference scheme which is positive definite, mass conserving and efficient. Moreover through a flux correction it can be made monotonous. It is an iterative scheme. In a first step a donor cell approximation (also called upstream method, positive definite but
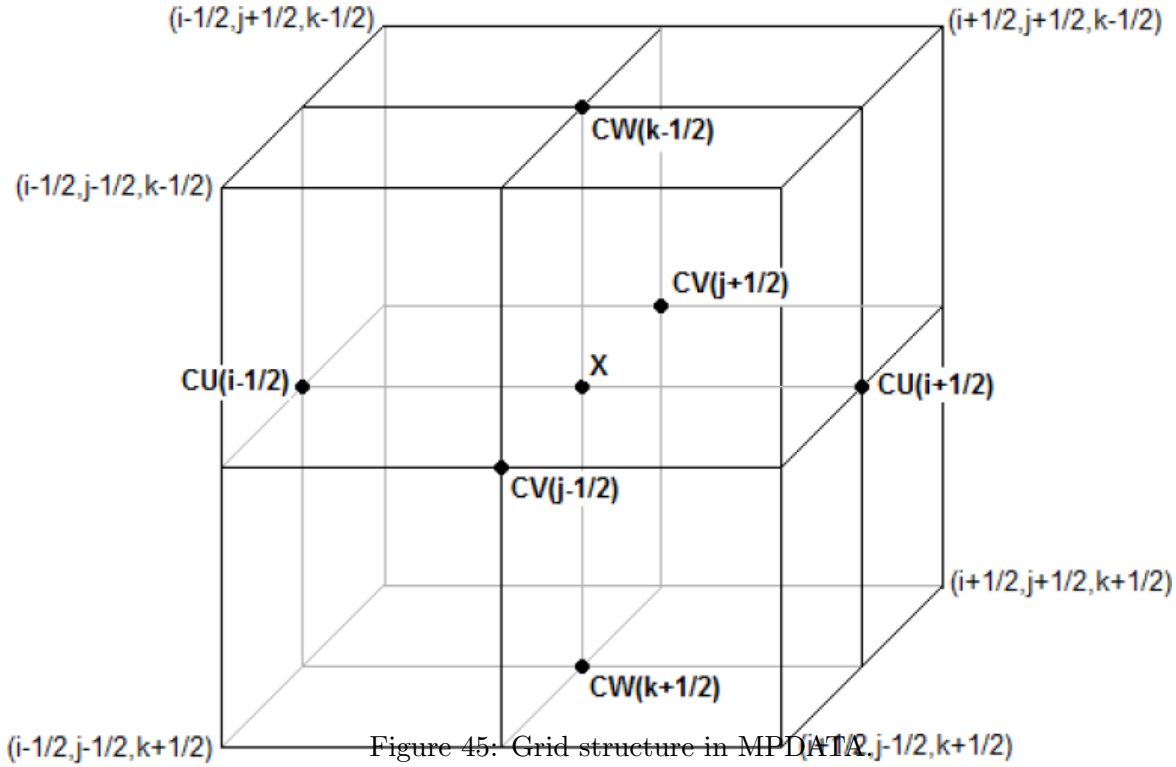
Figure 45: Grid structure in MPDATA.

only of first order accuracy) is made. In the second step which can be repeated, corrections are applied to make the scheme more accurate (second order in time and space). In the first step, the physical velocities are used but in the iterations, the velocities are computed from the advection fields and we call them diffusive velocities.

The grid used in MPDATA is basically composed of two set of grids which are shifted by half a grid length in all directions so that the center of the cells are whole numbers i (i.e. the contribution of the first grid) and the grid summits (contribution of the second grid) with half valued indexes $i \pm 1/2$, see Figure 45. The **X** sign marks in the figure the position of the quantity to be advected, **CU(i − 1/2)** and **CU(i + 1/2)** are the Courant numbers in the x direction, **CV(j − 1/2)** and **CV(j + 1/2)** are the Courant numbers in the y direction and **CW(k − 1/2)** and **CW(k + 1/2)** are the Courant numbers in the z direction.

The equation of advection in 3-dimensions is

$$\frac{\partial \Psi}{\partial t} = -\frac{\partial}{\partial x}(u\Psi) - \frac{\partial}{\partial y}(v\Psi) - \frac{\partial}{\partial z}(w\Psi) \tag{6}$$

The equation for the donor cell approximation of (6) is then

$$
\begin{aligned}
\Psi_{i,j,k}^{n+1} = \Psi_{i,j,k}^{n} &- [F(\Psi_{i,j,k}^{n}, \Psi_{i+1,j,k}^{n}, U_{i+\frac{1}{2},j,k}) - F(\Psi_{i-1,j,k}^{n}, \Psi_{i,j,k}^{n}, U_{i-\frac{1}{2},j,k})] \\
&- [F(\Psi_{i,j,k}^{n}, \Psi_{i,j+1,k}^{n}, V_{i,j+\frac{1}{2},k}) - F(\Psi_{i,j-1,k}^{n}, \Psi_{i,j,k}^{n}, V_{i,j-\frac{1}{2},k})] \\
&- [F(\Psi_{i,j,k}^{n}, \Psi_{i,j,k+1}^{n}, W_{i,j,k+\frac{1}{2}}) - F(\Psi_{i,j,k-1}^{n}, \Psi_{i,j,k}^{n}, W_{i,j,k-\frac{1}{2}})]
\end{aligned}
\tag{7}
$$

where the whole indexes correspond to the center and the half indexes are on the boundaries of the grid cells.

The Courant numbers U, V and W are $U \equiv u\delta t/\delta x$, $V \equiv v\delta t/\delta y$ and $W \equiv w\delta t/\delta z$ where the time step is δt and the grid space in x, y and z direction are $\delta x, \delta y$ and δz. The flux functions

are defined as

$$F(\Psi_L, \Psi_R, U) \equiv [U]^+ \Psi_L + [U]^- \Psi_R$$
$$F(\Psi_L, \Psi_R, V) \equiv [V]^+ \Psi_L + [V]^- \Psi_R \tag{8}$$
$$F(\Psi_L, \Psi_R, W) \equiv [W]^+ \Psi_L + [W]^- \Psi_R$$

with the Courant numbers

$$[U]^+ \equiv max(0, U), \ [U]^- \equiv min(0, U) \quad [V]^+ \equiv max(0, V), \ [V]^- \equiv min(0, V)$$

$$[W]^+ \equiv \max(0, W), \ [W]^- \equiv \min(0, W)$$

The $[U]^+$, $[V]^+$ and $[W]^+$ are the nonnegative, and $[U]^-$, $[V]^-$ and $[W]^-$ are the nonpositive parts of the Courant numbers. With a Taylor expansion and under the assumption that u, v and w are constant, we can again compute the donor cell approximation as:

$$\Psi_{i,j,k}^{n+1} = \Psi_{i,j,k}^n + \delta t \frac{\partial \Psi}{\partial t} + \frac{(\delta t)^2}{2} \frac{\partial^2 \Psi}{\partial t^2} + \hspace{3cm} O(\delta t^3)$$
$$= \Psi_{i,j,k}^n + \delta t \frac{\partial \Psi}{\partial t} + \frac{(\delta t)^2}{2} u^2 \frac{\partial^2 \Psi}{\delta x^2} + \frac{(\delta t)^2}{2} v^2 \frac{\partial^2 \Psi}{\delta y^2} + \frac{(\delta t)^2}{2} w^2 \frac{\partial^2 \Psi}{\delta z^2} +$$
$$\frac{(\delta t)^2}{2} 2uv \frac{\partial^2 \Psi}{\partial x \partial y} + \frac{(\delta t)^2}{2} 2uw \frac{\partial^2 \Psi}{\partial x \partial z} + \frac{(\delta t)^2}{2} 2vw \frac{\partial^2 \Psi}{\partial y \partial z} + O(\delta t^3)$$

$$\Psi_{i+1,j,k}^n = \Psi_{i,j,k}^n + \delta x \frac{\partial \Psi}{\partial x} + \frac{(\delta x)^2}{2} \frac{\partial^2 \Psi}{\partial x^2} + O(\delta x^3)$$

$$\Psi_{i-1,j,k}^n = \Psi_{i,j,k}^n - \delta x \frac{\partial \Psi}{\partial x} + \frac{(\delta x)^2}{2} \frac{\partial^2 \Psi}{\partial x^2} + O(\delta x^3)$$

$$\Psi_{i,j+1,k}^n = \Psi_{i,j,k}^n + \delta y \frac{\partial \Psi}{\partial y} + \frac{(\delta y)^2}{2} \frac{\partial^2 \Psi}{\partial y^2} + O(\delta y^3)$$

$$\Psi_{i,j-1,k}^n = \Psi_{i,j,k}^n - \delta y \frac{\partial \Psi}{\partial y} + \frac{(\delta y)^2}{2} \frac{\partial^2 \Psi}{\partial y^2} + O(\delta y^3)$$

$$\Psi_{i,j,k+1}^n = \Psi_{i,j,k}^n + \delta z \frac{\partial \Psi}{\partial z} + \frac{(\delta z)^2}{2} \frac{\partial^2 \Psi}{\partial z^2} + O(\delta z^3)$$

$$\Psi_{i,j,k-1}^n = \Psi_{i,j,k}^n - \delta z \frac{\partial \Psi}{\partial z} + \frac{(\delta z)^2}{2} \frac{\partial^2 \Psi}{\partial z^2} + O(\delta z^3)$$

After putting this in (7) we get the following advection diffusion equation

$$\frac{\partial \Psi}{\partial t} = -u \frac{\partial \Psi}{\partial x} - v \frac{\partial \Psi}{\partial y} - w \frac{\partial \Psi}{\partial z} + \tag{9}$$
$$(|U| - U^2) \frac{(\delta x)^2}{2 \delta t} \frac{\partial^2 \Psi}{\partial x^2} + (|V| - V^2) \frac{(\delta y)^2}{2 \delta t} \frac{\partial^2 \Psi}{\partial y^2} + (|W| - W^2) \frac{(\delta z)^2}{2 \delta t} \frac{\partial^2 \Psi}{\partial z^2} -$$
$$\frac{UV \delta x \delta v}{\delta t} \frac{\partial^2 \Psi}{\partial x \partial y} - \frac{UW \delta x \delta z}{\delta t} \frac{\partial^2 \Psi}{\partial x \partial z} - \frac{VW \delta y \delta z}{\delta t} \frac{\partial^2 \Psi}{\partial y \partial z}$$

The error which arises from the diffusion term in (9) is estimated with a donor cell approximation and then subtracted from (7) to obtain a higher precision. The equation (9) is written with the diffusive velocities u_d, v_d and w_d as

$$\frac{\partial \Psi}{\partial t} = -\frac{\partial}{\partial x}(u\Psi) - \frac{\partial}{\partial y}(v\Psi) - \frac{\partial}{\partial z}(w\Psi) + \frac{\partial}{\partial x}(u_d^{(1)}\Psi) + \frac{\partial}{\partial y}(v_d^{(1)}\Psi) + \frac{\partial}{\partial z}(w_d^{(1)}\Psi) \tag{10}$$

with the following definitions:

$$u_d^{(1)} \equiv (|U| - U^2)\frac{(\delta x)^2}{2\delta t}\frac{1}{\Psi}\frac{\partial \Psi}{\partial x} - r\frac{UV\delta x\delta y}{\delta t}\frac{1}{\Psi}\frac{\partial \Psi}{\partial y} - s\frac{UW\delta x\delta z}{\delta t}\frac{1}{\Psi}\frac{\partial \Psi}{\partial z}$$

$$v_d^{(1)} \equiv (|V| - V^2)\frac{(\delta y)^2}{2\delta t}\frac{1}{\Psi}\frac{\partial \Psi}{\partial y} - (1-r)\frac{UV\delta x\delta y}{\delta t}\frac{1}{\Psi}\frac{\partial \Psi}{\partial x} - t\frac{VW\delta y\delta z}{\delta t}\frac{1}{\Psi}\frac{\partial \Psi}{\partial z} \qquad (11)$$

$$w_d^{(1)} \equiv (|W| - W^2)\frac{(\delta z)^2}{2\delta t}\frac{1}{\Psi}\frac{\partial \Psi}{\partial z} - (1-s)\frac{UW\delta x\delta z}{\delta t}\frac{1}{\Psi}\frac{\partial \Psi}{\partial x} - (1-t)\frac{VW\delta y\delta z}{\delta t}\frac{1}{\Psi}\frac{\partial \Psi}{\partial y}$$

with r, s, $t \in \mathbb{R}$ can be chosen arbitrarily. The implementation is independent of the choice for r, s, $t \in [0,1]$ and as default values we choose r, s, $t = 0.5$ The diffusive velocities must be built at the grid cell boundaries. The explicit form depends if the boundary is horizontal or vertical but they can be written in the following dimensionless form

$$U^{(1)} \equiv \frac{u^{(1)}\delta t}{\delta x} = (|U| - U^2)A^{(1)} - 2rUVB^{(1)} - 2sUWC^{(1)}$$

$$V^{(1)} \equiv \frac{v^{(1)}\delta t}{\delta y} = (|V| - V^2)B^{(1)} - 2(1-r)UVA^{(1)} - 2tVWC^{(1)} \qquad (12)$$

$$W^{(1)} \equiv \frac{w^{(1)}\delta t}{\delta z} = (|W| - W^2)C^{(1)} - 2(1-s)UWA^{(1)} - 2(1-t)VWB^{(1)}$$

with

$$A^{(1)} \equiv \left[\frac{\delta x}{2\Psi}\frac{\partial \Psi}{\partial x}\right]_{i+1/2,j,k}^{n+1} = \frac{\Psi_{1+1,j,k}^{(1)} - \Psi_{i,j,k}^{(1)}}{\Psi_{1+1,j,k}^{(1)} + \Psi_{i,j,k}^{(1)}}$$

$$B^{(1)} \equiv \left[\frac{\delta y}{2\Psi}\frac{\partial \Psi}{\partial y}\right]_{i+1/2,j,k}^{n+1} = \frac{1}{2}\frac{\Psi_{i+1,j+1,k}^{(1)} + \Psi_{i,j+1,k}^{(1)} - \Psi_{i+1,j-1,k}^{(1)} - \Psi_{i,j-1,k}^{(1)}}{\Psi_{i+1,j+1,k}^{(1)} + \Psi_{i,j+1,k}^{(1)} + \Psi_{i+1,j-1,k}^{(1)} + \Psi_{i,j-1,k}^{(1)}}$$

$$C^{(1)} \equiv \left[\frac{\delta z}{2\Psi}\frac{\partial \Psi}{\partial z}\right]_{i+1/2,j,k}^{n+1} = \frac{1}{2}\frac{\Psi_{i,j,k+1}^{(1)} + \Psi_{i+1,j,k+1}^{(1)} - \Psi_{i,j,k-1}^{(1)} - \Psi_{i+1,j,k-1}^{(1)}}{\Psi_{i,j,k+1}^{(1)} + \Psi_{i+1,j,k+1}^{(1)} + \Psi_{i,j,k-1}^{(1)} + \Psi_{i+1,j,k-1}^{(1)}}$$

6.5   Non-oscillating option

The algorithm described in the previous paragraph is positive definite but not monotone. The solution can show wrong extrema. The reasons for the oscillations in the numerical solution are that on one side some fluxes are overestimated and on the other an underestimation can arise from the first order accuracy of the fluxes. The flux-corrected transport (FCT) methodology enforces appropriate limits to the fluxes and removes these oscillations. The adopted method merges the FCT with the iterative formalism of MPDATA (Smolarkiewicz and Grabowski, 1990). The numerical diffusion of the advection is reduced by limiting the anti-diffusive fluxes so that no unphysical extrema occur in the solutions.

General form of the FCT methodology   Starting with the conservation of a time dependent fluid variable (e.g. mass, momentum) Ψ can be written as

$$\frac{\partial \Psi}{\partial t} + \nabla \cdot (\Psi\mathbf{u}) = S$$

where $\mathbf{u}$ is the fluid velocity and S is a source term. First Ψ is advected. In the second FCT step Ψ is numerically diffused so that the solution is positive everywhere if the starting

profile Ψ^0 was positive. The source term S is added to obtain the low order value Ψ^l. In the next step the anti-diffusive fluxes are computed and we obtain a higher order approximation Ψ^h. The anti-diffusive fluxes are limited to not generate any new extrema and not to reduce any extrema of the start profile. Applying these fluxes to Ψ^l gives the new solution Ψ^n which is positive and monotone.

Limiters in MPDATA   First the extrema Ψ^{min} and Ψ^{max} are computed

$$\Psi_{i,j,k}^{l,min} = \min(\Psi_{i,j,k}^l, \Psi_{i-1,j,k}^l, \Psi_{i+1,j,k}^l, \Psi_{i,j-1,k}^l, \Psi_{i,j+1,k}^l, \Psi_{i,j,k-1}^l, \Psi_{i,j,k+1}^l)$$

$$\Psi_{i,j,k}^{l,max} = \max(\Psi_{i,j,k}^l, \Psi_{i-1,j,k}^l, \Psi_{i+1,j,k}^l, \Psi_{i,j-1,k}^l, \Psi_{i,j+1,k}^l, \Psi_{i,j,k-1}^l, \Psi_{i,j,k+1}^l)$$

Then Ψ^h is computed using (7) and the new extrema Ψ^{min} and Ψ^{max} are found

$$\Psi_{i,j,k}^{h,min} = \min(\Psi_{i,j,k}^h, \Psi_{i-1,j,k}^h, \Psi_{i+1,j,k}^h, \Psi_{i,j-1,k}^h, \Psi_{i,j+1,k}^h, \Psi_{i,j,k-1}^h, \Psi_{i,j,k+1}^h, \Psi_{i,j,k}^{l,min})$$

$$\Psi_{i,j,k}^{h,max} = \max(\Psi_{i,j,k}^h, \Psi_{i-1,j,k}^h, \Psi_{i+1,j,k}^h, \Psi_{i,j-1,k}^h, \Psi_{i,j+1,k}^h, \Psi_{i,j,k-1}^h, \Psi_{i,j,k+1}^h, \Psi_{i,j,k}^{l,max})$$

The flux terms in (8) are computed and in the next step the total in- and outgoing anti-diffusive fluxes F^{in} and F^{out} of each cell can be computed as

$$F_i^{in} = \max(F_{i-1/2}, 0) - \min(F_{i+1/2}, 0) \ , \ F_i^{out} = \max(F_{i+1/2}, 0) - \min(F_{i-1/2}, 0)$$

$$F_j^{in} = \max(F_{j-1/2}, 0) - \min(F_{j+1/2}, 0) \ , \ F_j^{out} = \max(F_{j+1/2}, 0) - \min(F_{j-1/2}, 0)$$

$$F_k^{in} = \max(F_{k-1/2}, 0) - \min(F_{k+1/2}, 0) \ , \ F_k^{out} = \max(F_{k+1/2}, 0) - \min(F_{k-1/2}, 0)$$

The partial in- and outgoing fluxes f^{in} and f^{out} which have to be applied to each grid cell are then

$$f_i^{in} = \frac{\Psi_{i,j,k}^{h,max} - \Psi_{i,j,k}^l}{F_i^{in}} \ , \ f_i^{out} = \frac{\Psi_{i,j,k}^l - \Psi_{i,j,k}^{h,min}}{F_i^{out}}$$

$$f_j^{in} = \frac{\Psi_{i,j,k}^{h,max} - \Psi_{i,j,k}^l}{F_j^{in}} \ , \ f_j^{out} = \frac{\Psi_{i,j,k}^l - \Psi_{i,j,k}^{h,min}}{F_j^{out}}$$

$$f_k^{in} = \frac{\Psi_{i,j,k}^{h,max} - \Psi_{i,j,k}^l}{F_k^{in}} \ , \ f_k^{out} = \frac{\Psi_{i,j,k}^l - \Psi_{i,j,k}^{h,min}}{F_k^{out}}$$

Finally in the last step each of these partial anti-diffusive fluxes are limited so that no undershooting is produced at the exit and no overshooting at the entry of the grid cell. For the pseudo velocities u, v and w we use

$$u_{i+1/2,j,k} = \min(1, f_i^{out}, f_{i+1}^{in}) \max(0, u_{i+1/2,j,k}) + \min(1, f_i^{in}, f_{i+1}^{out}) \min(0, u_{i+1/2,j,k})$$

$$v_{i,j+1/2,k} = \min(1, f_j^{out}, f_{j+1}^{in}) \max(0, v_{i,j+1/2,k}) + \min(1, f_j^{in}, f_{j+1}^{out}) \min(0, v_{i,j+1/2,k})$$

$$w_{i,j,k+1/2} = \min(1, f_k^{out}, f_{k+1}^{in}) \max(0, w_{i,j,k+1/2}) + \min(1, f_k^{in}, f_{k+1}^{out}) \min(0, w_{i,j,k+1/2})$$
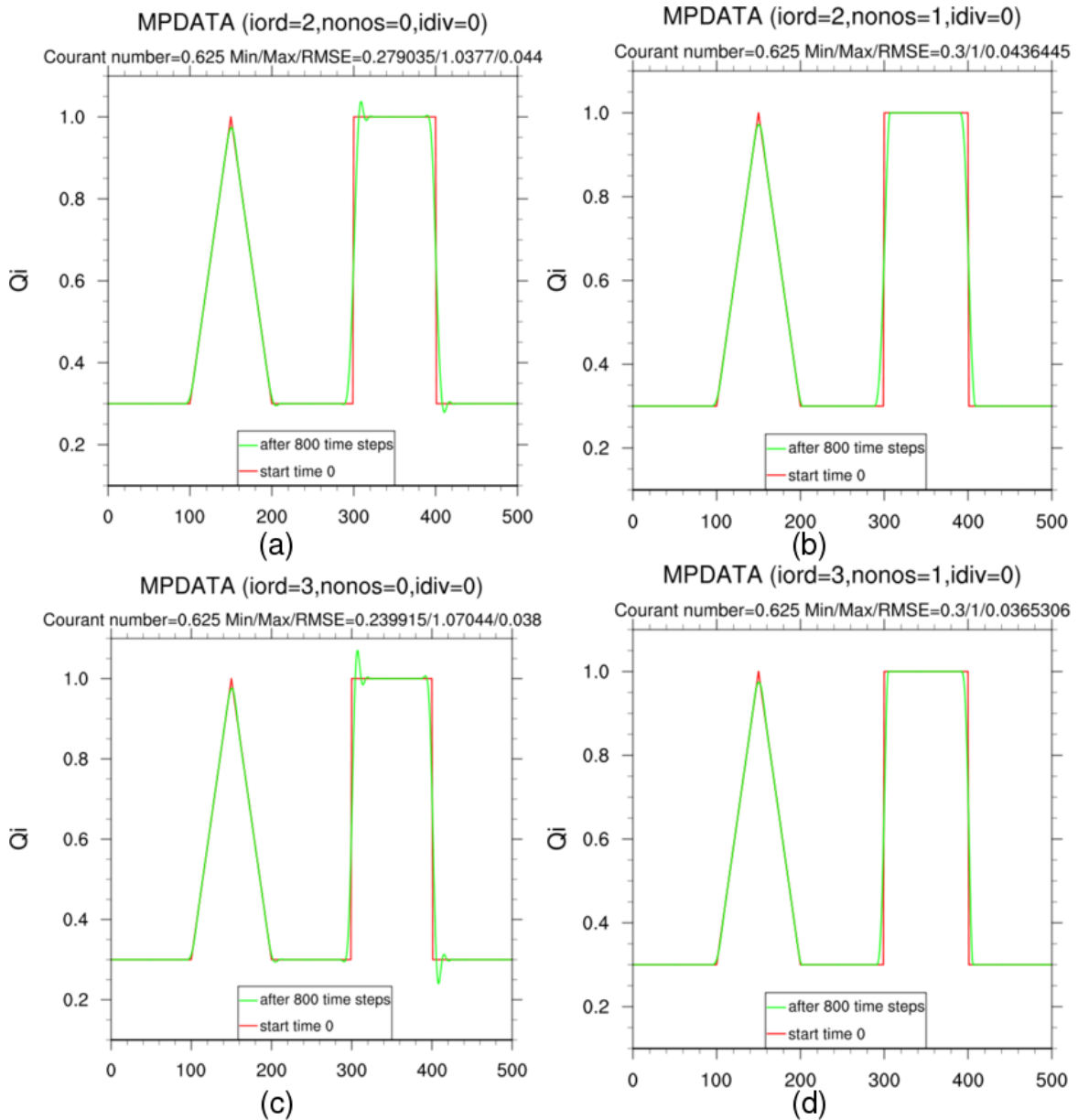
Figure 46: First example of MPDATA in one dimension, details see text.

6.6   Illustration in a one dimensional case

To show how MPDATA works a simple advection in one dimension is used here. The initial distributions of the tracer (Qi) are a triangle and a rectangular function with maximum value 1 and minimum value 0.3 over 100 grid points. These are shown in red in the Figure 46. A constant positive velocity (to the right) is applied to the tracer with a Courant number of 0.625 and periodic boundary conditions are used. After 800 time steps the distribution has passed over all the 500 grid points and is back at the initial position (in green in Figure 46) and the impact of the different advection options is visible. These options are the number of iterations (*iord*) used in the MPDATA algorithm, the non-oscillating option described in the previous section if *nonos* = 1 and a switch for non-divergent fields (*idiv* = 1 if the divergence of the velocity field is different than zero). For *iord* = 1 only the donor cell advection is operated and the scheme is very diffusive (not shown). With *iord* = 2 we have the basic

MPDATA scheme with only one anti-diffusive flux computed. This step can be repeated although for *iord* higher than 3 no significant improvement is obtained (not shown). On the top left of Figure 46 *iord* is equal 2 and on the left of the rectangular tracer there is a 4% overshooting and on the right an undershooting of 7%. This effect is totally absent in the part (b) of the figure where *nonos* = 1. With an extra iteration (*iord* = 3, lower left part c) the over- and undershooting are worse (respectively 7 and 20%) but the root mean square error (RMSE) of the overall distribution is reduced. The best results are obtained in the lower right corner in part (d) of the figure and one can also state that the triangular distribution does not seem to change much for any of the shown options. In a more stringent
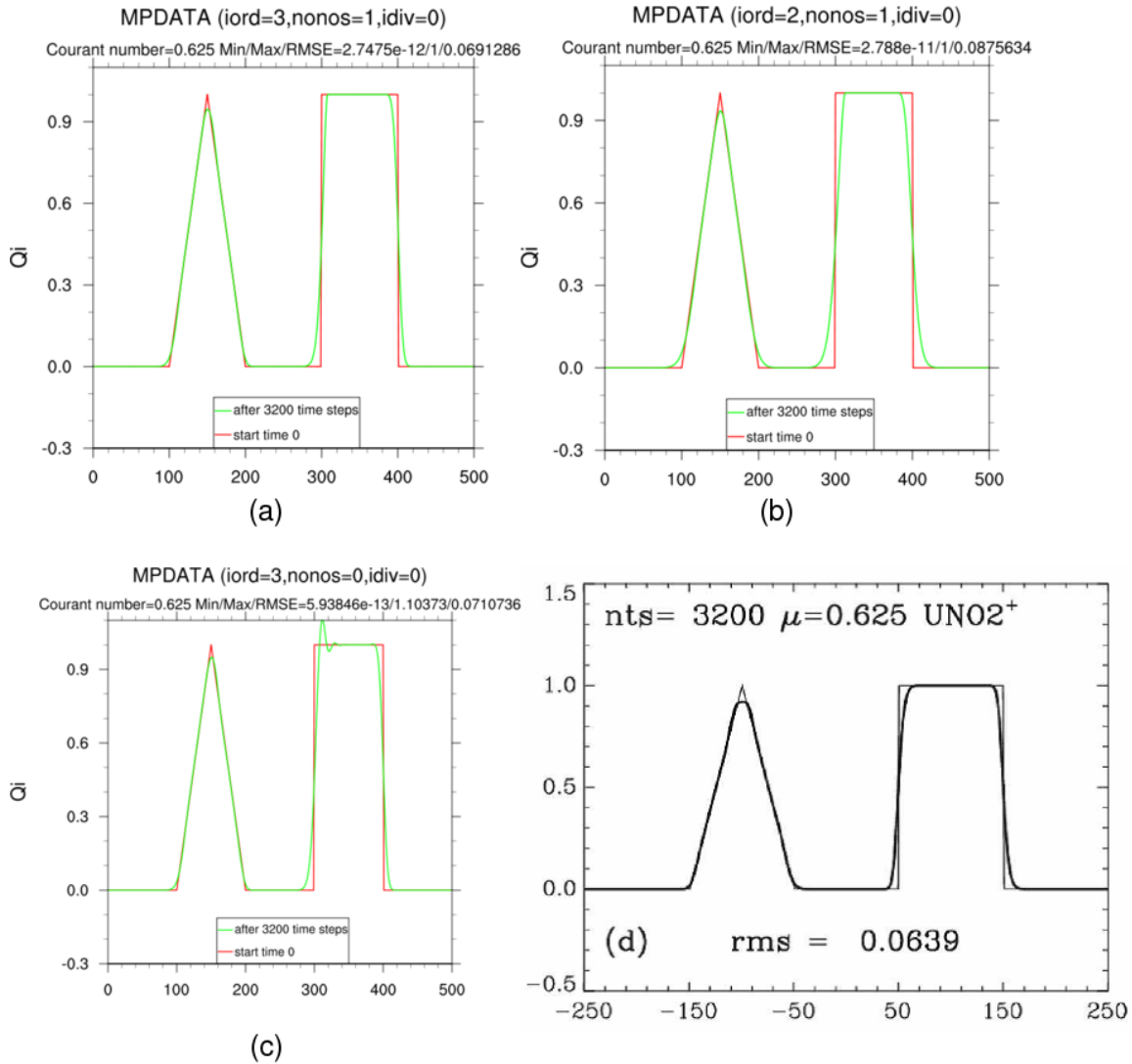

Figure 47: Second example of MPDATA in one dimension, details see text.

test the 2 previous distributions are compared after 3200 time steps which correspond to 4 complete rotations. In contrast to Figure 46 the starting distributions have a minimum of 0 and only three options are shown in Figure 47. In the lower right part an upstream non-oscillatory (UNO2+) solution from Li (2008) is displayed for comparison. The RMSE with the best MPDATA options (iord=3, nonos=1) is shown in the upper left part (a) and is similar to the UNO2+ method.

6.7 Advection tests

In a first configuration MPDATA was tested by conducting synthetic experiments with the module src_artifdata. This module permits to construct artificial initial and boundary data and all the usual settings of the model and then to do component testing while still using the whole COSMO model in its version 4.12 for the dynamics of the flow. MPDATA could therefore be easily compared to results obtained with Bott_2 or the semi-Lagrangian scheme (SL).

These so-called solid body rotation tests were computed on a domain of 80x80 grid points with an horizontal resolution of 2.2km. The time step used was 20s. There is no orography and the vertical extension of the model has no impact but permits to conduct different experiments on different model levels.
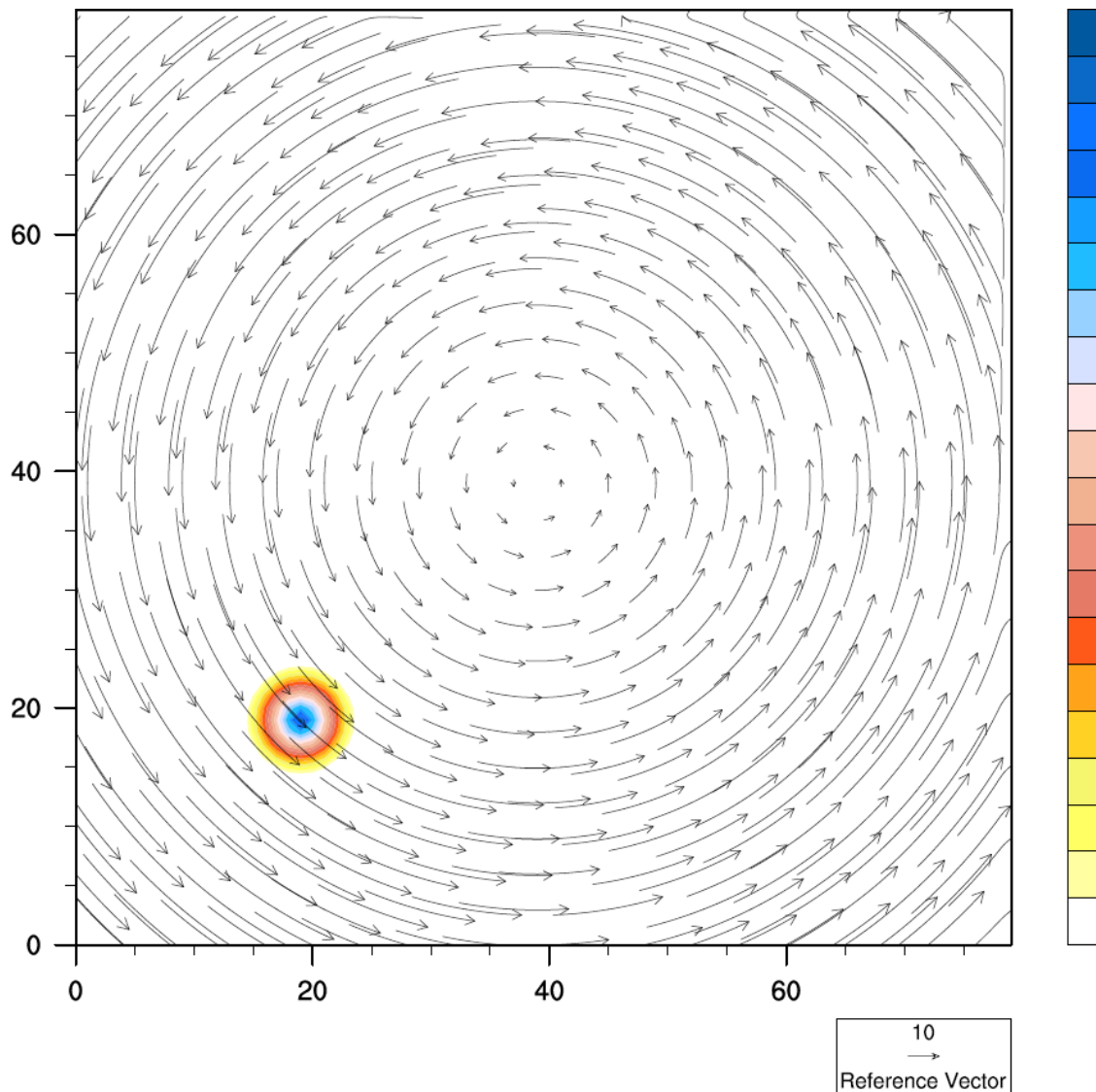

Figure 48: Rotating wind field in m/s over the whole computational domain with the starting tracer concentration (cone with base radius of 5 grid points) in colours centered at position (20,20).

Rotating cone test with 0 background   As in the previous paragraph the specific cloud ice content q_i (in units of kg/kg) was used as a tracer and initialized to zero everywhere except

for a cone centered over the position $(i, j) = (20, 20)$ and with radius of 5 grid points and placed on the 10th level of the model so that we can write

$$q_i(i, j, 10) = \max(0.0, 1.0 - \sqrt{((i - i_{max})/5)^2 + ((j - j_{max})/5)^2})$$

where the maximum of q_i is 1 and is positioned on the grid point $(i_{max}, j_{max} = (20, 20)$. The rotating wind field is defined as

$$u(i, j, k) = -\omega(j - j_0) \quad v(i, j, k) = \omega(i - i_0) \quad w(i, j, k) = 0.0$$

where $\omega = 0.97 m/s$, $u(i, j, k)$, $v(i, j, k)$ and $w(i, j, k)$ are the wind velocities in the i-, j- and k-direction and (i_0, j_0) is the mid point of the horizontal layer. The stationary winds and the distribution of the tracer at time 0 are shown in Figure 48.

The rotation period is 4h and the Courant number at the location of the tracer is about 0.3 but the maximum values are close to 0.5 in the corners of the domain.

The tracer should theoretically be transported without changing its shape and after 4h of computation it should be back in its starting position. To show the characteristics of the different schemes, the isolines of the tracer concentrations of the MPDATA method are drawn on top of the colored results of the Bott_2 scheme. Figure 49 displays 2 different settings of the MPDATA scheme. For MPDATA one can see that the maximum values have been reduced by 78% and 66% whereas Bott_2 has only been reduced by 50%. The results of the SL scheme are not shown but are very similar to the Bott_2 with a slightly better maximum value of 0.510. There is not only a reduction of the maximum but there is also a phase shift in the position of this value.

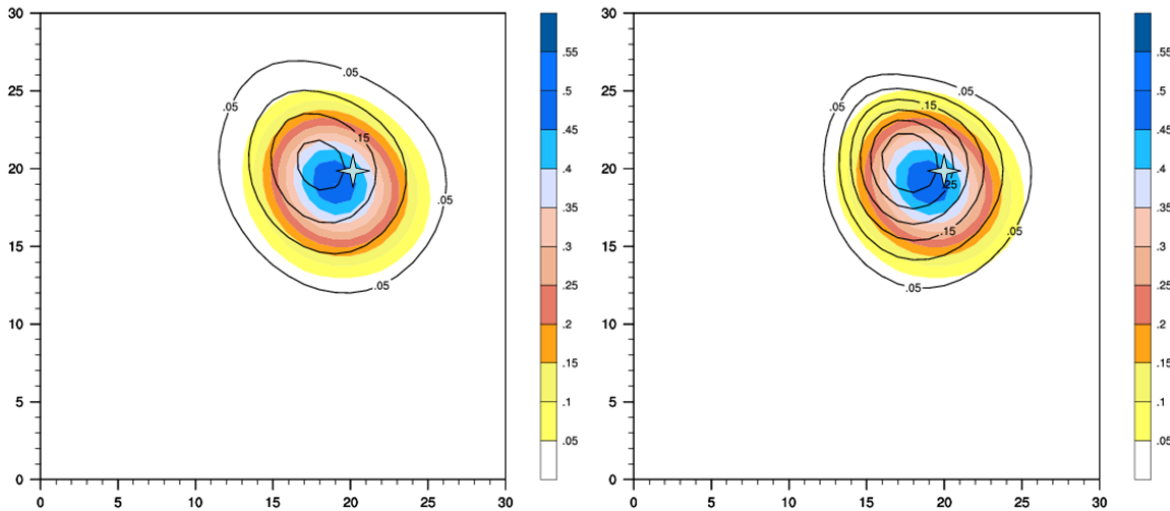We compute the following statistical measures to quantify the results:

Figure 49: Zoom of the lower left domain with the tracer concentrations after one complete rotation of a cone with maximum of 1 and horizontal radius of 5 grid points centered at the position (20,20).

- the phase error E_{phase} is defined as the distance between the exact maximum position (i^{start}, j^{start}) and the computed one (i^{end}, j^{end}):

$$E_{phase} = \sqrt{(i^{start} - i^{end})^2 + (j^{start} - j^{end})^2} \tag{13}$$

- the diffusion error is

$$E_{diffusion} = \max(q_i^{start}) - max(q_i^{end}) \tag{14}$$

- the L2-norm is

$$E_{L2} = \sqrt{\sum_{i=1}^{N} A_i \cdot (q_i^{start} - q_i^{end})^2} \tag{15}$$

where N is the number of grid cells and A_i is the area of the grid cell.

Advection scheme after one rotation	L2-norm E_{L2}	Maximum value	E_{phase}	$E_{diffusion}$
Bott_2	3.068	0.501	1.414	0.499
Semi-Lagrange	3.147	0.510	1.414	0.490
MPDATA				
iord=2, nonos=0	5.798	0.219	2.000	0.781
iord=3, nonos=0	4.925	0.348	2.236	0.652
iord=2, nonos=1	5.795	0.217	2.000	0.783
iord=3, nonos=1	4.906	0.344	2.000	0.656

Table 8: Overview of the different schemes for the rotating cone test with 0 background.

All the results of the different experiments with the rotating cone are shown in Table 8. The smallest MPDATA diffusion error is given by the experiment with *iord* = 3 and *nonos* = 0 but its phase error is the largest and the overall smallest L2-norm is given by the Bott_2 scheme although its diffusion error is larger than the SL experiment.

Rotating cylinder test with non-zero background
In this test the tracer has a value of 0.3 over the whole domain and only in a radius of 5 grid points around the center position $(i, j) = (20, 20)$ does the tracer have a value of 1.0. The rotating wind field is the same as in the previous cone test. Figure 50 shows the same 2 settings of the MPDATA scheme on top of the Bott_2 solution as for the rotating cone test. Although we use the non-oscillating option for MPDATA local minima and maxima appear in the vicinity of the main tracer concentration. This is also the case for the Bott_2 but the trail behind the main concentration is much smaller than with MPDATA. For MPDATA one can see that the maximum values have been reduced by 37% and 26% whereas Bott_2 has only been reduced by 16%. This is much better than in the previous test but because of the local extrema the overall L2-norm is much larger in this experiment (see Table 9). The results of the SL scheme are not shown here because there is a boundary undershooting problem for this experiment.

All the results of the different experiments with the rotating cylinder are shown in Table 9. The smallest MPDATA diffusion error is again given by the experiment with *iord* = 3 and *nonos* = 0 with a maximum reduction of only 21% but its phase error is again the largest and the overall smallest L2-norm is again given by the Bott_2 scheme and its diffusion error is also the overall smallest.
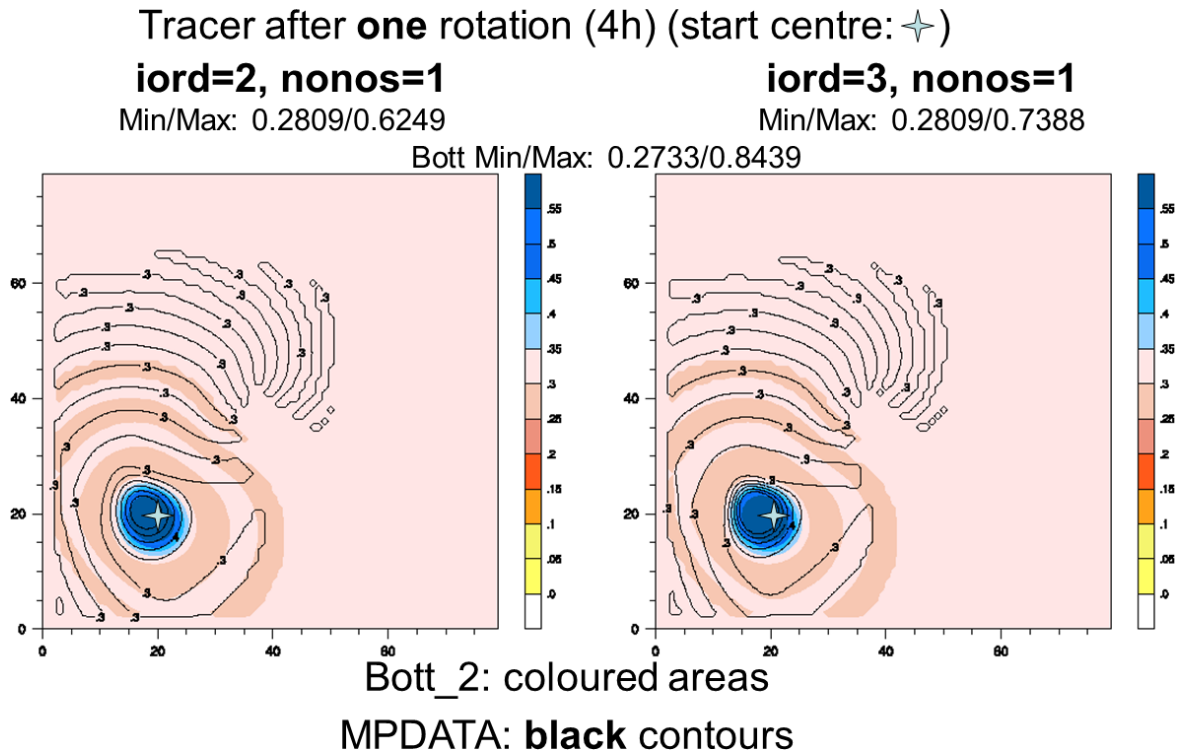
Figure 50: Tracer concentrations after one complete rotation (4h) of a cylinder of maximum 1 and horizontal radius of 5 grid points centered at the position (20,20) on top of a background value of 0.3.

Advection scheme after one rotation	L2-norm E_{L2}	Minimum value	Maximum value	Phase error	Diffusion error
Bott_2	5.233	0.273	0.844	1.414	0.156
Semi-Lagrange	12.574	0.125	0.843	1.414	0.157
MPDATA					
iord=2, nonos=0	6.907	0.261	0.633	2.000	0.367
iord=3, nonos=0	6.771	0.199	0.785	3.162	0.215
iord=2, nonos=1	6.882	0.281	0.625	2.000	0.375
iord=3, nonos=1	6.402	0.281	0.739	2.000	0.261

Table 9: Overview of the different schemes for the rotating cylinder test with non-zero background.
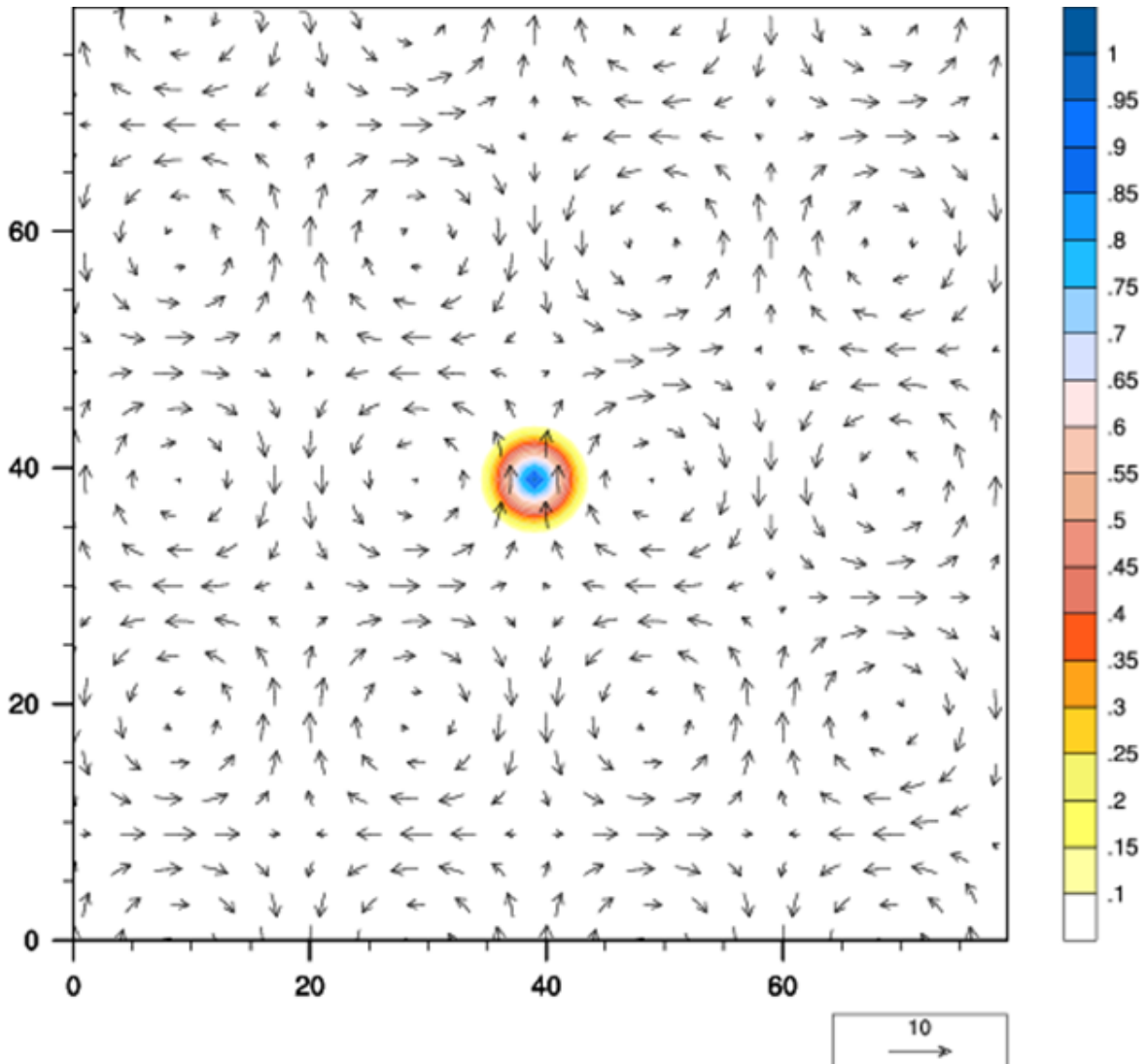
Figure 51: Wind field in m/s for the deformational flow test with the starting tracer concentration (cone with base radius of 5 grid points) in colours centered at position (40,40).

6.8 Deformation flow tests

The stability and the qualitative value of the different advection schemes can be best tested in this set-up because the splitting schemes have here the potential to fail. The wind field is now composed of series of symmetrical vortices with all neighbors rotating in opposite directions and the divergence is non-zero. Therefore the MPDATA switch $idiv = 1$ needs to be used for this test. The purely horizontal wind speed components ($w(i, j, 10) = 0$) are defined as follows

$$u(i, j, 10) = \frac{120.0 \cdot \pi}{80.0} \sin(\frac{4.0 \cdot \pi}{80.0} i) \sin(\frac{4.0 \cdot \pi}{80.0} j)$$
$$v(i, j, 10) = \frac{120.0 \cdot \pi}{80.0} \cos(\frac{4.0 \cdot \pi}{80.0} i) \cos(\frac{4.0 \cdot \pi}{80.0} j)$$

Similar to the first advection test, a cone tracer q_i of 5 grid point radius is placed on the 10th level at the centre of the domain $(i_{max}, j_{max}) = (40, 40)$ and every where else set to zero

$$q_i(i, j, 10) = \max(0.0, 1.0 - \sqrt{((i - i_{max})/5)^2 + ((j - j_{max})/5)^2})$$

The shear flow generated by the equations above is shown in Figure 51 where the initial distribution of the tracer at time 0 is exactly split in the middle by a counterclockwise and a clockwise rotating vortex. The tracer will therefore be transported first to the North reaching a strongly divergent zone (with a saddle point at the center of the top 4 complete vortices) where the tracer will be split in two parts, one going West and another going East. Near the tracer maximum the Courant number is 0.04. The time for the tracer to go round once depends on the starting position and as the fluid trajectories are not circles for a position close to the center of the domain the period can be analytically computed by $P_c = 2\pi/(k^2|A|) = L^2/(8\pi|A|)$ where L is the computational domain and A is the amplitude of the stream function which describes the wind field (see formula (12) in Staniforth et al. (1987)). This corresponds here to about 1500 time steps so that after 10 hours of simulation the tracer has gone round about 1.2 times.

Advection scheme	Maximum after 5h	Maximum after 10h
Bott_2	0.297	0.148
Semi-Lagrange	0.334	0.164
MPDATA		
iord=2, nonos=0	0.278	0.126
iord=3, nonos=0	0.299	0.149
iord=2, nonos=1	0.267	0.128
iord=3, nonos=1	0.287	0.146

Table 10: Maximum values of the cone tracer in a deformational flow field.

Figure 52 displays the tracer concentration with the Bott_2 and the SL scheme and they can be compared with 2 different settings of the MPDATA scheme in Figure 53. Although the setup is completely symmetric the results show some small asymmetry which can be perhaps explained by the Coriolis force which was not excluded. The maximum tracer values of the experiments are summarized in Table 10 and for the *iord* = 3 and *nonos* = 0 configuration of MPDATA the values are higher than for Bott_2 but the results for SL are overall best.

The test referred to in Smolarkiewicz (1982) and in Staniforth et al. (1987) is laid out in a larger domain with a square side of 100 grid points and starts with a cone with a radius of 15 grid points which interacts with six vortices. The amplitude of the stream function is also reduced from 30 to 8 so that the time needed to reach $3T/200$ ($T = 2637.6$) is of 32 hours. Three different advection schemes are shown in Figure 54 and can be compared to the analytical solution shown in Figure 4a of Staniforth et al. (1987). The overall symmetry of this setup is much higher than with the previous deformation flow test. The solution with the highest wall on the North side of the two central vortices and between these two vortices is the SL configuration. The MPDATA configuration maintains higher maximum values than the Bott_2 scheme and the advection of the tracer near the North saddle point produces far reaching 'horns' which are also in the analytical solution, but the southern tracer extension from the South saddle point is the smallest with MPDATA.

6.9   Conclusions

MPDATA is a 3-dimensional advection scheme which was introduced by Piotr Smolarkiewicz. It is based on the upstream scheme. The strong diffusion of the upstream scheme is reduced
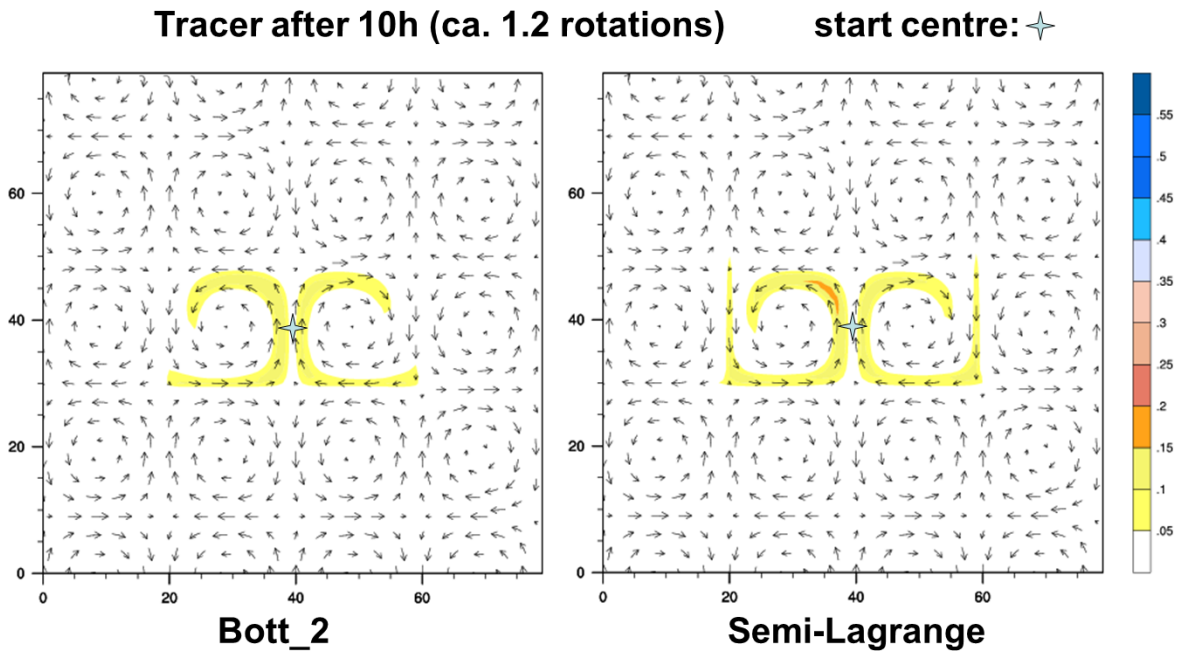
Figure 52: Tracer concentrations after more than a complete rotation of a cone with maximum of 1 and horizontal radius of 5 grid points centered in the middle of the domain for the Bott_2 (left) and semi-Lagrangian (right) advection scheme.
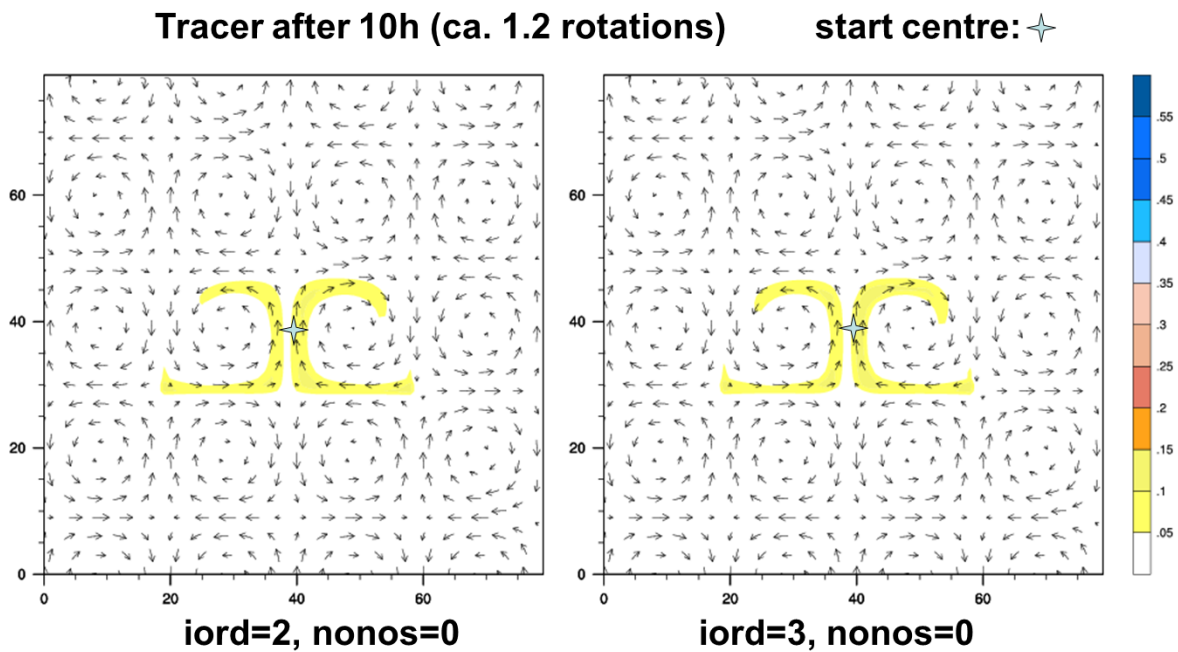
Figure 53: Same as Figure 52 but for 2 different settings of the MPDATA scheme.
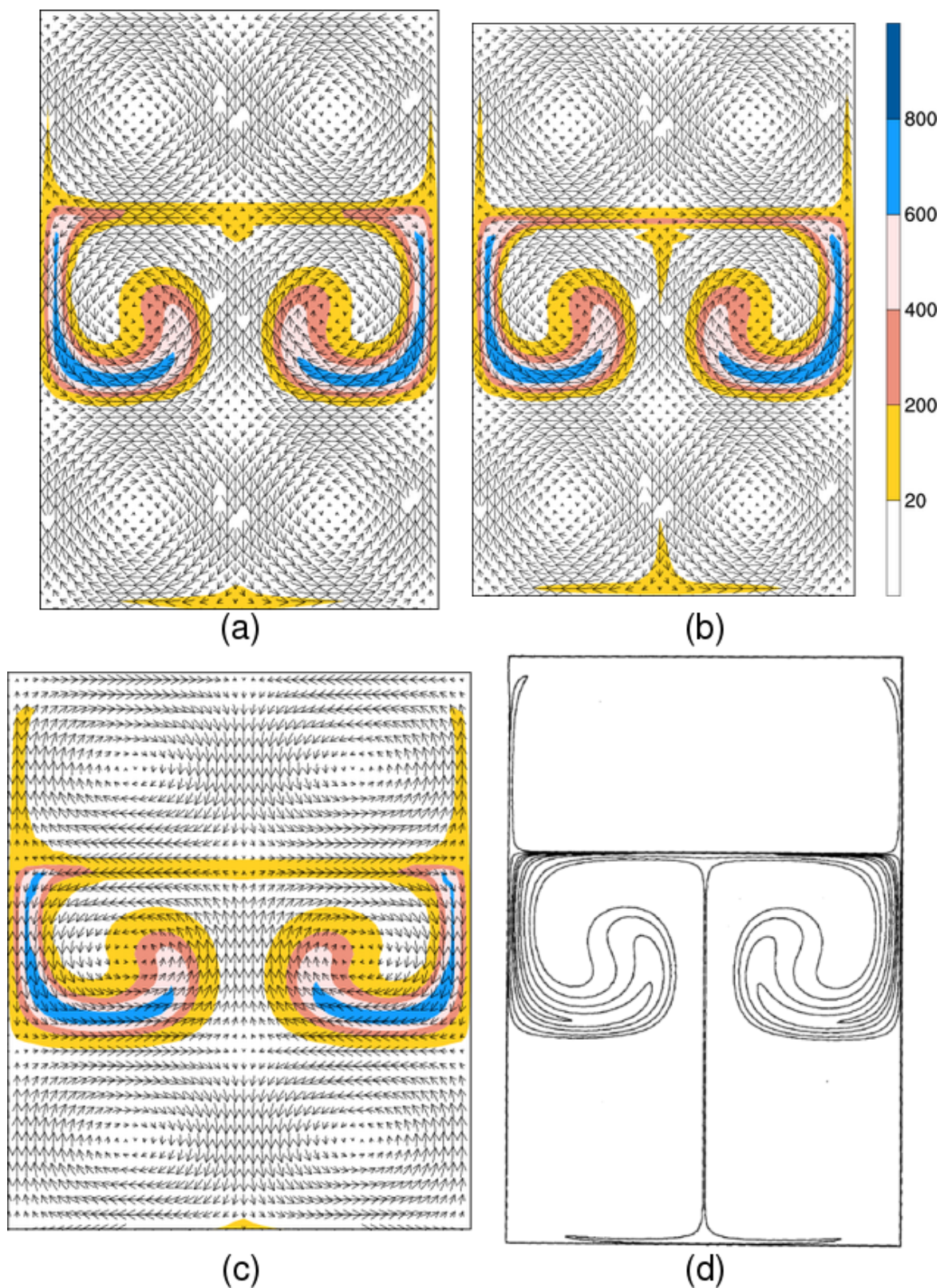
Figure 54: Tracer concentrations after 32 hours for (a) the Bott_2 scheme, (b) the SL scheme, (c) MPDATA scheme with *iord* = 3 and *nonos* = 1. (d) is the Fig. 4a of Staniforth et al. (1987) for *T*/50 with (*T* = 2637.6). All the isolines are 0.8 (not present in (a), (b) or (c)), 0.6, 0.4, 0.2, 0.02. Except for (d) the divergent flow field of the internal six vortices where the tracer is confined is also shown.

by iterating anti-diffusive steps.

Compared to splitted schemes, as the Bott-scheme, MPDATA has the advantage not to have the tendency to oscillate and is therefore more precise and as a fully 3-dimensional scheme it therefore can not empty a grid box in a single step. But MPDATA is more diffusive as the Bott_2 scheme or the 3-dimensional semi-Lagrangian scheme (SL). This was particularly the case in the solid body rotation tests because in the deformation flow tests the maximum values of MPDATA were better than for the Bott_2 scheme. To be fair a fully 3-dimensional test was not conducted so that the full advantage of MPDATA as a non-splitted scheme could not be completely compared to the Bott-scheme.

The computing time for MPDATA as used in this work is considerably larger than for Bott_2 or for the Semi-Lagrange scheme but no effort was undertaken to optimize the scheme as it is already done for the two other schemes which can be used for operations. For the moment MPDATA runs only on one processor and to operate weather forecasts one should consider to use a parallelised and optimized version of MPDATA and then to compare the results of the different advection schemes.

References

Bott A., 1989: A positive definite advection scheme obtained by nonlinear renormalization of the advective fluxes. *Monthly Weather Review*, **117**, 1006-1015.

Doms G. et al., 2011: A Description of the Nonhydrostatic Regional COSMO-Model. Part I: Dynamics and Numerics. Available at *http://www.cosmo-model.org*

Li J.-G., 2008: Upstream nonoscillatory advection schemes, *Monthly Weather Review*, **136**, 4709-4729.

Müllner M., 2010: Implementierung eines dreidimensionalen Advektionsschemas für den dynamischen COSMO Kern, Diplomarbeit bei der Fakultät für Mathematik der Technischen Universität Chemnitz, pp. 69.

Prusa J. M., P. K. Smolarkiewicz, A. A. Wyszogrodzki, 2008: EULAG, a computational model for multiscale flows. *Computer and Fluids*, **37**, 119-1207.

Smolarkiewicz P. K., 1982: The multi-dimensional Crowley advection scheme. *Monthly Weather Review*, **113**, 1050-1065.

Smolarkiewicz P. K. and W. W. Grabowski, 1990: The Multidimensional Positive Definite Advection Transport Algorithm: Nonoscillatory Option. *Journal of Computational Physics*, **86**, 355-375.

Smolarkiewicz P. K. and L.G. Margolin, 1998: MPDATA: a finite-difference solver for geophysical flows. *Journal of Computational Physics*, **140**, 459-480.

Staniforth A., J. Côté and J. Pudykiewicz, 1987: Comment on "Smolarkiewicz's deformational flow". *Monthly Weather Review*, **115**, 894-900.

Wicker, L. and W. Skamarock, 2002: Time-splitting methods for elastic models using forward time schemes. *Monthly Weather Review*, **130**, 2088-2097.

7 Normal mode analysis of anelastic and compressible equation sets

Michael Baldauf

Deutscher Wetterdienst, Germany

7.1 Introduction

Inspection of linear wave expansion properties is often one of the starting points in the investigation of a hyperbolic equation set. Such an analysis gives also a first impression about the accuracy of possible approximations made in an equation set. Here we will investigate the wave expansion properties of several anelastic approximations of the Euler equations. Such a study has already been done by Davies et al. (2003) and some of their results will be reproduced here. Contrariwise, the current COSMO model uses the fully compressible Euler equations with a split-explicit solver by Wicker and Skamarock (2002). This time-splitting approach needs a so-called divergence damping to be stable (Baldauf, 2010), which can be considered as an artificial additional term in the compressible Euler equations. It will be of interest in which manner such a term will change the wave expansion properties, too. In the frame of the CDC priority project, it is of particular interest to compare the divergence damping with the anelastic equations. This comparison is done here on the level of the analytic equations.

Such an investigation has been already performed by Baldauf (2011), where the anelastic approximation sets of Ogura and Phillips (1962), here denoted as 'OP62', Wilhelmson and Ogura (1972) ('WO72'), and Lipps and Hemler (1982) ('LH82') have been compared with a compressible equation set with the artificial 3-dimensional (3D) divergence damping. The equation set 'LH82' is used in the EULAG model (e.g. Smolarkiewicz and Prusa, 2005). This study extends those of Baldauf (2011) by considering additionally the anelastic equation set of Durran (1989) ('D89') and by comparing different versions (3D, 2D) of the divergence damping, too. The basic methodology again follows the normal mode analysis of Davies et al. (2003).

7.2 Derivation of the dispersion relations

In the following a steady atmosphere (no base flow $u_0 = 0$) is assumed for the base state. It is further hydrostatic ($\partial p_0/\partial z = -g\rho_0$) and fulfills the ideal gas law $p_0 = \rho_0 R T_0$. The sound velocity of the base state is $c_s = \sqrt{\frac{c_p}{c_v} R T_0}$.

We will use an equation for the pressure perturbation p' as in the COSMO-model, but a continuity equation to have a direct control about the anelastic approximations. The different anelastic equation sets are summarized e.g. in Nance and Durran (1994) and are therefore

not repeated here The linearization around the base state delivers

$$\frac{\partial u'}{\partial t} = -\frac{1}{\rho_0}\frac{\partial p'}{\partial x} + fv' + \alpha_D\frac{\partial D'}{\partial x}, \tag{16}$$

$$\frac{\partial v'}{\partial t} = -\frac{1}{\rho_0}\frac{\partial p'}{\partial y} - fu' + \alpha_D\frac{\partial D'}{\partial y}, \tag{17}$$

$$\frac{\partial w'}{\partial t} = -\frac{1}{\rho_0}\frac{\partial p'}{\partial z} - \sigma_{LH}\frac{1}{\rho_0}\frac{N^2}{g}p' - g\frac{\rho'}{\rho_0} + \alpha_{D,v}\frac{\partial D'}{\partial z} + \sigma_{dd2}\alpha_{D,v}D'\frac{1}{\rho_0}\frac{\partial \rho_0}{\partial z}, \tag{18}$$

$$\sigma_2\frac{\partial \rho'}{\partial t} + w'\frac{\partial \rho_0}{\partial z} = -\rho_0 D' - \sigma_{D89}\frac{\rho_0}{\Theta_0}\frac{\partial \Theta_0}{\partial z}w', \tag{19}$$

$$\underbrace{\frac{\partial p'}{\partial t} + w'\frac{\partial p_0}{\partial z}}_{=-g\rho_0 w'} = c_s^2\left(\frac{\partial \rho'}{\partial t} + w'\frac{\partial \rho_0}{\partial z}\right), \tag{20}$$

$$D' = \frac{\partial u'}{\partial x} + \frac{\partial v'}{\partial y} + \frac{\partial w'}{\partial z}. \tag{21}$$

Some switches $\sigma_{...}$ have been introduced whose values (0 or 1) are summarized in table 11. σ_{dd2} distinguishes two types of the artificial divergence damping in the 3D case: either the term $\alpha_D\partial D'/\partial z$ ('type 1', $\sigma_{dd2} = 0$) or the term $\alpha_D/\rho_0\partial(\rho_0 D')/\partial z$ ('type 2', $\sigma_{dd2} = 1$). Type 2 is used in COSMO and MM5 because it can be coded more efficiently than type 1. σ_2 is the main switch of the anelastic approximation. The additional term $\sim \sigma_{LH}$ only arises in the equation system of LH82. For its derivation one has to consider that LH82 are using $-c_p\nabla\Theta_0\pi' + \mathbf{g}\Theta'/\Theta_0$ for the pressure gradient and the buoyancy term instead of the correct term $-c_p\Theta\nabla\pi' + \mathbf{g}\Theta'/\Theta_0$ (Nance and Durran, 1994). In linear approximation the difference between these two terms is $-c_p\pi'\nabla\Theta_0$. Expressed by the variables used in the equation system above this can be approximated linearly by $-\frac{1}{\rho_0}\frac{N^2}{g}p'$. Alternatively, the D89 equation set uses $\nabla\cdot\rho_0\Theta_0\mathbf{v} = 0$ (for adiabatic processes) instead of $\nabla\cdot\rho_0\mathbf{v} = 0$ (used in OP62, WO72 and LH82). In linear approximation this delivers an additional term $\sim \sigma_{D89}$. The pressure equation is just the linearized adiabatic state equation $d\Theta/dt = 0$ which is used by all equation sets considered here. Furthermore, it should be mentioned that in this *linear* analysis there is no difference between the equation systems of OP62 and WO72.

equation system	σ_2	σ_{LH}	σ_{D89}	α_D	$\alpha_{D,v}$	σ_{dd2}
compressible	1	0	0	0	0	0
compressible, with 3D-div. damping, type 1	1	0	0	$\neq 0$	$= \alpha_D$	0
compressible, with 3D-div. damping, type 2	1	0	0	$\neq 0$	$= \alpha_D$	1
compressible, with 2D-div. damping	1	0	0	$\neq 0$	0	0
anelastic (OP62, WO72)	0	0	0	0	0	0
anelastic (LH82)	0	1	0	0	0	0
anelastic (D89)	0	0	1	0	0	0

Table 11: Switches for the different equation sets inspected in the normal mode analysis.

The coefficient functions of the linearized equations (16)-(21) are dependent on z. To reduce this z-dependency (the following Fourier transformation requires even constant coefficients) we perform a variable transformation by a function of the density according to Bretherton (1966, section 5):

$$\phi' = \left(\frac{\rho_0}{\rho_s}\right)^\alpha \cdot \phi_b. \tag{22}$$

where ρ_s is a constant reference value (e.g. at the bottom). The exponent is $\alpha = -1/2$ for the variables $\phi' = u$, v, w, T' and $\alpha = +1/2$ for $\phi' = p'$, ρ'. Insertion into eqns. (16)-(21) results in a quite similar system with additional terms proportional to the (inverse) scale height

$$\delta = -\frac{\partial}{\partial z}\left(\log\frac{\rho_0}{\rho_s}\right). \tag{23}$$

In the special case of an isothermal atmosphere ($T_0 = const.$) the density is purely exponential and therefore $\delta = g/(RT_0) = const.$ The result of this Bretherton transformation is that some coefficients (namely those $\sim 1/\rho_s$) become constant, whereas others like $\sim c_s^2$, $\sim T_0$, $\sim \delta$ remain dependent on z (they are only constant for an isothermal atmosphere). But this z-dependency is quite weak, therefore they can also be considered nearly as constant. This allows to extent the analysis to more realistic stratifications (see 'second stratification case' below).

It is convenient to introduce the acoustic cutoff frequency

$$\omega_a^2 = -\frac{g}{\rho_0}\frac{\partial\rho_0}{\partial z} \tag{24}$$

and therefore $\delta = \omega_a^2/g$, and the Brunt-Väisälä-frequency

$$N^2 = \frac{g}{\Theta_0}\frac{\partial\Theta_0}{\partial z} = \frac{g}{T_0}\left(\frac{\partial T_0}{\partial z} + \frac{g}{c_p}\right). \tag{25}$$

With the aid of the sound velocity, the ideal gas equation and the hydrostatic equation one can derive

$$\omega_a^2 = N^2 + \frac{g^2}{c_s^2}. \tag{26}$$

Now we can Fourier transform the equations by

$$\phi_b'(x,y,z,t) = \hat{\phi}_b(k_x,k_y,k_z,\omega)\,e^{i(k_x x + k_y y + k_z z - \omega t)}. \tag{27}$$

This leads to a system of the form $\mathbf{A}\cdot(\hat{u}_b,\hat{v}_b,\hat{w}_b,\hat{\rho}_b,\hat{p}_b)^T = 0$ with

$$\mathbf{A} = \begin{pmatrix} i\omega + \alpha_D(ik_x)^2 & f - \alpha_D k_x k_y & \alpha_D ik_x(ik_z + \frac{\delta}{2}) & 0 & -ik_x\frac{1}{\rho_s} \\ -f - \alpha_D k_x k_y & i\omega + \alpha_D(ik_y)^2 & \alpha_D ik_y(ik_z + \frac{\delta}{2}) & 0 & -ik_y\frac{1}{\rho_s} \\ \alpha_{D,v}ik_x K_d & \alpha_{D,v}ik_y K_d & i\omega + \alpha_{D,v}(ik_z + \frac{\delta}{2})K_d & -\frac{g}{\rho_s} & A_{35} \\ -ik_x\rho_s & -ik_y\rho_s & A_{43} & \sigma_2 i\omega & 0 \\ 0 & 0 & -\frac{\rho_s}{g}N^2 c_s^2 & -i\omega c_s^2 & i\omega \end{pmatrix} \tag{28}$$

and with the abbreviations

$$K_d = \left(ik_z + \frac{\delta}{2} - \sigma_{dd2}\frac{\omega_a^2}{g}\right), \tag{29}$$

$$A_{35} = -\frac{1}{\rho_s}\left(ik_z - \frac{\delta}{2}\right) - \sigma_{LH}\frac{1}{\rho_s}\frac{N^2}{g}, \tag{30}$$

$$A_{43} = -\rho_s(ik_z + \frac{\delta}{2}) + \rho_s\frac{\omega_a^2}{g} - \sigma_{D89}\rho_s\frac{N^2}{g}. \tag{31}$$

After an appropriate non-dimensionalization the requirement $\det A = 0$ leads to the characteristic equation for $\omega(\mathbf{k})$. This delivers the following dispersion relations:

The characteristic equation for the **non-hydrostatic, compressible equations** follows from the switches $\sigma_2 = 1$, $\sigma_{LH} = 0$, $\sigma_{D89} = 0$:

$$
\omega^4 + \left[i\alpha_D(k_x^2 + k_y^2) + i\alpha_{D,v}\left(k_z - \frac{i}{2}\frac{\omega_a^2}{g}\right)^2 - \sigma_{dd2}\alpha_{D,v}\left(k_z - \frac{i}{2}\frac{\omega_a^2}{g}\right)\frac{\omega_a^2}{g} \right] \omega^3
$$
$$
- \left[c_s^2\left(k^2 + \frac{1}{4}\frac{\omega_a^4}{g^2}\right) + f^2 \right] \omega^2
$$
$$
+ \left[(k_x^2 + k_y^2)(\alpha_D - \alpha_{D,v})g\left(k_z - \frac{i}{2}\frac{\omega_a^2}{g}\right) - i\alpha_{D,v}f^2\left(k_z - \frac{i}{2}\frac{\omega_a^2}{g}\right)^2 \right.
$$
$$
\left. + \sigma_{dd2}\alpha_{D,v}\left(-i(k_x^2 + k_y^2)\omega_a^2 + f^2\left(k_z - \frac{i}{2}\frac{\omega_a^2}{g}\right)\frac{\omega_a^2}{g}\right) \right] \omega
$$
$$
+ N^2 c_s^2 (k_x^2 + k_y^2) + f^2 c_s^2\left(k_z^2 + \frac{1}{4}\frac{\omega_a^4}{g^2}\right) = 0.
\tag{32}
$$

For $\alpha_D = 0$ and $\alpha_{D,v} = 0$ we get the compressible solution (i.e. the 'true' solution), whereas the influence of the artificial divergence damping can be inspected by $\alpha_D, \alpha_{D,v} \neq 0$. Note, that this dispersion relation is identical to equations (15) and (18) of Gassmann and Herzog (2007), if the simplifications $f = 0$ and $\sigma_{dd2} = 0$ are made.

The different **anelastic approximations** follow from $\sigma_2 = 0$, $\alpha_D = \alpha_{D,v} = 0$ and the setting of the switches σ_{LH} and σ_{D89} (see table 11). This results in the dispersion relation

$$
\left[c_s^2\left(k^2 + \frac{1}{4}\frac{\omega_a^2}{g}\right) + a_0 \right] \omega^2 - \left[c_s^2(k_x^2 + k_y^2)N^2 + f^2\left(c_s^2\left(k_z^2 + \frac{1}{4}\frac{\omega_a^2}{g}\right) + a_0\right) \right] = 0
\tag{33}
$$

with

$$
a_0 = \begin{cases} \frac{N^2 c^2}{g}\left(ik_z - \frac{1}{2}\frac{\omega_a^2}{g}\right) & \text{for OP62, WO72,} \\ 0 & \text{for LH82,} \\ -N^2 & \text{for D89.} \end{cases}
\tag{34}
$$

All the anelastic approximations eliminates sound waves, only the two branches for gravity waves are contained.

In the following sections, we will evaluate and compare the dispersion relations (32) and (33) for several realistic parameters.

7.3   Discussion of the results

To get an impression about the behavior of waves we consider two stratifications. First an isothermal atmosphere with $T_0 = 260$ K. In this case the inverse scale height is $\delta \approx 1/7606.5$ 1/m, the sound velocity is $c_s \approx 323.2$ m/s, the Brunt-Väisälä-frequency is $N \approx 0.01919$ 1/s, and the acoustic cut-off frequency is $\omega_a \approx 0.03591$ 1/s. The second considered atmosphere also has a mean temperature of $T_0 = 260$ K but a Brunt-Väisälä frequency of $N = 0.01$ 1/s. We further consider wave expansion both in pure horizontal direction or in a direction which is tilted by 20 degrees against the horizontal.

For the compressible equations *with* divergence damping we choose values of $\alpha_D, \alpha_{D,v} = 50000$, 100000, or 150000 m^2/s, which are typical values for COSMO grid mesh sizes from about 2.8 km until about 10 km, respectively.
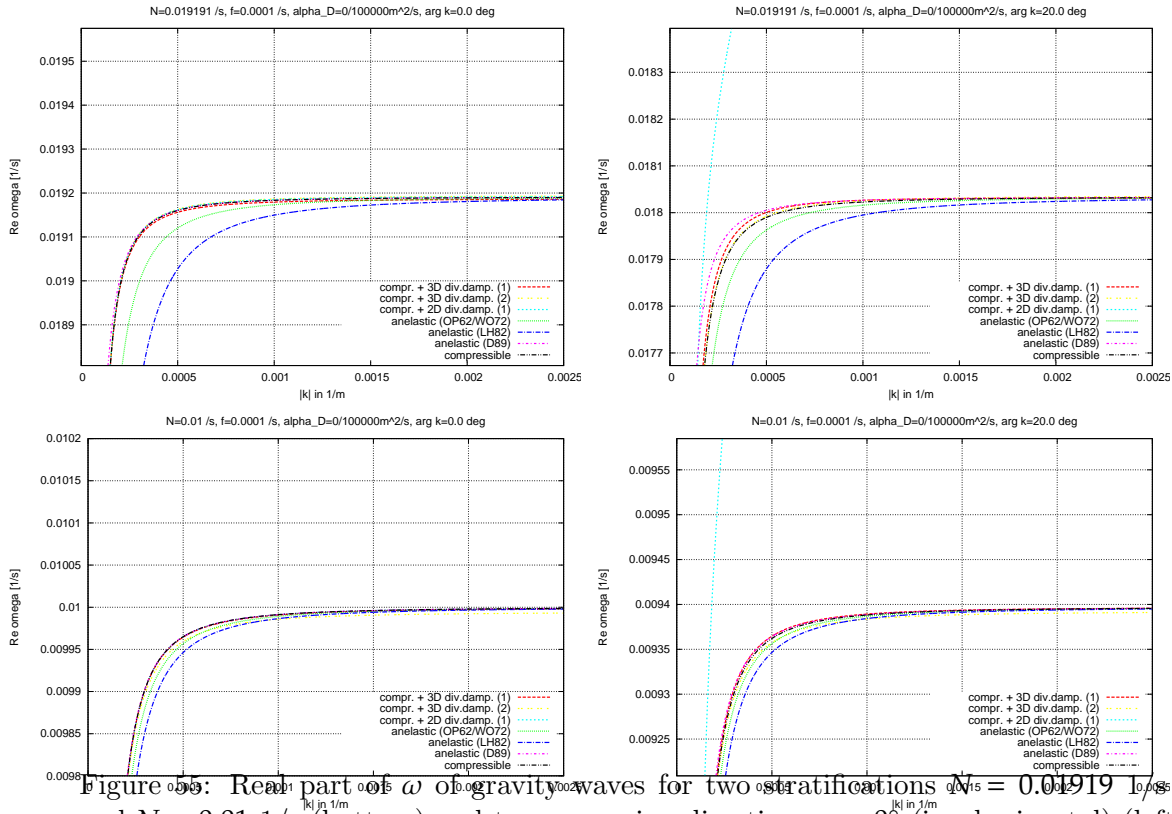
Figure 55: Real part of ω of gravity waves for two stratifications $N = 0.01919$ 1/s (top) and $N = 0.01$ 1/s (bottom) and two expansion directions $\alpha = 0°$ (i.e. horizontal) (left) and $\alpha = 20°$ (right). The different equation sets are distinguished by different colors and line types (see also table 11).

Short gravity waves. Figure 55 shows the positive real part of the gravity for the different equation sets. For very short gravity waves ($k = 0.003$ 1/m corresponds to a wavelength $\lambda = 2\pi/k \approx 2.1$ km) all equation sets show a quite good agreement with the 'truth', the dispersion relation of the compressible equations (black line). A closer examination shows that for the anelastic equation sets it holds indeed that $\omega \to \pm N$ for $k \to \infty$. The compressible 3D divergence damping versions do not exactly converge to the right value but the deviations are less than about 0.05 % and therefore are negligible. The 2D divergence damping has a quite strange behavior for tilted expansion, which is separately discussed below.

For longer waves (> 10 km) stronger deviations in the order of one percent are visible for the OP62 and WO72 system and even stronger for the LH82 system. In contrast, a remarkably good agreement with the compressible system is shown by the D89 equation set. The compressible sets *with* 3D-divergence damping are generally quite close to the compressible solution.
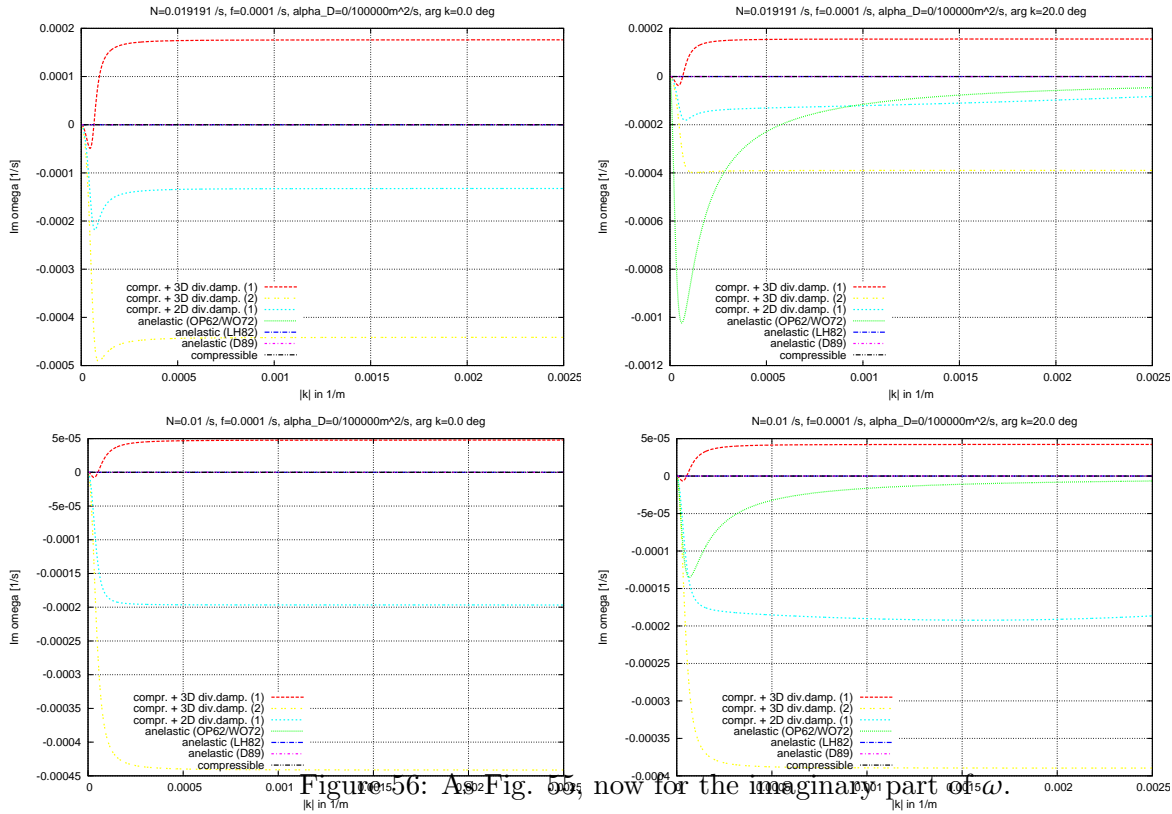
Figure 56: As Fig. 55, now for the imaginary part of ω.

The damping (i.e. the imaginary part of ω) is shown in Figure 56. The horizontal expansion of all anelastic sets has no damping. The same holds for tilted expansion in the cases LH82 and D89, however OP62 or WO72 show a certain damping for longer gravity waves. The compressible equations with 3D divergence damping type 2 show a damping of nearly all gravity waves. This is smaller for the 2D divergence damping. In contrast, type 1 even shows a weak amplification. This was also stated in Baldauf (2010, appendix), were it has been shown, too, that this behavior does not occur if the Bretherton-transformation is not performed.

Long gravity waves. The long gravity wave behavior is shown in Fig. 57 ($k = 0.0001\ 1/\text{m}$ corresponds to $\lambda \approx 63$ km). Obviously divergence damping has almost no influence to this wave type. The OP62 and WO72 systems are still relatively close to the compressible equations for wave lengths larger around 100 km. For even larger wave lengths the deviations become larger. A different behavior has LH82: here an intermediate range of long gravity waves show a larger deviation from the compressible solution, however, very long gravity waves ($\lambda > 300$ km) are well represented. Under all anelastic approximations considered here, such very long waves are worst represented by the D89 system. All these statements reduce in strength if the stratification becomes less stable. (lower figures in Fig. 57).

For the damping of long waves (Figs. 58) similar statements hold as for the shorter waves. For extremely long waves the influence of divergence damping decreases with increasing wave length.
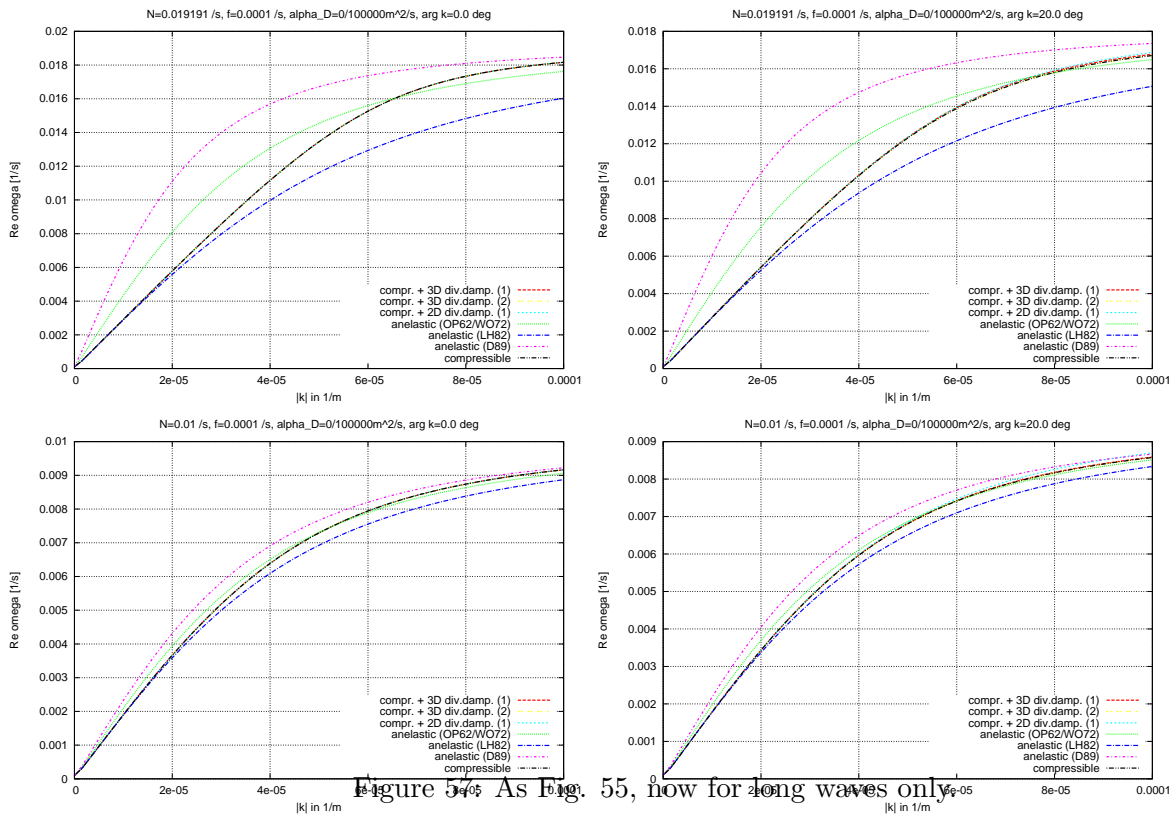
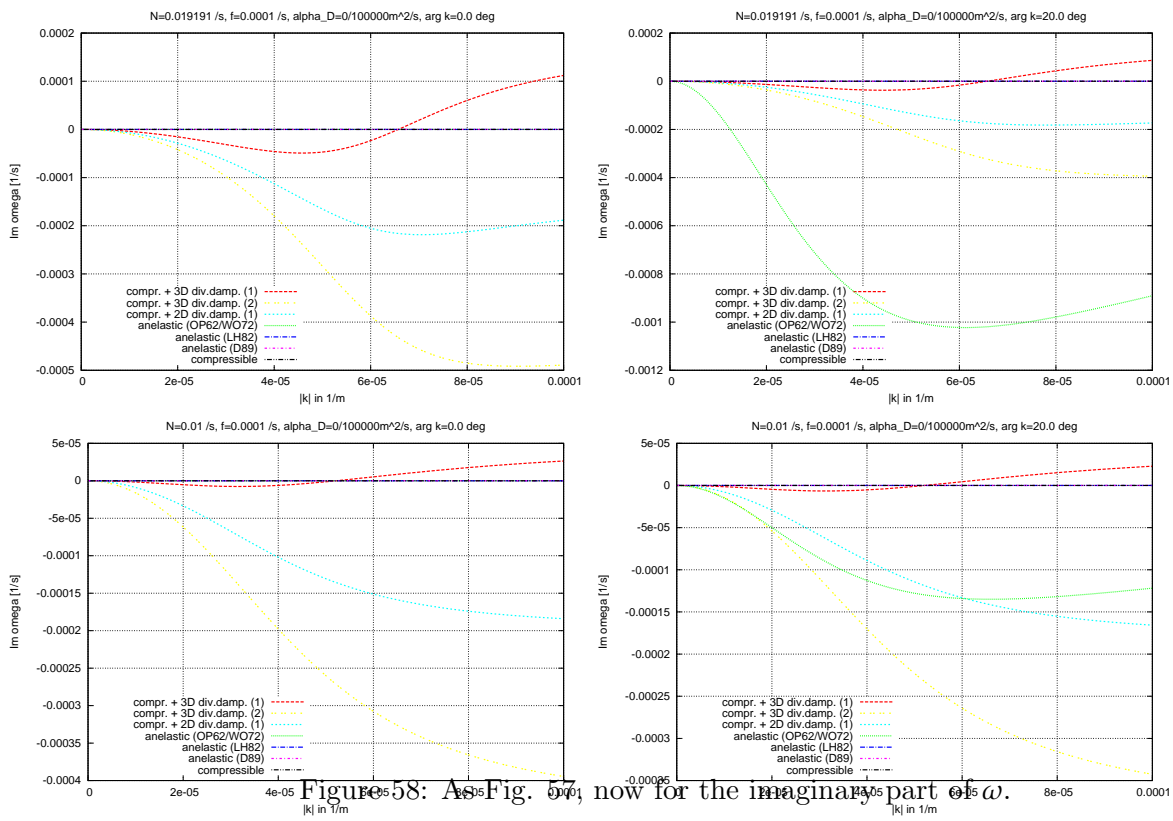Figure 57: As Fig. 55, now for long waves only.

Figure 58: As Fig. 57, now for the imaginary part of ω.

Sound waves in the compressible systems.   The compressible equations contain sound waves. The divergence damping increasingly reduces their phase velocity with decreasing wave length (Figure 59). However, for strong divergence damping the e-folding time is quite small, therefore only long sound waves will be simulated in the current COSMO dynamical core. In the case of tilted expansion (Figure 60), there is a small but relatively unimportant difference between the different types of divergence damping.

The temperature stratification has almost no influence to the expansion of sound waves. Therefore only results for $N = 0.01$ 1/s are shown.

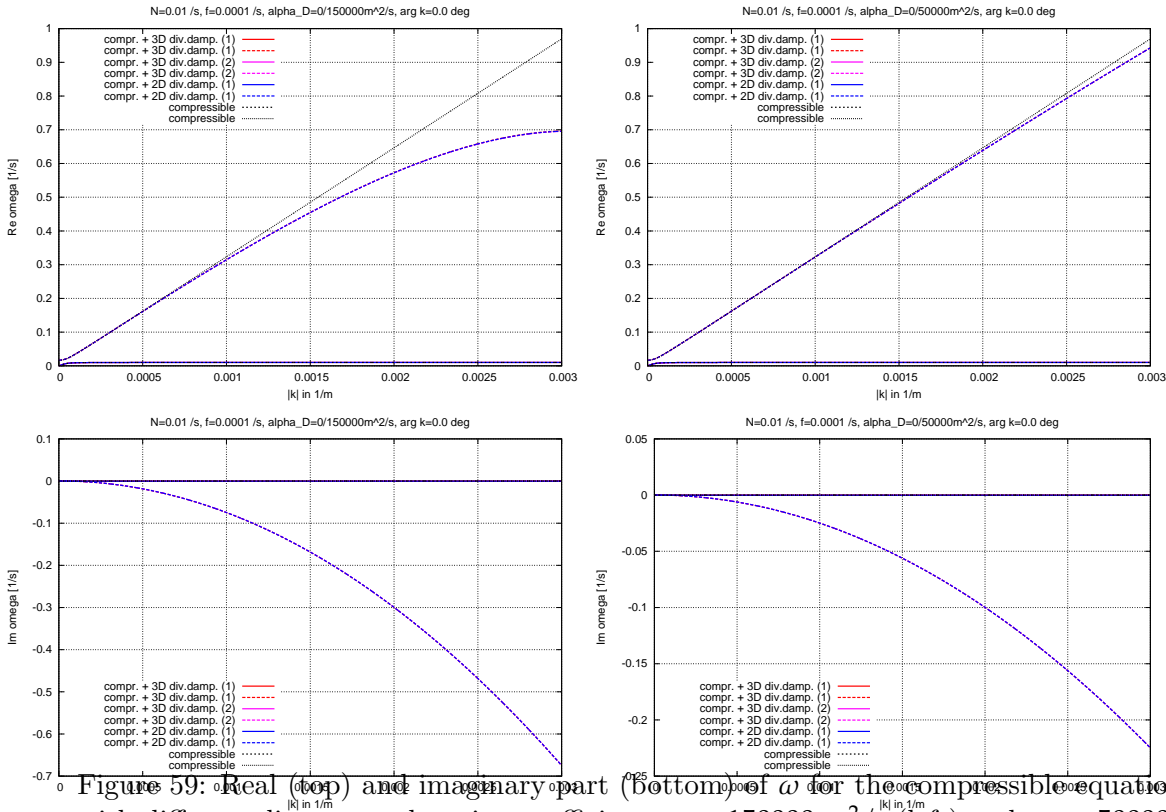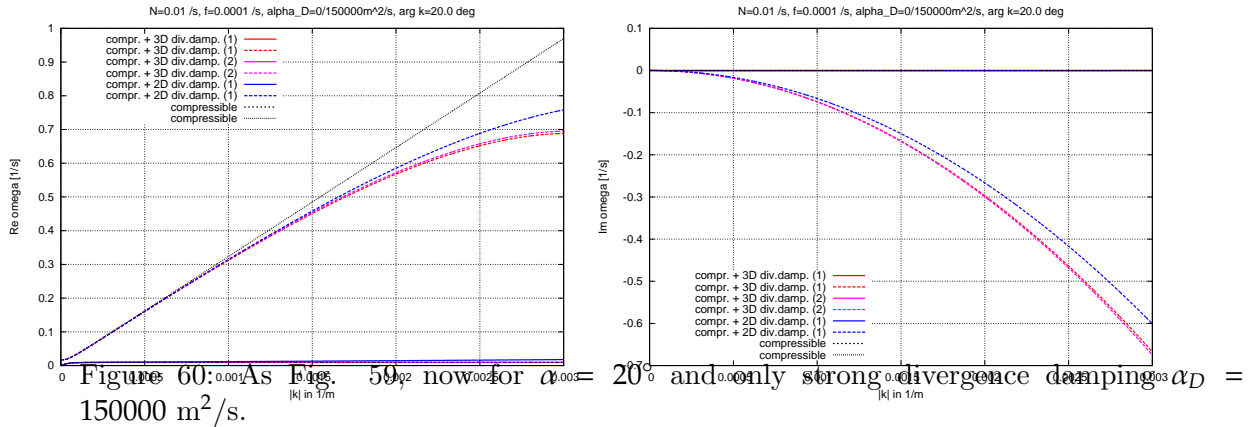Figure 59: Real (top) and imaginary part (bottom) of ω for the compressible equation sets with different divergence damping coefficient $\alpha_D = 150000$ m^2/s (left) and $\alpha_D = 50000$ m^2/s (right). $N = 0.01$ 1/s, $\alpha = 0°$.

Figure 60: As Fig. 59, now for $\alpha = 20°$ and only strong divergence damping $\alpha_D = 150000$ m^2/s.

Gravity waves in the compressible systems. In a section above we have already seen that the gravity waves are almost correctly treated by the 3D divergence damping. For the 2D divergence damping, this also holds only for purely horizontal expansion of gravity waves, whereas it shows a strange behavior for tilted expansion: the frequency obviously increases with decreasing wavelength instead of remaining constant. This behavior was already remarked by (Gassmann and Herzog, 2007, eq. (20)). Since in real case simulations and also in idealized tests this equation system behaves not so bad, a look to all the branches of the dispersion relation is advisable. Figure 61 shows that the positive frequencies ω are increasing with k. But the absolute values of the negative frequencies are *decreasing*. Physically this means that upward traveling gravity waves are faster then expected, whereas downward traveling gravity waves are slower than expected, so that their mean velocity is nearly the correct one.

Figure 61: As Figure 60, only gravity waves.
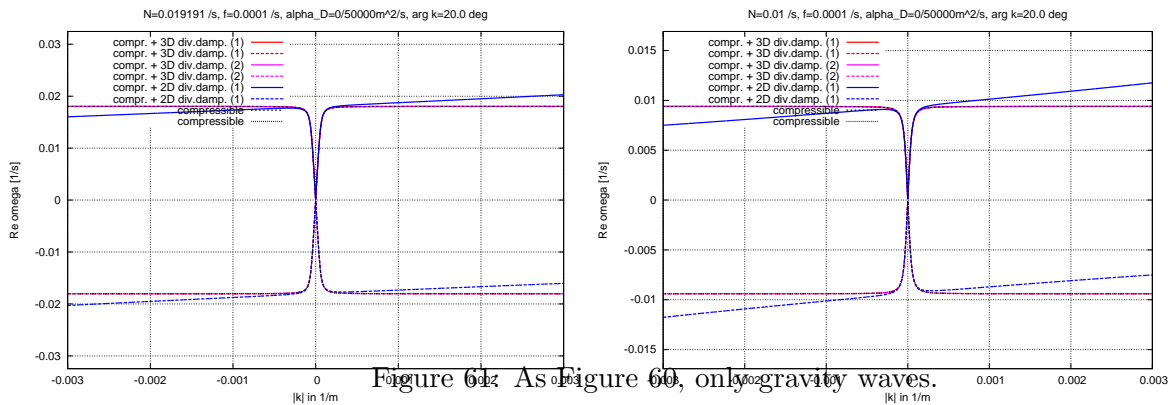
7.4   Summary

The dispersion relations for several anelastic equation sets and compressible equations with several versions of the artificial divergence damping have been compared.

The general outcome is that the anelastic equation set is very well suited to simulate shorter gravity waves. The compressible systems with 'type 2' 3D-divergence damping treats the phase and group velocity of this wave type well, too, apart from a small damping. But

the 2D divergence damping, which is actually used in the COSMO model, exhibits a not completely satisfying behavior.

Concerning long gravity waves ($\lambda > 100$ km), the anelastic equation sets have some drawbacks. This probably reduces their applicability for global models a bit.

Sound waves are of course not contained in the anelastic equations, but also the shorter waves are heavily damped in the compressible equations by divergence damping. Only for rather long sound waves a reasonable realistic treatment can be expected.

References

Baldauf, M., 2010: Linear stability analysis of Runge-Kutta based partial time-splitting schemes for the Euler equations. *Mon. Wea. Rev.*, **138**, 4475–4496.

Baldauf, M., 2011: Non-hydrostatic modelling with the COSMO model. *ECMWF Workshop on Non-hydrostatic Modelling.*

Bretherton, F. P., 1966: The propagation of Groups of Internal Gravity Waves in a Shear Flow. *Quart. J. Roy. Met. Soc.*, **92**, 466–480.

Davies, T., A. Staniforth, N. Wood, and J. Thuburn, 2003: Validity of anelastic and other equation sets as inferred from normal-mode analysis. *Quart. J. Roy. Met. Soc.*, **129**, 2761–2775.

Durran, D. R., 1989: Improving the Anelastic Approximation. *J. Atmos. Sci.*, **46 (11)**, 1453.

Gassmann, A. and H.-J. Herzog, 2007: A Consistent Time-Split Numerical Scheme Applied to the Nonhydrostatic Compressible Equations. *Mon. Wea. Rev.*, **135**, 20–36.

Lipps, F. B. and R. S. Hemler, 1982: A scale-analysis of deep moist convection and some related numerical calculations. *J. Atmos. Sci.*, **39**, 2192–2210.

Nance, L. B. and D. R. Durran, 1994: A Comparison of the Accuracy of Three Anelastic Systems and the Pseudo-Incompressible System. *JAS*, **52 (24)**, 3549–3565.

Ogura, Y. and N. A. Phillips, 1962: Scale analysis of deep and shallow convection in the atmosphere. *J. Atmos. Sci.*, **19**, 173.

Smolarkiewicz, P. K. and J. M. Prusa, 2005: Towards mesh adaptivity for geophysical turbulence: continuous mapping approach. *Int. J. Numer. Meth. Fluids*, **47**, 789–801.

Wicker, L. J. and W. C. Skamarock, 2002: Time Splitting Methods for Elastic Models using Forward Time Schemes. *Mon. Wea. Rev.*, **130**, 2088–2097.

Wilhelmson, R. and Y. Ogura, 1972: The pressure perturbation and the numerical modeling of a cloud. *J. Atmos. Sci.*, **29**, 1295–1307.

8   The finite volume implicit solver CONSOL

Pier Luigi Vitagliano

CMCC, Centro Euro-Mediterraneo sui Cambiamenti Climatici

CIRA, Centro Italiano Ricerche Aerospaziali

Via Maiorise, 80143 Capua (CE), Italy

Summary

A flow solver for the Euler and Navier-Stokes equations in 3 dimensions has been written. Time integration is based on dual time stepping, spatial discretization on finite volumes. Second order central scheme with added artificial dissipation and fourth order scheme have been currently implemented. Convergence in dual time is improved by adopting residual averaging, local time stepping, preconditioning, multigrid. Tests with complex orography were carried out, they are meant to address the issues related with flow initialization, hydrostatic balance in the equations, inflow, outflow and upper boundary conditions. Some other test cases are reported, to demonstrate the capability of the present method to dial with typical basic phenomena.

8.1   Introduction

The general trend in numerical weather prediction is to increase the mesh resolution; consequences are the increase in amount of mesh cells, reduction of time step and steeper lower boundaries in regions with complex orography. In those regions mesh cells are more skewed, so horizontal and vertical components of velocity and pressure gradient (and numerical errors as well) are more strongly coupled.

Motivations for this work are the needs of improving numerical efficiency of the COSMO model, improving the conservation properties of the scheme and its capability to deal with steep orography.

Finite volume formulation has the capability of conserving the transported quantities, for this reason it is a good candidate for improving the conservation properties of the dynamical core. The dual time stepping procedure is very popular in the field of aerodynamics but it seems that was never tested for simulation of atmospheric flows. The aim of this work is to evaluate the performances of the scheme in comparison with the classical time splitting procedure, which is the standard time integration scheme of COSMO, in the perspective of using very small grid size and also very large time steps, those are required for climatological simulations. The main questions to answer are related to three aspects: equation set in conservative variables, the dual time stepping procedure and the finite volume schemes, whether they are suitable for numerical weather prediction.

8.2   Mathematical formulation

The unsteady Euler equations are cast in integral form for a region Ω with boundary $\partial\Omega$:

$$\frac{\partial}{\partial t} \int_{\Omega} \underline{\mathbf{W}} \, d\Omega + \oint_{\partial\Omega} \underline{\underline{\mathbf{F}}} \cdot \underline{n} \, dS = \int_{\Omega} \underline{\mathbf{B}} \, dV \qquad (35)$$

when the region Ω is fixed in time the above matrices are:

$$
\underline{\mathbf{W}} = \begin{bmatrix} \rho \\ \rho u \\ \rho v \\ \rho w \\ \rho E \end{bmatrix}, \quad
\underline{\underline{\mathbf{F}}} = \begin{bmatrix} \rho u & \rho v & \rho w \\ \rho u^2 + p & \rho uv & \rho uw \\ \rho uv & \rho v^2 + p & \rho w \\ \rho uw & \rho vw & \rho w^2 + p \\ \rho uH & \rho vH & \rho wH \end{bmatrix}, \quad
\underline{\mathbf{B}} = \begin{bmatrix} 0 \\ 0 \\ 0 \\ \rho g \\ \rho gw \end{bmatrix},
\tag{36}
$$

where $\underline{\mathbf{W}}$ is the vector of conserved quantities, $\underline{\underline{\mathbf{F}}}$ is the corresponding flux term, $\underline{\mathbf{B}}$ the source term, g the vertical component of the gravity vector g (usually the reference system z axis is oriented like -g), $\underline{n}$ is the unit vector normal to the boundary surface and dS is the surface area element. We denote density and pressure as ρ and p, the velocity vector $\underline{\mathbf{u}}=(u,v,w)$. For a perfect gas we can express the pressure from the total energy E

$$
p = (\gamma - 1)\rho(E - \frac{\mathbf{u}^2}{2})
\tag{37}
$$

the total enthalpy is defined by

$$
H = E + \frac{p}{\rho}.
\tag{38}
$$

The integral form allows discontinuities in the flow field.

For computing the Navier-Stokes equations, viscous fluxes $\underline{\underline{\mathbf{G}}}$ are added to $\underline{\underline{\mathbf{F}}}$:

$$
\underline{\underline{\mathbf{G}}} = - \begin{bmatrix} 0 & 0 & 0 \\ \sigma_{xx} & \sigma_{xy} & \sigma_{xz} \\ \sigma_{xy} & \sigma_{yy} & \sigma_{yz} \\ \sigma_{xz} & \sigma_{yz} & \sigma_{zz} \\ \underline{\mathbf{u}} \cdot \sigma_{ix} - \kappa\frac{\partial T}{\partial x} & \underline{\mathbf{u}} \cdot \sigma_{iy} - \kappa\frac{\partial T}{\partial y} & \underline{\mathbf{u}} \cdot \sigma_{iz} - \kappa\frac{\partial T}{\partial z} \end{bmatrix}
\tag{39}
$$

$\underline{\underline{\sigma}}$ is the stress tensor and its components are:

$$
\begin{aligned}
\sigma_{xx} &= \mu[2\frac{\partial u}{\partial x} - \tfrac{2}{3}(\frac{\partial u}{\partial x} + \frac{\partial v}{\partial y} + \frac{\partial w}{\partial z})] \\
\sigma_{xy} &= \mu(\frac{\partial u}{\partial y} + \frac{\partial v}{\partial x})
\end{aligned}
\tag{40}
$$

the other components are obtained by exchanging the velocity gradient derivatives. μ is the kinematic viscosity, the heat flux is given by the thermal diffusion coefficient κ multiplied by the temperature gradient. In case of turbulent fluxes the turbulent viscosity μ_{tur} and turbulent thermal diffusion κ_{tur} are modeled and added to the thermodynamical (laminar) coefficients. Turbulent viscous flows were not simulated in this work.

Boundary conditions are different in case of inflow, outflow and rigid wall. Inflow conditions allow to set four variables and extrapolate one variable from inside the flow field. Usually momentum and density are set, and pressure is extrapolated. Outflow conditions allow to set one variable (usually pressure or normal momentum component) and extrapolate the others. Boundary conditions on rigid walls fix normal momentum component to 0 and extrapolate tangential components and pressure. Artificial dissipation also requires boundary conditions: usually zero artificial fluxes are set at the boundaries. In case of viscous computations all the momentum components at the wall can be set to 0 (no-slip boundary condition), and wall enthalpy or heat flux (enthalpy gradient) can be assigned. In case of inviscid flow the heat flux at the wall could be added as an external source to the ground layer.

8.3   Finite volume scheme and time integration

The equations are discretized by sub-dividing the flow domain in sub-domains (mesh cells), assuming the conserved quantities $\underline{\mathbf{W}}$ are known at the center of each mesh cell. In our case the domain is sub-divided in structured form, which means that each cell is stored in a 3-dimensional array and can be addressed by a 3-d index (i,j,k). Its 6 neighbors can be simply addressed by the indices (i+1,j,k), (i-1,j,k), (i,j-1,k), (i,j+1,k), (i,j,k-1), (i,j,k+1). The structured mesh arrangement allows more efficient algorithms for computing advective and diffusive fluxes, and more efficient data storage, since it is not necessary to keep informations for addressing the neighbor cells. The semi-discretization for a sub-domain of volume V leads to the equation:

$$V\frac{\partial(\underline{\mathbf{W}})}{\partial t} + \underline{\mathbf{R}}(\underline{\mathbf{W}}) = 0 \tag{41}$$

where

$$\underline{\mathbf{R}}(\underline{\mathbf{W}}) = \underline{\mathbf{Q}} - \underline{\mathbf{D}} - \underline{\mathbf{B}}. \tag{42}$$

$\underline{\mathbf{R}}$ represents the sum of the net flux out of the sub-domain $\underline{\mathbf{Q}}$, the artificial dissipative flux $-\underline{\mathbf{D}}$ (that is required for numerical stability) and the source term $-\underline{\mathbf{B}}$, which are balanced by the rate of change of $\underline{\mathbf{W}}$. The net flux out of the cell m is given by the sum over the six cell faces k

$$\mathbf{Q}_{\mathrm{m}} = \sum_{\mathrm{k}=1}^{6} \underline{\underline{\mathbf{F}}}_{\mathrm{mk}} \cdot \underline{n} S_{\mathrm{mk}} \tag{43}$$

Fluxes $\underline{\underline{\mathbf{F}}}$ are approximated at the cell face centers by averaging the quantities between the cell m and its neighbors k,

$$\underline{\underline{\mathbf{F}}}_{\mathrm{mk}} = \frac{\underline{\underline{\mathbf{F}}}_{\mathrm{m}} + \underline{\underline{\mathbf{F}}}_{\mathrm{k}}}{2} \tag{44}$$

S_{mk} is the area of the face between cells m and k, and $\underline{n}$ the unit vector normal to the cell face pointing outward. The artificial dissipation $\underline{\mathbf{D}}$ is proportional to the fourth derivative of the conserved variables:

$$\underline{\mathbf{D}} = \nu\nabla^4(\underline{\mathbf{W}}). \tag{45}$$

It can be expressed in flux form as the sum of the third derivative over the cell faces, in order to keep the conservation properties of the scheme.

Time derivatives are discretized by a second order backward formula, where the upper index n indicates the current time step. Volume for our system is constant in time and can be taken out of the time derivative:

$$\frac{\partial(\underline{\mathbf{W}})}{\partial t} = \frac{3\underline{\mathbf{W}}^{n+1} - 4\underline{\mathbf{W}}^n + \underline{\mathbf{W}}^{n-1}}{2\Delta t} \tag{46}$$

This formula is implicit, as it contains the variables $\underline{\mathbf{W}}$ at the time step n+1. It is A-stable and damps the highest frequency. In principle there are no limitations to Δt due to numerical stability. The dual time stepping procedure (Jameson, 1992) consists in solving the following system by inner iterations which advance in pseudo-time τ to steady state:

$$\frac{\partial(\underline{\mathbf{W}}^{n+1})}{\partial \tau} + \underline{\mathbf{R}}^*(\underline{W}^{n+1}) = 0 \tag{47}$$

where

$$\underline{\mathbf{R}}^*(\underline{W}^{n+1}) = \frac{3\underline{\mathbf{W}}^{n+1} - 4\underline{\mathbf{W}}^n + \underline{\mathbf{W}}^{n-1}}{2\Delta t} + \underline{\mathbf{R}}(\underline{W}^{n+1}) \tag{48}$$

An explicit multistage Runge-Kutta time marching scheme with variable local $\Delta\tau$, residual averaging, preconditioning and multigrid is implemented to advance the system in dual time, until a norm of the dual time derivative is smaller than a given small value. It should be noted that the backward implicit time derivative is second order accurate only when the residuals of the dual time equations are driven to 0. A technique based on prediction can be adopted, in order to keep the second order accuracy also in case of non perfect convergence of the dual time iterations: the flow variables are initialized at the beginning of the dual time iterations by an appropriate prediction formula, second order accurate in time. It has been shown that the dual time iterations do not destroy the second order accuracy of the prediction formula.

The convergence rate of iterative solvers for compressible Euler or Navier-Stokes equations is limited in case of low Mach number flows, because of the large difference between the velocities of the advective fluxes and the pressure perturbations (acoustic waves). Usual technique is to modify the acoustic speed in order to make the local Mach number large enough almost everywhere in the flow domain. It has essentially two functions: the first one is to improve the convergence rate, the second one is to modify the relative influence of the artificial dissipation term, which would affect the physical solution for very small Mach numbers. The basic idea is to pre-multiply the time derivatives of the flow variables (without artificial dissipation) by an appropriate matrix, which performs the scaling of the acoustic speeds with respect to the flux velocities. More details are in Turkel et al. (1996). Preconditioning can only be applied when we are interested to obtain a steady solution, since it destroys the time accuracy of the governing equations. In our procedure the physical time derivatives are treated as source terms and they are concealed in the right hand side of the equations set, while the dual time derivatives are relaxation terms.

8.4   Atmosphere at rest

The test case with atmosphere at rest (i.e. zero velocity components and no fluxes from the boundaries) is useful to highlight the numerical issues related to the large vertical gradient of pressure and density in case of a deformed mesh. Discretization errors in the computation of the pressure gradient for tilted cells can produce non-zero horizontal components. Even the little displacement of a single mesh point in the interior of a perfectly regular rectangular mesh on flat orography can produce spurious velocity and disturbances in the flow solutions. When pressure is a function only of the vertical coordinate z, a density field exists that allows a steady solution with zero velocity. But the spatial discretization of the pressure gradient is affected by metric terms. The discrete Euler flow equations for a cell m in case of atmosphere at rest simplify to:

$$\frac{\partial \rho}{\partial t} = 0 \tag{49}$$

$$\frac{\partial \rho u}{\partial t} + \frac{1}{V}\sum_{k=1}^{6} p_{mk} n_x S_{mk} = 0 \tag{50}$$

$$\frac{\partial \rho v}{\partial t} + \frac{1}{V}\sum_{k=1}^{6} p_{mk} n_y S_{mk} = 0 \tag{51}$$

$$\frac{\partial \rho w}{\partial t} + \frac{1}{V}\sum_{k=1}^{6} p_{mk} n_z S_{mk} = \rho g \tag{52}$$

$$\frac{\partial \rho E}{\partial t} = 0 \tag{53}$$

p_{mk} is the pressure averaged at the face between the cells m and k:

$$p_{\mathrm{mk}} = \frac{p_{\mathrm{m}} + p_{\mathrm{k}}}{2} \tag{54}$$

n_x, n_y, n_z are the Cartesian components of the unit vector normal to the face, S_{mk} is the face area. The set of discrete equations in case of zero velocity is a system of $3N_c$ linear equations in $2N_c$ unknowns p, ρ, constant in time, where N_c is the total amount of mesh cells. So it is not possible to find discrete solution for the atmosphere at rest with generic 3 dimensional meshes: only additional constraints on mesh coordinates could allow a solution for the equilibrium of the horizontal pressure gradient components. The resulting horizontal accelerations produce spurious motions.

A reference pressure and density field p_{ref}, ρ_{ref} in hydrostatic equilibrium is subtracted from the momentum equation to reduce the amount of spurious accelerations. By assuming that:

$$\nabla p_{\mathrm{ref}} = \rho_{\mathrm{ref}} g \tag{55}$$

$$p' = p - p_{\mathrm{ref}} \tag{56}$$

$$\rho' = \rho - \rho_{\mathrm{ref}} \tag{57}$$

the momentum equations in discrete form can be written as follows:

$$\frac{\partial \rho u}{\partial t} + \frac{1}{V} \sum_{k=1}^{6} p'_{\mathrm{mk}} n_x S_{\mathrm{mk}} = 0 \tag{58}$$

$$\frac{\partial \rho v}{\partial t} + \frac{1}{V} \sum_{k=1}^{6} p'_{\mathrm{mk}} n_y S_{\mathrm{mk}} = 0 \tag{59}$$

$$\frac{\partial \rho w}{\partial t} + \frac{1}{V} \sum_{k=1}^{6} p'_{\mathrm{mk}} n_z S_{\mathrm{mk}} = \rho' g \tag{60}$$

Since the pressure perturbation $p\prime$ is usually 10 to 100 times smaller than full pressure, the spurious acceleration is also smaller. Pressure and density perturbations are adopted for computing the artificial dissipation terms. In order to evaluate the performances of the numerical scheme, a skewed mesh was produced on a simplified orography with highest mountain of 3 km (Fig. 62). The mesh contains 150 cells in horizontal direction and 160 in vertical direction, with $\Delta x = 1$ km and $\Delta z = 125$ m. The mesh levels are flat above 13.5 km.
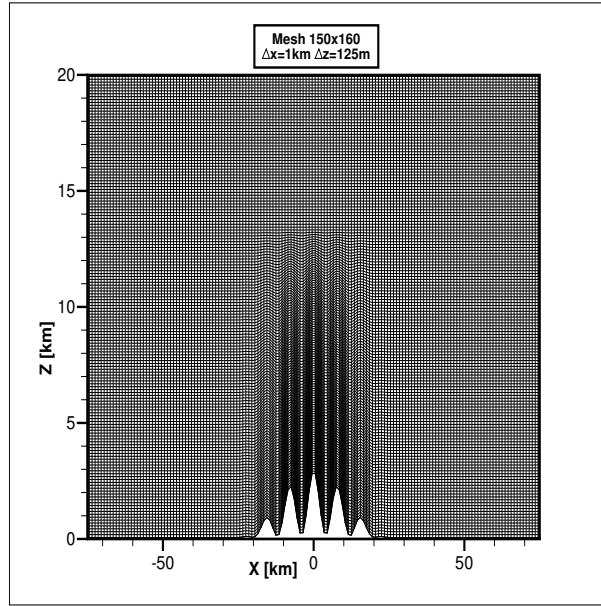
Figure 62: Mesh for testing the atmosphere at rest

The reference pressure and density field is defined with constant Brunt-Väisälä frequency N_{BV}=0.01 1/s, and the initial field is defined with N_{BV}=0.015 1/s, so the initial pressure and density perturbations are computed as the difference between the two fields (Fig. 63). The flow field computed after 90000 seconds is shown in Fig. 64.
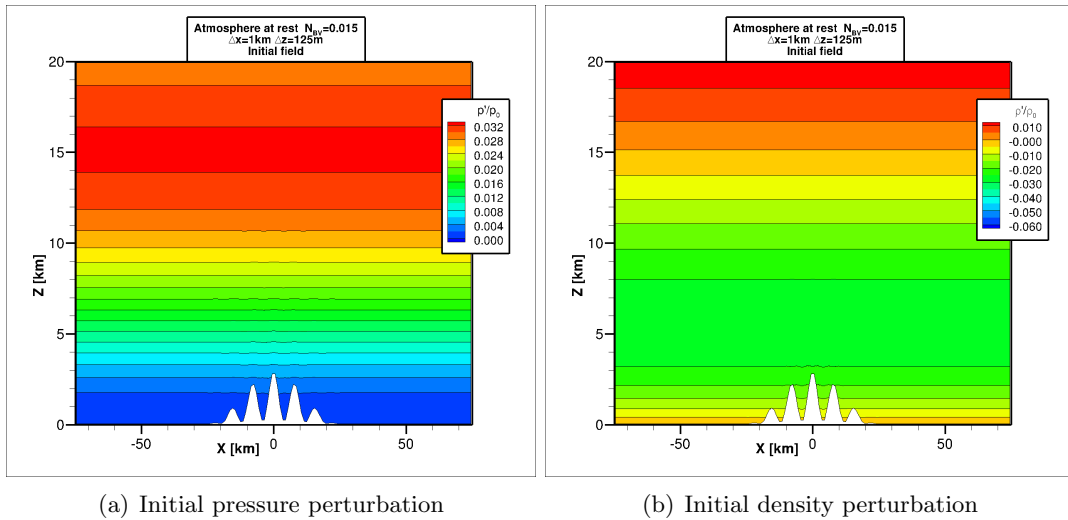
(a) Initial pressure perturbation

(b) Initial density perturbation

Figure 63: Initial perturbation field for atmosphere with N_{BV}=0.015 1/s
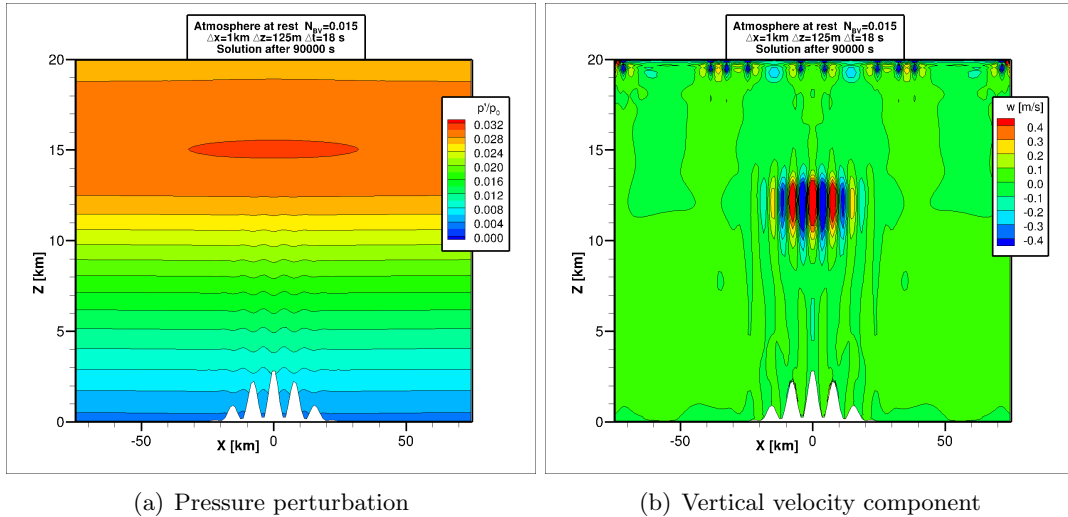
(a) Pressure perturbation   (b) Vertical velocity component

Figure 64: Velocity components after 90000 s

The magnitude of the spurious velocity field is affected by the artificial viscosity ν: near the ground it damps the oscillations, at the higher levels the mesh stretching in vertical direction increases the artificial fluxes. This effect calls for a more appropriate formulation of the artificial dissipation and for a smoother mesh clustering in vertical direction.

An exact solution of the discrete equations for the atmosphere at rest can be obtained in 2D cases on generic meshes: the pressure field can be computed from the equation for the horizontal component (equilibrium of the horizontal component of the pressure forces acting on the four sides of each cell): the pressure depends upon the metric terms. After the pressure has been computed, the density field can be readily derived from the equilibrium in vertical direction. An example of such a 2D solution for a skewed mesh shown in Fig. 65.

(a) Pressure perturbation   (b) Vertical velocity component
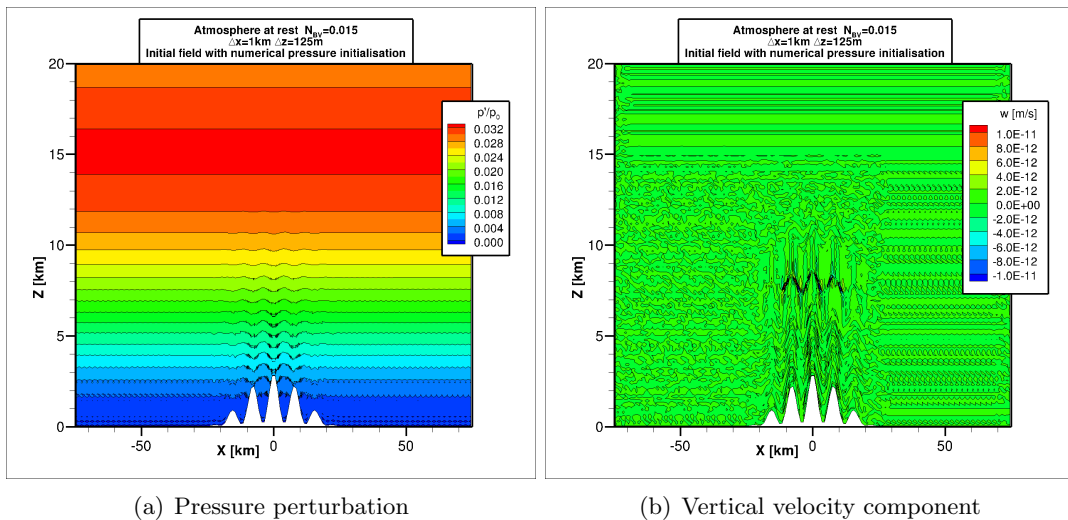
Figure 65: Exact solution of the discrete equations for 2D atmosphere at rest: pressure field computed from the equilibrium in horizontal direction

By comparing the numerical solution of pressure and density fields with the mathematical solution (horizontal stratification) the effect of a deformed mesh can be seen: it is clear that a mesh deformation induces disturbances in the field in such a way that pressure is increased where the mesh density decreases (i.e. in correspondence of the valleys). The resulting

velocity field is balanced.

8.5   Pressure gradient correction

A correction of the pressure gradient terms has been tested, in order to reduce the spurious velocity for the atmosphere at rest. This seems to improve the convergence rate of dual time iterations as well. The basic idea is to add a first order correction to the pressure averaged at the cell faces, by considering the vertical pressure gradient ρg, when the face center has different vertical coordinate from the cell center. Two different approaches were tested and compared. In the first case the density is considered to be constant inside a mesh cell. The averaged pressure at the face between cells m and k is computed as follows:

$$p'_{mk} = \frac{p'_m + (\frac{\partial p'}{\partial z})_m \delta z_m + p'_k + (\frac{\partial p'}{\partial z})_k \delta z_k}{2} \tag{61}$$

where δz_k is the difference between the z coordinate of the cell face center and the k cell center.

$$(\frac{\partial p'}{\partial z})_k = \rho'_k g \tag{62}$$

The second approach considers a vertical gradient of the density perturbation inside the cell, related to the pressure gradient by the isentropic relation:

$$(\frac{\partial p'}{\partial \rho'}) = \gamma p / \rho = c^2 \tag{63}$$

It means that entropy is assumed to be constant inside a cell, rather than density. Both the averaged pressure and density are modified by adding the following corrections like in eq.(61):

$$(\frac{\partial p'}{\partial z})_k = \frac{\rho'_k g}{1 + \frac{\delta z_k}{c^2}} \tag{64}$$

$$(\frac{\partial \rho'}{\partial z})_k = \frac{\rho'_k g}{c^2 + \delta z_k} \tag{65}$$

The perturbation fields after 90000 seconds are compared in Fig. 66 and show similar behavior, with smaller velocities near the ground. Finally, the effect of reducing the artificial viscosity is shown in Fig. 66(d). The flow computations of the atmosphere at rest were carried out with time steps ranging from 18 to 750 seconds, without significant differences in the results.
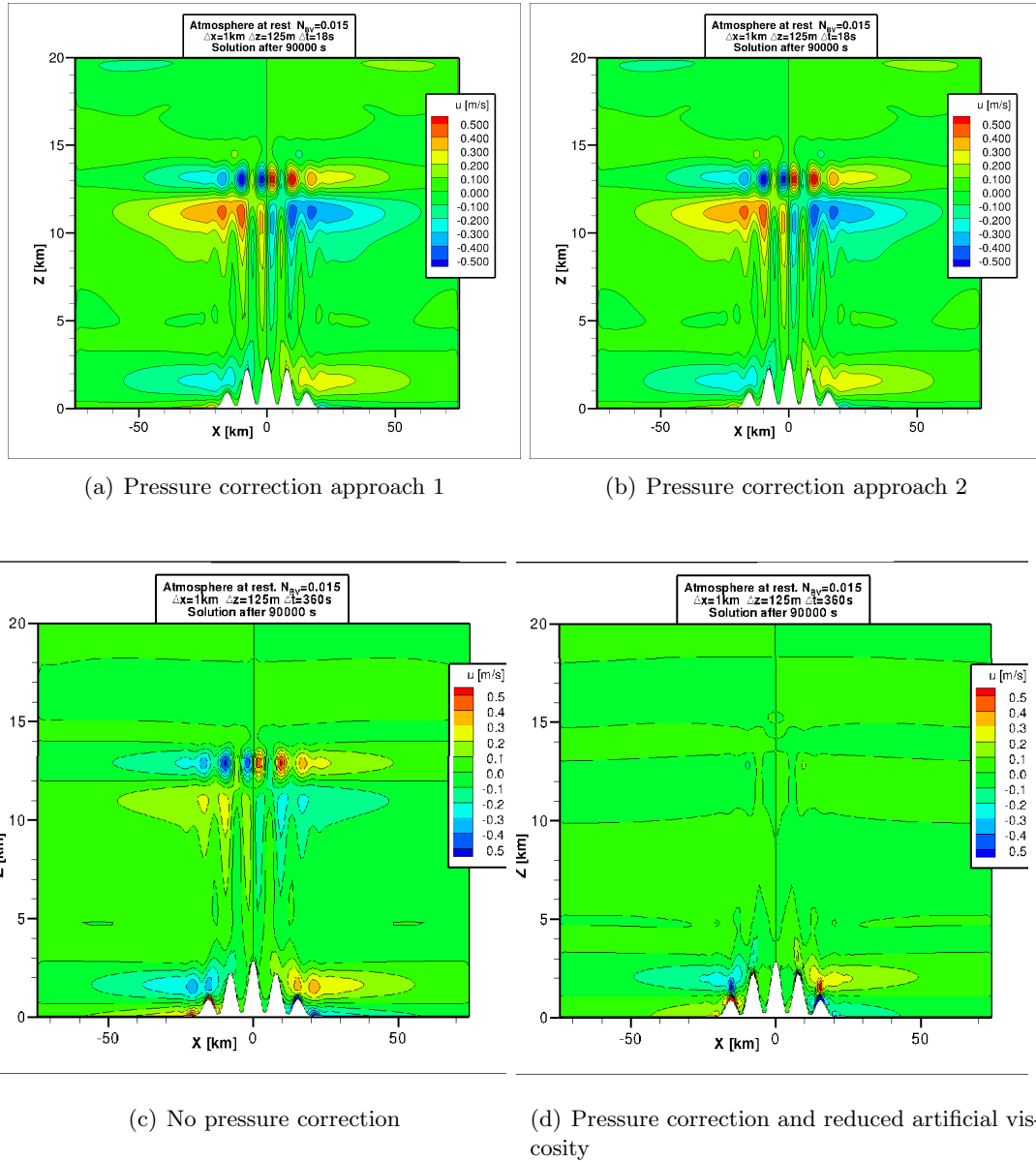
(a) Pressure correction approach 1

(b) Pressure correction approach 2

(c) No pressure correction

(d) Pressure correction and reduced artificial viscosity

Figure 66: Comparison of horizontal velocity components after 90000 s with different pressure correction approaches

8.6　Gravity wave

The test case is described in Skamarock and Klemp (1994), it shows the capability of the present scheme to simulate the time evolution of gravity waves produced by potential temperature perturbations. The flow field is initialized with constant Brunt Väisälä frequency N_{BV}=0.01 1/s in a channel of length 300 km and height 10 km, with rigid free-slip upper and lower boundaries. A small perturbation of potential temperature is located at x=-50 km (Fig. 67(a)). The wave is advected by a uniform stream of 20 m/s. The perturbation of total temperature is implemented as a perturbation of density. The mesh is made of 1200x40 cells, $\Delta x=\Delta z$=250m. Initial disturbance of potential temperature and solution computed after 3000 s are shown in Fig. 67. Time steps from 0.25 s to 50 s were tested, although details of the solution deteriorate when the time step is larger than 3 s.
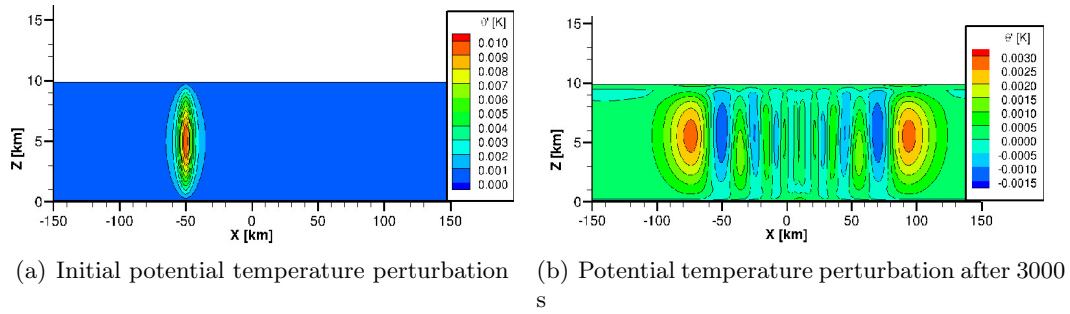
(a) Initial potential temperature perturbation   (b) Potential temperature perturbation after 3000 s

Figure 67: Gravity wave. Mesh with Δx=Δz=250 m, time step 1 s

8.7   Density current

The test case is described in Straka et al. (1993). The equation set is completed by viscous fluxes (momentum and internal energy diffusion), with constant diffusion coefficient. Different mesh sizes (from $\Delta x = \Delta z$= 200m to 12.5m) and time steps between 0.25 and 10 seconds were tested. The complete flow field was simulated, without symmetric boundary condition in x=0. The solution is affected by the time step when Δt is larger than 1 second: it seems that larger time steps introduce a sort of viscosity, so that local maxima of the flow variables are smoothed and velocity is smaller. Mesh size below 50 m is sufficient to obtain grid-converged solutions. In Fig. 68 the solution obtained with the finest mesh is shown, together with a comparison of the potential temperature obtained with different mesh density and time step.
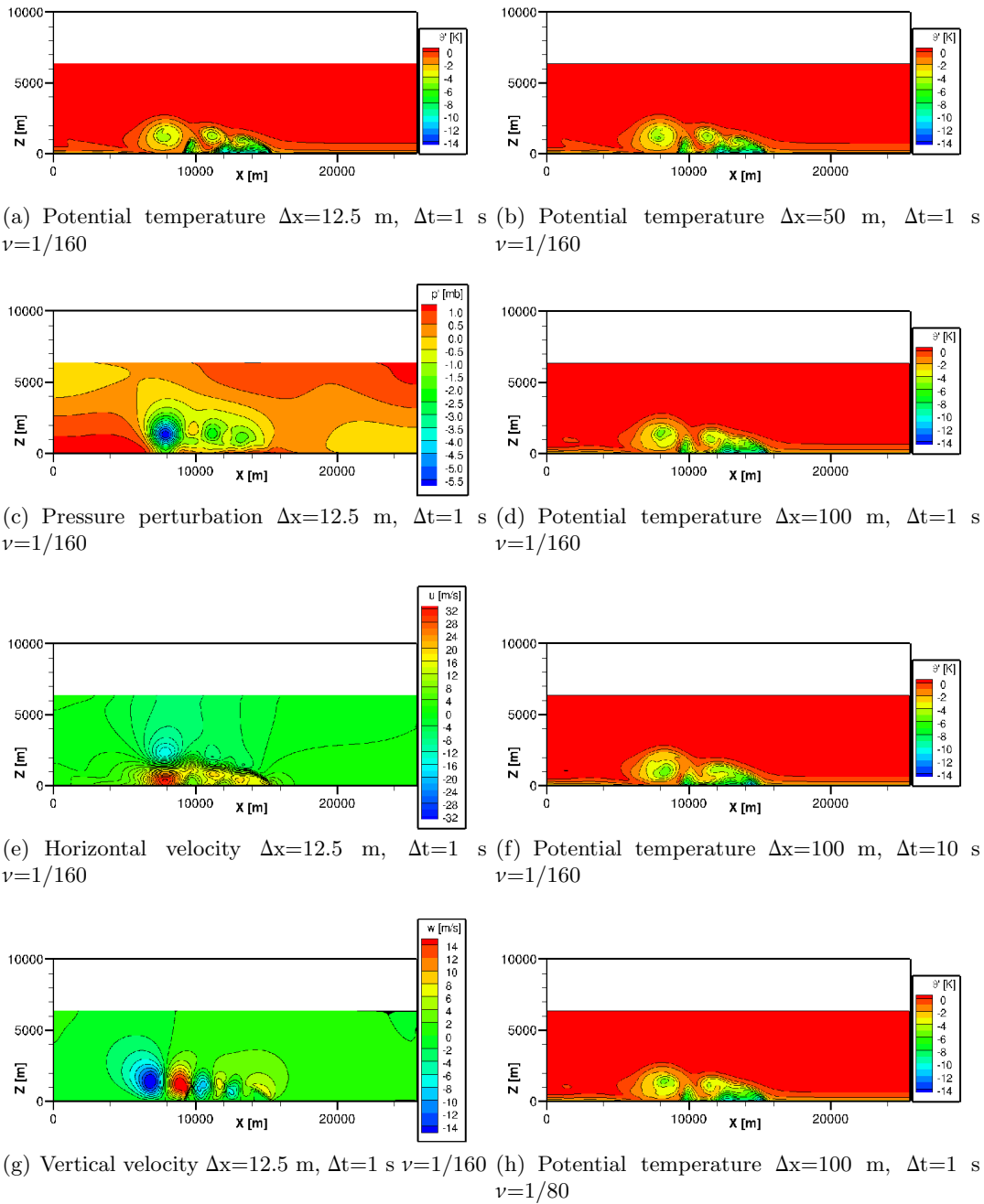
(a) Potential temperature Δx=12.5 m, Δt=1 s ν=1/160

(b) Potential temperature Δx=50 m, Δt=1 s ν=1/160

(c) Pressure perturbation Δx=12.5 m, Δt=1 s ν=1/160

(d) Potential temperature Δx=100 m, Δt=1 s ν=1/160

(e) Horizontal velocity Δx=12.5 m, Δt=1 s ν=1/160

(f) Potential temperature Δx=100 m, Δt=10 s ν=1/160

(g) Vertical velocity Δx=12.5 m, Δt=1 s ν=1/160

(h) Potential temperature Δx=100 m, Δt=1 s ν=1/80

Figure 68: Density current. Results after 900 s. Left: mesh with Δx=12.5 m. Right: effect of mesh density, time step, artificial dissipation ν

8.8 Advection

The test case is described in Schär et al. (2002). A scalar quantity contained in a circular bubble is advected accross a highly skewed mesh. The inflow velocity is 0 below the altitude of 4 km and rises smoothly to 10 m/s between 4 km and 5 km. Two different meshes were tested: the first one contains 300x50 cells with Δx=1 km and Δz=500 m, the second one has twice the number of cells in both directions with Δx=0.5 km and Δz=250 m (Fig. 69). A time step of 50 s was adopted in both computations. An attempt was made to implement and test the fourth order scheme described in Kok (2009), without significant improvements.
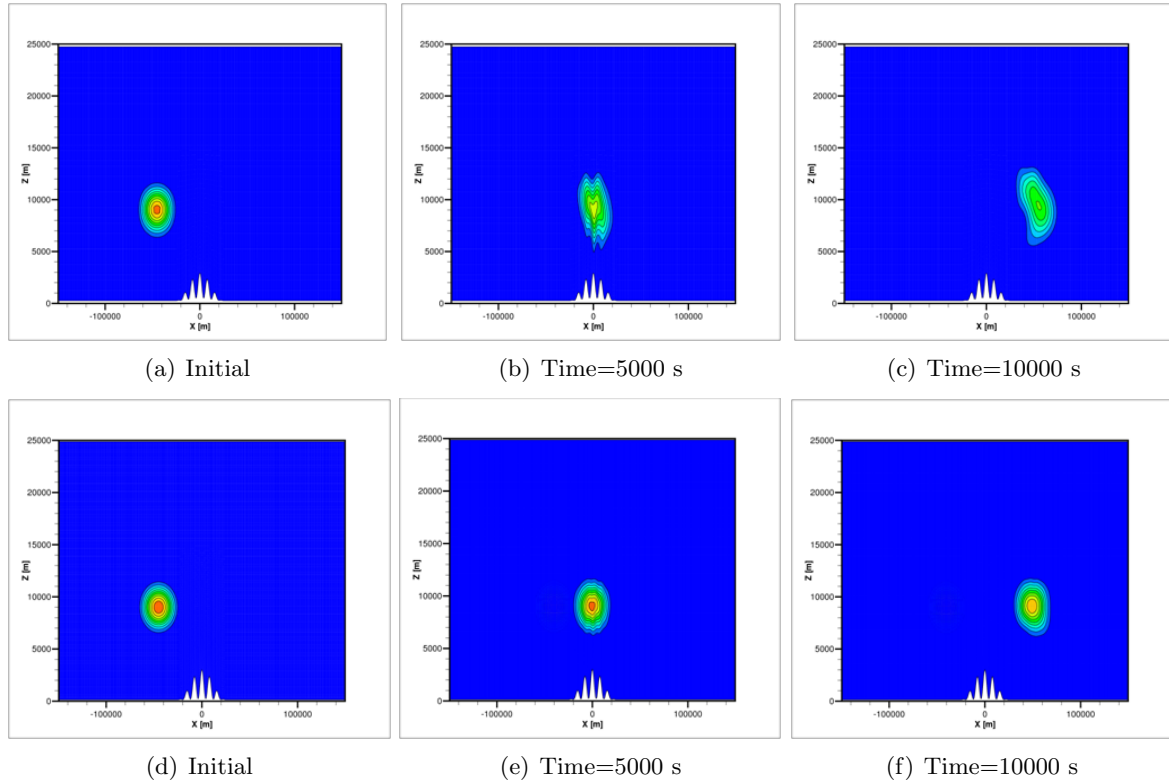
(a) Initial　　　　　　　(b) Time=5000 s　　　　　　(c) Time=10000 s

(d) Initial　　　　　　　(e) Time=5000 s　　　　　　(f) Time=10000 s

Figure 69: Advection of a conserved quantity in a deformed mesh. Above: coarse mesh 1. Below: mesh 2

8.9　Hydrostatic mountain flow

A classical hydrostatic test case is the flow simulation of a reference atmosphere with Brunt Väisälä frequency N_{BV}=0.01 1/s over a Gaussian shaped hill 10 m high, with free stream velocity of 10 m/s. The gravity waves produced above the mountain are stationary and momentum is transported in vertical direction. In order to avoid spurious reflection of the waves against the upper boundary, two techniques can be adopted: a damping layer in the upper atmosphere, where vertical velocities are smoothly damped, or a radiative upper boundary condition, that allows the wave energy to cross the boundary without reflection. In the first case (Fig. 70 a) about one third of the flow field is affected by an artificial damping term, that modifies the global momentum budget. In the second case (Fig. 70 b) the boundary condition has to be tuned to the local flow conditions, in order to be effective.
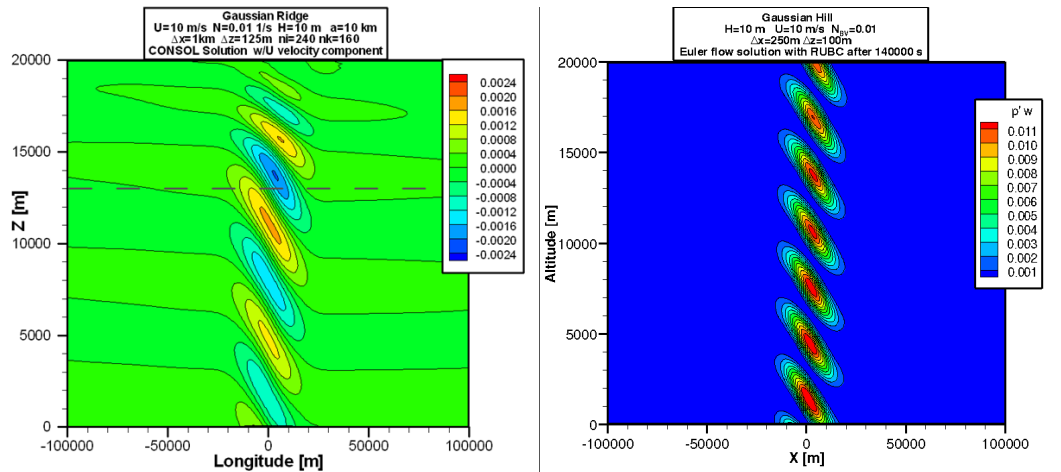
(a) Rayleigh damping: velocity field. The dashed line shows the lower side of the damping layer

(b) Radiative upper boundary condition: energy flux

Figure 70: Hydrostatic flow computed with different upper boundary conditions

8.10   Conclusions

The CONSOL flow solver, based upon second order central finite volume schemes and implicit time integration with dual time stepping, is capable to simulate the test cases considered in the present work. A wide range of time steps can be adopted, as it is not limited by numerical stability, that could be an advantage when time accuracy is not an issue. It is not possible at this moment to draw a conclusion about the numerical efficiency with respect to other schemes, since the solver is not optimized yet. More complex 3D test cases should be simulated.

8.11   Implementation of a time integration procedure based upon dual time stepping in COSMO

The time integration procedure based upon dual time stepping was implemented in a test version of COSMO, by replacing the Runge-Kutta scheme currently adopted. This preliminary study was meant to assess the possibility to use the scheme in the dynamical core of COSMO. It seems that the dual time stepping was never used in the field of numerical weather prediction, despite its popularity in aerodynamics. The idea was to keep the equations set with the spatial discretization schemes adopted in COSMO, and to replace only the time integration scheme. Main difference is that the time splitting procedure operates in physical time, by advancing the flow solution with smaller time steps for the fast processes and larger steps for slow processes. The dual time stepping computes all processes with the same time step, and iterates in order to improve the evaluation of the flow variables and the time derivatives using the 'dual' time as relaxation parameter. The dual time relaxation is a pseudo-steady problem, which does not require time accuracy and can be solved with any convergence acceleration technique, like local time stepping, implicit residual averaging and preconditioning. As the scheme is implicit, in theory there is no limitation to the physical time step due to stability.

Defining the prognostic variables in the COSMO solver as $\underline{\mathbf{U}} = (u,v,w,p',T')$ and the model equations as

$$\frac{\partial \underline{\mathbf{U}}}{\partial t} = -R(\underline{\mathbf{U}}) \tag{66}$$

where $R(\underline{\mathbf{U}})$ denotes the right hand side of the model equation for $\underline{\mathbf{U}}$, the Runge Kutta integration takes the form of three steps to advance a solution $\underline{\mathbf{U}}(t)$ to $\underline{\mathbf{U}}(t + \Delta t)$:

$$
\begin{aligned}
\underline{\mathbf{U}}^* &= \underline{\mathbf{U}}^t - \frac{\Delta t}{3} R(\underline{\mathbf{U}}^t) \\
\underline{\mathbf{U}}^{**} &= \underline{\mathbf{U}}^t - \frac{\Delta t}{2} R(\underline{\mathbf{U}}^*), \\
\underline{\mathbf{U}}^{t+\Delta t} &= \underline{\mathbf{U}}^t - \Delta t R(\underline{\mathbf{U}}^{**})
\end{aligned}
\tag{67}
$$

where Δt is the time step for the slow-frequency modes (the model time step), and superscripts denote time levels. The time-splitting technique integrates fast modes with smaller time steps; terms associated with horizontally propagating modes are integrated explicitly, while terms associated with vertically propagating modes are integrated implicitly. The implicit integration component alleviates the severe Courant number restriction, arising from vertically propagating acoustic modes when using grids with large aspect ratios $\frac{\Delta x}{\Delta z}$, at the cost of a simple tridiagonal matrix inversion. The Figure 71a shows the three stages of the Runge-Kutta time integration procedure, where the blue arrows represent the small time steps used to advance the fast tendencies of the governing equations, while the slow tendencies are kept constant in each stage, represented by the red arrows.

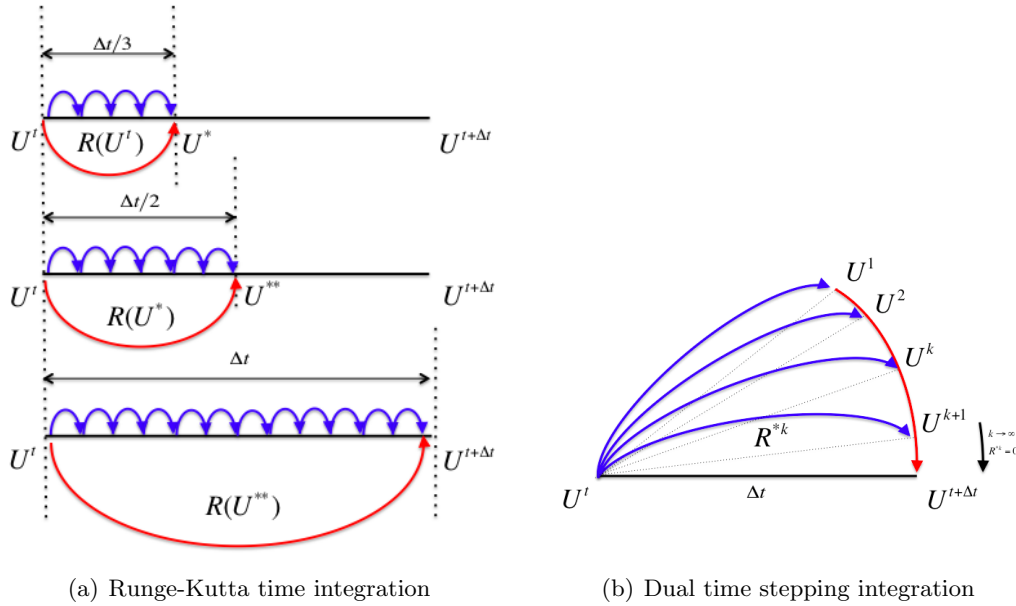(a) Runge-Kutta time integration   (b) Dual time stepping integration

Figure 71: Time integrations in COSMO: 3 stages Runge-Kutta and Dual time stepping

In the dual time stepping procedure (see equations 47 and 48) the residual at the dual iteration k is computed as follows:

$$\underline{\mathbf{R}}^{*k} = \underline{\mathbf{R}}(\underline{\mathbf{U}}^k) + \frac{3\underline{\mathbf{U}}^k - 4\underline{\mathbf{U}}^t + \underline{\mathbf{U}}^{t-\Delta t}}{2\Delta t} \tag{68}$$

we evaluate $\underline{\mathbf{R}}(\underline{\mathbf{U}}^k)$ using the spatial schemes already implemented in the dynamical core of COSMO for computing the time derivatives. The dual time derivative

$$\frac{\partial \underline{\mathbf{U}}^k}{\partial \tau} = -\underline{\mathbf{R}}^{*k} \tag{69}$$

is integrated to the steady state (see Fig. 71b). A flow chart of the implementation is shown in Fig. 72.
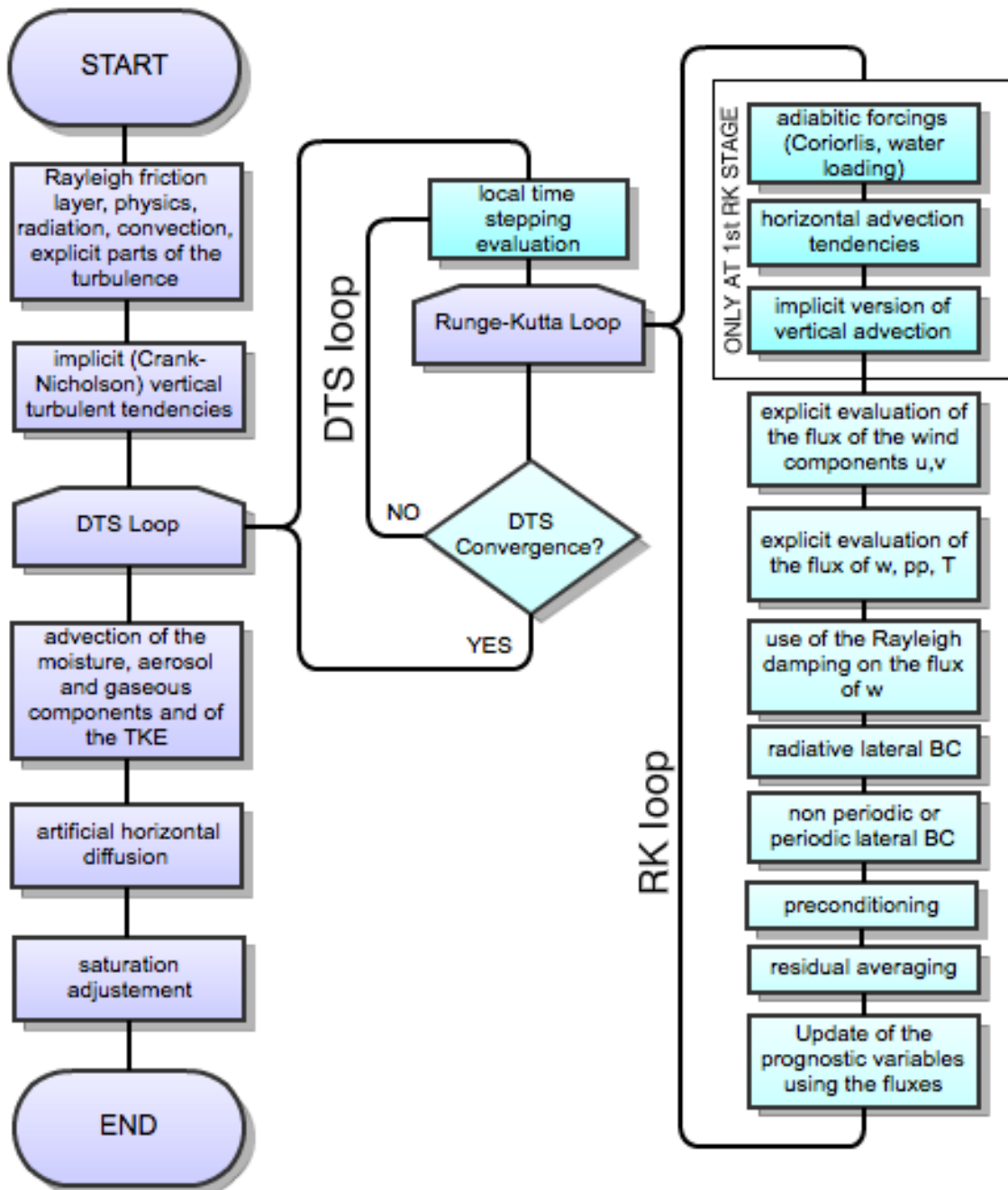

Figure 72: Flow chart of the Dual time stepping implementation in COSMO

Idealized test cases were computed, like mountain flow and inertia-gravity waves, which have

shown that the scheme is capable to give similar results to the original COSMO model, as reported in Petrone (2012). Larger time steps can be adopted. Applications to real test cases would require further work to be completed.

References

Baldauf, M., 2008: A linear solution for flow over mountains and its comparison with the COSMO model. *COSMO-Newsletter*,**9**, 19–24.

Baldauf, M., 2010: Linear stability analysis of Runge-Kutta based partial time-splitting schemes for the Euler equations. *Mon. Wea. Rev.*,**138**, 4475–4496.

Baldauf, M., and S. Brdar, 2013: An Analytic Solution for Linear Gravity Waves in a Channel as a Test for Numerical Models using the Non-Hydrostatic, Compressible Euler Equations. *Q. J. R. Meteorol. Soc.*, DOI:10.1002/qj.2105.

Botta, N., R. Klein, S. Langenberg, S. Lützenkirchen, 2004: Well balanced finite volume methods for nearly hydrostatic flows. *J. Comput. Phys.*,**196**, 539–565.

Choi, Y.-H. and C. L. Merkle, 1993: The application of preconditioning in viscous flows. *J. Comput. Phys.*, **105**, 207.

Giraldo, F. X., and M. Restelli, 2008: A study of spectral element and discontinuous Galerkin methods for the Navier-Stokes equations in nonhydrostatic mesoscale atmospheric modeling: equation sets and test cases. *J. Comput. Phys.*, **227**, 3849–3877.

Jameson, A., 1992: Time dependent calculations using multigrid with applications to unsteady flows past airfoils and wings. *AIAA Paper*, **91**, 1596.

Kok, J. C., 2009: A high-order low-dispersion symmetry-preserving finite-volume method for compressible flow on curvilinear grids. *J. Comput. Phys.*, **228**, 6811–6832.

Petrone, G., 2012: Implementation of a numerical scheme based on the dual time stepping in COSMO LM: idealized test cases. Research Papers Issues RP0146, CMCC.

Robert, A., 1993: Bubble convection experiments with a semi-implicit formulation of the Euler equations. *J. Atmos. Sci.*, **50**, No. 13, 1865–1873.

Schär, C., D. Leuenberger, O. Fuhrer, D. Lüthi, and C. Girard, 2002: A new terrain-following vertical coordinate formulation for atmospheric prediction models. *Mon. Wea. Rev.*, **130(10)**, 2459–2480.

Skamarock, W. C. and J. B. Klemp, 1992: The stability of time-split numerical methods for the hydrostatic and the nonhydrostatic elastic equations. *Mon. Wea. Rev.*, **120**, 2109–2127.

Skamarock, W. C. and J. B. Klemp, 1994: Efficiency and accuracy of the Klemp-Wilhelmson time-splitting scheme. *Mon. Wea. Rev.*, **122**, 2623–2630.

Straka, J. M., R. B. Wilhelmson, L. J. Wicker, J. R. Anderson, and K. K. Droegemeier, 1993: Numerical solutions of a non-linear density current: A benchmark solution and comparisons. *Int. J. Num. Meth. Fluids*, **17**, 1–22.

Turkel, E., V. N. Vatsa, and R. Radespiel, 1996: Preconditioning methods for low speed flows. *AIAA-96-2460-CP*, 650–660.

Turkel, E., 1999: Preconditioning techniques in computational fluid dynamics. *Annu. Rev. Fluid Mech.*, **31**, 385–416.

Weiss, J. M. and W. A. Smith, 1995: Preconditioning applied to variable and constant density flows. *AIAA Journal*, **33**, No. 11, 2050–2057.

Wicker, J. L. and W. C. Skamarock, 1998: A time-splitting scheme for elastic equations incorporating second-order Runge-Kutta time differencing. *Mon. Wea. Rev.*, **126**, 1992–1999.

Wicker, J. L. and W. C. Skamarock, 2002: Time-splitting method for elastic models using forward time schemes. *Mon. Wea. Rev.*, **130**, 2088–2097.

Wunderlich, S., 2004: A 2D well balanced finite volume non-hydrostatic atmospheric model. Hydrostatic balance and simulation of mountain waves. *Ph.D. thesis ETH Zürich.*

Zängl, G., L. Gantner, G. Hartjenstein, H. Noppel, 2004: Numerical errors above steep topography: a model intercomparison. *Meteorol. Z.*, **13**, No. 2, 69–76.

9   Acknowledgement

List of COSMO Newsletters and Technical Reports

(available for download from the COSMO Website: www.cosmo-model.org)

COSMO Newsletters

No. 1: February 2001.

No. 2: February 2002.

No. 3: February 2003.

No. 4: February 2004.

No. 5: April 2005.

No. 6: July 2006.

No. 7: April 2008; Proceedings from the 8th COSMO General Meeting in Bucharest, 2006.

No. 8: September 2008; Proceedings from the 9th COSMO General Meeting in Athens, 2007.

No. 9: December 2008.

No. 10: March 2010.

No. 11: April 2011.

No. 12: April 2012.

No. 13: April 2013.

COSMO Technical Reports

No. 1: Dmitrii Mironov and Matthias Raschendorfer (2001):
Evaluation of Empirical Parameters of the New LM Surface-Layer Parameterization Scheme. Results from Numerical Experiments Including the Soil Moisture Analysis.

No. 2: Reinhold Schrodin and Erdmann Heise (2001):
The Multi-Layer Version of the DWD Soil Model TERRA_LM.

No. 3: Günther Doms (2001):
A Scheme for Monotonic Numerical Diffusion in the LM.

No. 4: Hans-Joachim Herzog, Ursula Schubert, Gerd Vogel, Adelheid Fiedler and Roswitha Kirchner (2002):
LLM ¯ the High-Resolving Nonhydrostatic Simulation Model in the DWD-Project LIT-FASS.
Part I: Modelling Technique and Simulation Method.

No. 5: Jean-Marie Bettems (2002):
EUCOS Impact Study Using the Limited-Area Non-Hydrostatic NWP Model in Operational Use at MeteoSwiss.

No. 6: Heinz-Werner Bitzer and Jürgen Steppeler (2004):
Documentation of the Z-Coordinate Dynamical Core of LM.

No. 7: Hans-Joachim Herzog, Almut Gassmann (2005):
Lorenz- and Charney-Phillips vertical grid experimentation using a compressible non-hydrostatic toy-model relevant to the fast-mode part of the 'Lokal-Modell'.

No. 8: Chiara Marsigli, Andrea Montani, Tiziana Paccagnella, Davide Sacchetti, André Walser, Marco Arpagaus, Thomas Schumann (2005):
Evaluation of the Performance of the COSMO-LEPS System.

No. 9: Erdmann Heise, Bodo Ritter, Reinhold Schrodin (2006):
Operational Implementation of the Multilayer Soil Model.

No. 10: M.D. Tsyrulnikov (2007):
Is the particle filtering approach appropriate for meso-scale data assimilation ?

No. 11: Dmitrii V. Mironov (2008):
Parameterization of Lakes in Numerical Weather Prediction. Description of a Lake Model.

No. 12: Adriano Raspanti (2009):
COSMO Priority Project "VERification System Unified Survey" (VERSUS): Final Report.

No. 13: Chiara Marsigli (2009):
COSMO Priority Project "Short Range Ensemble Prediction System" (SREPS): Final Report.

No. 14: Michael Baldauf (2009):
COSMO Priority Project "Further Developments of the Runge-Kutta Time Integration Scheme" (RK): Final Report.

No. 15: Silke Dierer (2009):
COSMO Priority Project "Tackle deficiencies in quantitative precipitation forecast" (QPF): Final Report.

No. 16: Pierre Eckert (2009):
COSMO Priority Project "INTERP": Final Report.

No. 17: D. Leuenberger, M. Stoll and A. Roches (2010):
Description of some convective indices implemented in the COSMO model.

No. 18: Daniel Leuenberger (2010):
Statistical analysis of high-resolution COSMO Ensemble forecasts in view of Data Assimilation.

No. 19: A. Montani, D. Cesari, C. Marsigli, T. Paccagnella (2010):
Seven years of activity in the field of mesoscale ensemble forecasting by the COSMO–LEPS system: main achievements and open challenges.

No. 20: A. Roches, O. Fuhrer (2012):
Tracer module in the COSMO model.

No. 21: Michael Baldauf (2013):
A new fast-waves solver for the Runge-Kutta dynamical core.

No. 22: C. Marsigli, T. Diomede, A. Montani, T. Paccagnella, P. Louka, F. Gofa, A. Corigliano (2013):
The CONSENS Priority Project.

COSMO Technical Reports

Issues of the COSMO Technical Reports series are published by the *COnsortium for Small-scale MOdelling* at non-regular intervals. COSMO is a European group for numerical weather prediction with participating meteorological services from Germany (DWD, AWGeophys), Greece (HNMS), Italy (USAM, ARPA-SIMC, ARPA Piemonte), Switzerland (MeteoSwiss), Poland (IMGW), Romania (NMA) and Russia (RHM). The general goal is to develop, improve and maintain a non-hydrostatic limited area modelling system to be used for both operational and research applications by the members of COSMO. This system is initially based on the COSMO-Model (previously known as LM) of DWD with its corresponding data assimilation system.

The Technical Reports are intended

- for scientific contributions and a documentation of research activities,
- to present and discuss results obtained from the model system,
- to present and discuss verification results and interpretation methods,
- for a documentation of technical changes to the model system,
- to give an overview of new components of the model system.

The purpose of these reports is to communicate results, changes and progress related to the LM model system relatively fast within the COSMO consortium, and also to inform other NWP groups on our current research activities. In this way the discussion on a specific topic can be stimulated at an early stage. In order to publish a report very soon after the completion of the manuscript, we have decided to omit a thorough reviewing procedure and only a rough check is done by the editors and a third reviewer. We apologize for typographical and other errors or inconsistencies which may still be present.

At present, the Technical Reports are available for download from the COSMO web site (www.cosmo-model.org). If required, the member meteorological centres can produce hardcopies by their own for distribution within their service. All members of the consortium will be informed about new issues by email.

For any comments and questions, please contact the editor:

Massimo Milelli
Massimo.Milelli@arpa.piemonte.it